SAND78-8183
Unlimited Release

Performance Analysis for the MDAC Rocketdyne Pilot and Commercial Plant Solar Receivers

Prepared by Sandia Laboratories, Albuquerque, New Mexico 87115 and Livermore, California 94550 for the United States Department of Energy under Contract AT (29-1)-789.

Printed September 1978

Sandia Laboratories
energy report

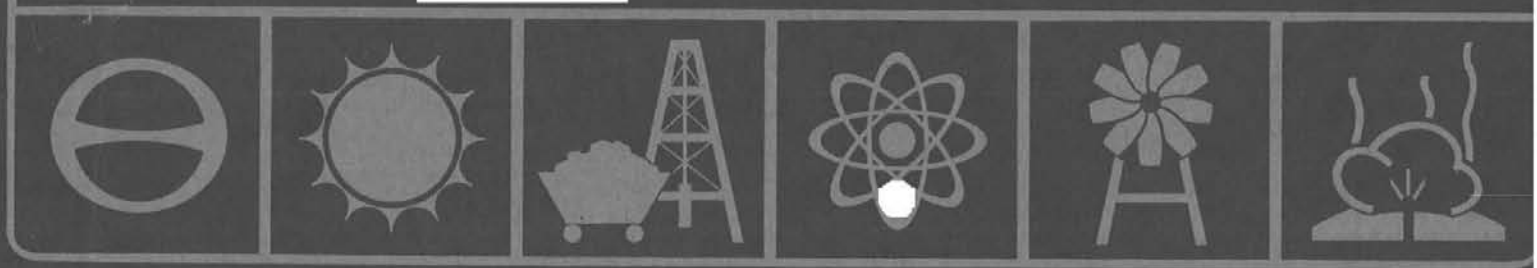

Printed in the United States of America
Available from
National Technical Information Service
U. S. Department of Commerce
5285 Port Royal Road
Springfield, VA 22161
Price: Printed Copy $6.50 ; Microfiche $3.00

FBRD 00073-2

DATE June 1978

TITLE: PERFORMANCE ANALYSIS FOR THE MDAC ROCKETDYNE PILOT AND COMMERCIAL PLANT SOLAR RECEIVERS

AUTHORS: S. Wolf, K. Chen, T. M. Yang and J. L. Simpson

APPROVALS: D H Imhoff

D. H. Imhoff, Manager
Development Engineering

J B Baus for C N Craig

C. N. Craig, Manager
Technology & Special Projects

Prepared for Sandia Laboratories

Under Contract No. 18-2969

GENERAL ELECTRIC

FAST BREEDER REACTOR DEPARTMENT • GENERAL ELECTRIC COMPANY
SUNNYVALE, CALIFORNIA 94086

DISCLAIMER OF RESPONSIBILITY

TABLE OF CONTENTS

TABLE OF CONTENTS (Continued)

LIST OF ILLUSTRATIONS

LIST OF ILLUSTRATIONS

LIST OF ILLUSTRATIONS

LIST OF ILLUSTRATIONS

LIST OF TABLES

ABSTRACT

This report presents results of analyses and reviews to evaluate selective features of receiver boiler panel designs proposed by McDonnell Douglas Astronautics Company for a 10-MWe pilot and a 100-MWe commercial solar-electric power plant. Overall thermal performance conditions are predicted for maximum and minimum heat flux conditions with a steady-state code, including parameters to take into account some of the two-dimensional effects resulting from nonuniform circumferential solar heating. Thermal and stress oscillations occurring in the tube walls in the transition boiling region following the critical heat flux point are predicted for the maximum heat flux condition for the pilot plant and for the maximum and 80% of maximum heat flux conditions for the commercial plant. A two-dimensional rivulet model is used for the thermal analysis and a generalized plane strain elastic model is used for the stress analysis leading to fatigue life predictions. Dynamic stability is investigated with a frequency domain model, modified by adding a superheat regime. Nyquist plots are presented for the maximum and minimum heat flux conditions without and with tube inlet orificing. Water chemistry and potential deposition/corrosion effects are evaluated based on a review of modern boiler water practices and recommendations for the solar plant are presented.

1. INTRODUCTION

Preliminary designs proposed by McDonnell Douglas Astronautics Company (MDAC) for a 10-MWe pilot and a 100-MWe commercial solar-elecric power plant include central receivers designed by Rocketdyne Division of Rockwell International.[1] The function of the receiver in a solar power plant is to absorb solar radiation reflected from the collector subsystem and convert that energy into raising the temperature of the water to produce superheated steam for delivery to the turbine subsystem or the thermal storage subsystem. The receiver unit is part of a receiver subsystem as illustrated in Figures 1 and 2 for the pilot and commercial plants, respectively. Each receiver consists of 24 heat-absorbing panels made of small tubes to form a large cylinder which is located on top of a high tower. Several of the panels are used as preheaters and the rest as boilers. A schematic representation of a panel for the plant receiver is shown as Figure 3.

The receiver units are designed to operate as once-through steam generators. Subcooled liquid water enters a set of parallel preheater panels at the bottom, flows upward, and returns downward in another set of preheaters in series. The heated water then flows upward in parallel boiler panels where it is converted to superheated steam. Critical heat flux (CHF) occurs in the boiler tubes. As a result of this situation, several important design problems arise which are associated with the receiver boiler panels and which constitute the subject of this report:

- Overall thermal performance - One of the key factors in this area is the accurate prediction of the heat transfer parameters at the location of CHF, which is used in heat transfer calculations to designate the axial position of a change in water-side heat transfer coefficient from a relatively high value upstream of CHF to a relatively low value in the post-CHF region. In addition, significant circumferential nonuniform heating effects result from solar heating only on the front side of the receiver panels.[2] A theoretical performance evaluation

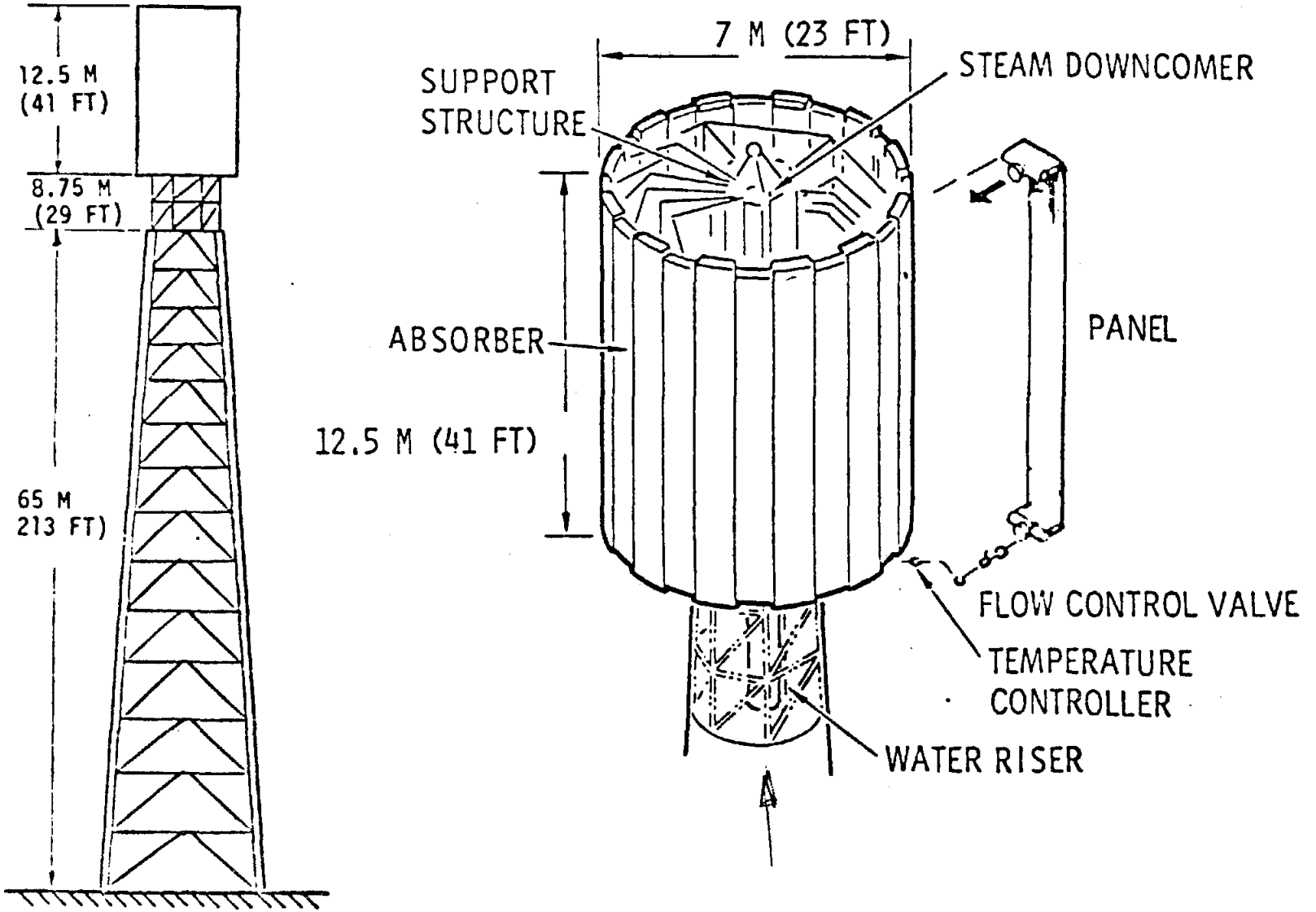

Figure 1. Pilot Plant Receiver

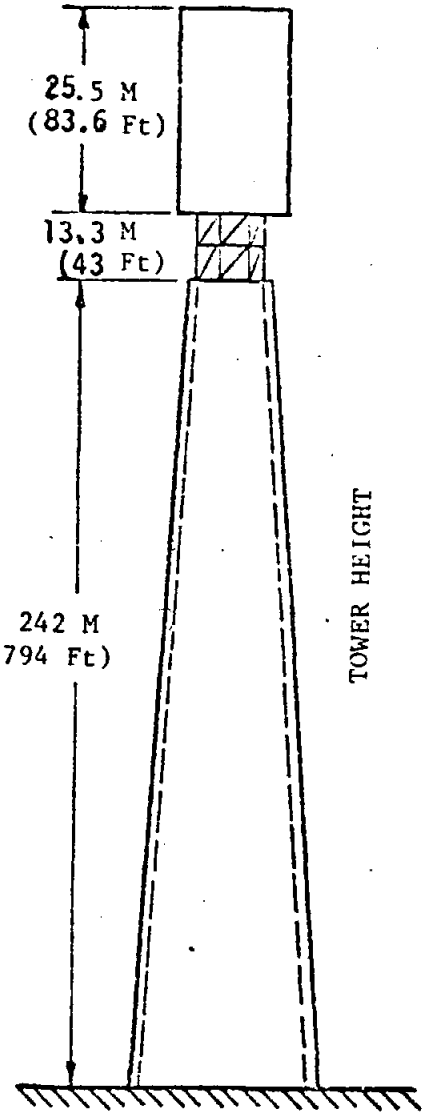

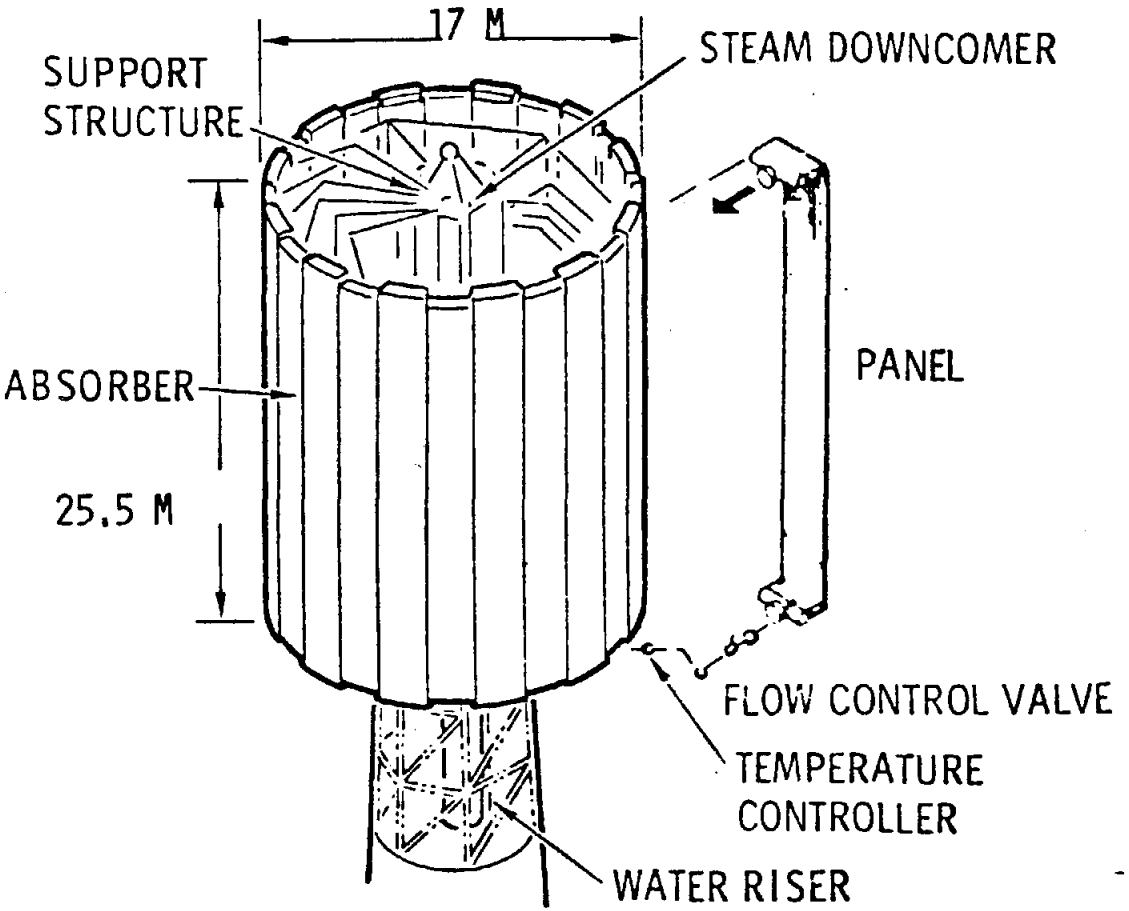

Figure 2. Commercial Plant Receiver

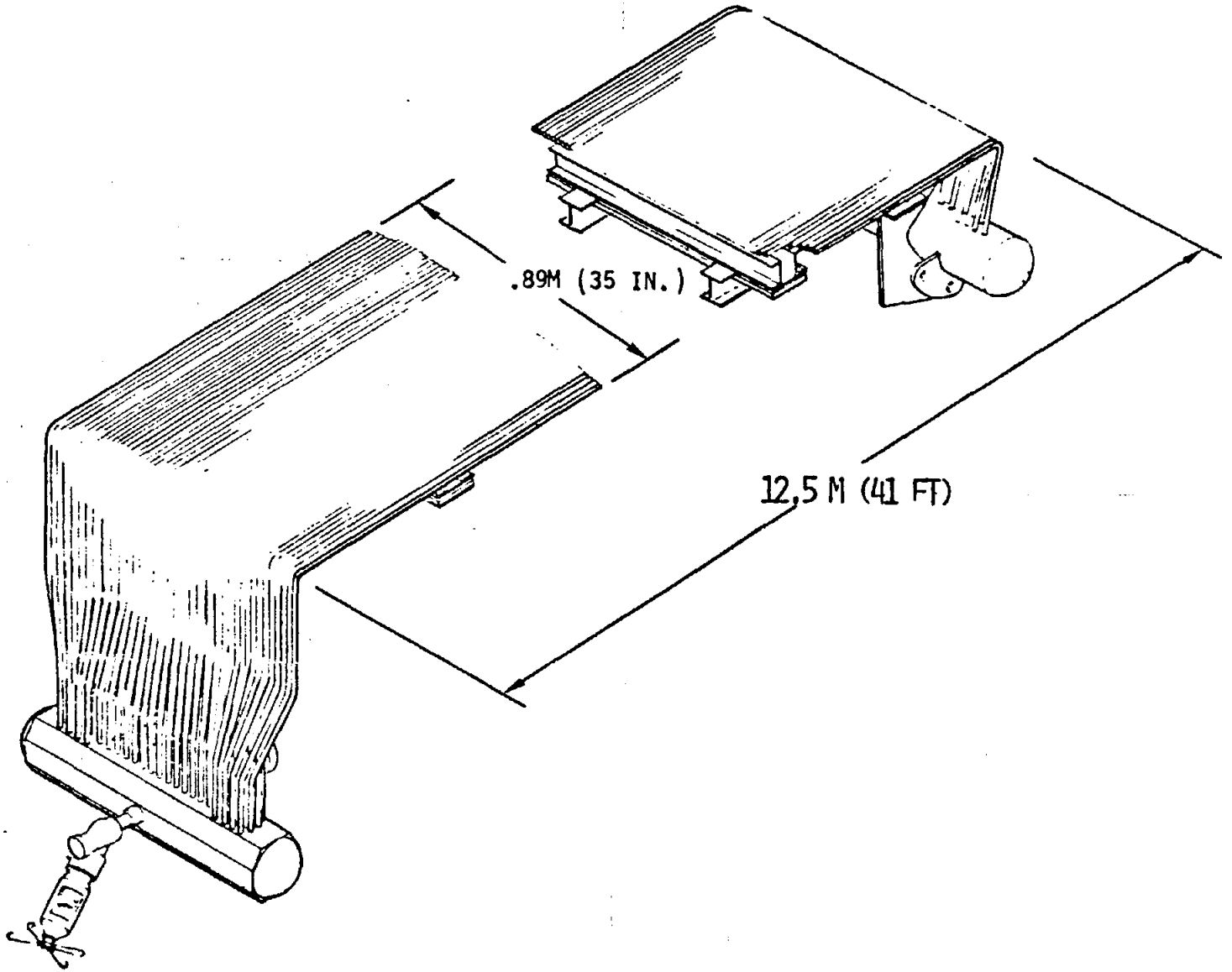

Figure 3. Pilot Plant Receiver Panel

is presented to deal with this design problem. The evaluation utilizes a one-dimensional thermal-hydraulic computer model with empirical heat transfer correlations to evaluate axial effects and a two-dimensional thermal model to evaluate circumferential nonuniform heat transfer effects.

- CHF induced thermal stress oscillations - Thermal fluctuations in the tube wall in the transition boiling region may cause potential fatigue damage. The transition boiling zone immediately downstream of CHF is known to be hydraulically unstable and will produce thermal fluctuations in the water/steam tube walls.[3,4] The thermal stresses in the tube walls are produced by relatively high frequency temperature fluctuations that are inherent in the transition boiling regime, plus lower frequency fluctuations which are system induced. The alternating thermal stresses that are produced in the tube walls, as a consequence, have the potential to shorten the tube life due to fatigue. The frequency of the system induced fluctuations and the length of the transition boiling zone movement are peculiar to each individual steam generator system. Because of the lack of current system definition for the MDAC receiver, the thermal-stress cycling analysis in this report deals only with the inherent thermal fluctuations in the transition boiling region. The analysis is divided into two parts: a thermal analysis followed by a stress analysis. The thermal analysis utilizes values of heat transfer coefficient and heat flux at CHF determined from the overall thermal performance analysis. An oscillating rivulet model is used to model the transition boiling regime to predict temperature oscillations as a function of time. Calculations are performed with a finite element computer model. The stress analysis utilizes the thermal results and the identical finite element model to determine associated alternating stresses and the fatigue life.

- Dynamic instability between individual tubes - Components which transfer heat and experience a phase change of the working fluid are candidates for static and dynamic stability problems. A frequency-domain model initially developed for evaluating potential boiling water reactor (BWR) core instability is modified by adding a superheat regime, and is, subsequently, used to investigate dynamic stability of the solar receiver tubes at maximum and minimum heat flux conditions without and with selective amounts of tube inlet orificing.

- Effects of water chemistry on deposition/corrosion - Deposition/corrosion in steam generator tubes, particularly in the transition boiling region, is a potential source of damage which may result in lengthy outages and expensive modifications or repairs. A review of modern boiler water practices was conducted, and recommendations for feedwater specifications using state-of-the-art methods are given.

- Development testing - Recommendations for additional development testing essential to verify predictions of the receiver performance analysis are presented.

2. THERMAL PERFORMANCE ANALYSIS

2.1 ANALYTICAL MODEL

The receiver boiler panels for both the pilot and commercial solar plants consist of 12.7 mm o.d. by 6.83 mm i.d. (0.5 in. o.d. by 0.269 in. i.d.) Incoloy 800 tubes. The pilot plant receiver has 70 tubes per panel with an active heated length of 12.5 m (41 ft) and the commercial plant receiver has 170 tubes per panel with an active length of 25.5 m (83.7 ft).

Subcooled liquid water enters the receiver boiler tubes at the bottom, absorbing heat as it travels vertically upwards, and is converted to superheated steam. The water inlet flow rate and inlet pressure are adjusted with automatic control functions to maintain specified outlet temperature and pressure conditions. The heat transfer regimes experienced by the water/steam include subcooled heating, subcooled boiling, nucleate boiling up to CHF, film boiling, and superheat. The actual distribution of incident heat flux, temperature, and quality are illustrated in Figure 4. The normal incident heat flux varies directly with cos θ, where θ is measured from the direction normal to the face of the panel as illustrated in the cross section shown in Figure 4.

The model for steady-state thermal performance evaluation is based on stepwise integration of energy and momentum equations applied sequentially to adjacent sections of a typical receiver panel tube. The model equations are summarized in the following paragraphs.

The heat, $q_{a,j}$ absorbed by a tube section of length ΔZ is:

$$q_{a,j} = D_o \Delta Z(q''_{i,j-1} + q''_{i,j})/2 - q_{L,j} \qquad (1)$$

Here q''_i is the incident heat flux based on outer projected tube area and q_L represents the associated heat losses. The subscript j is a counter as the analysis is marched along the tube length, and for simplicity is dropped

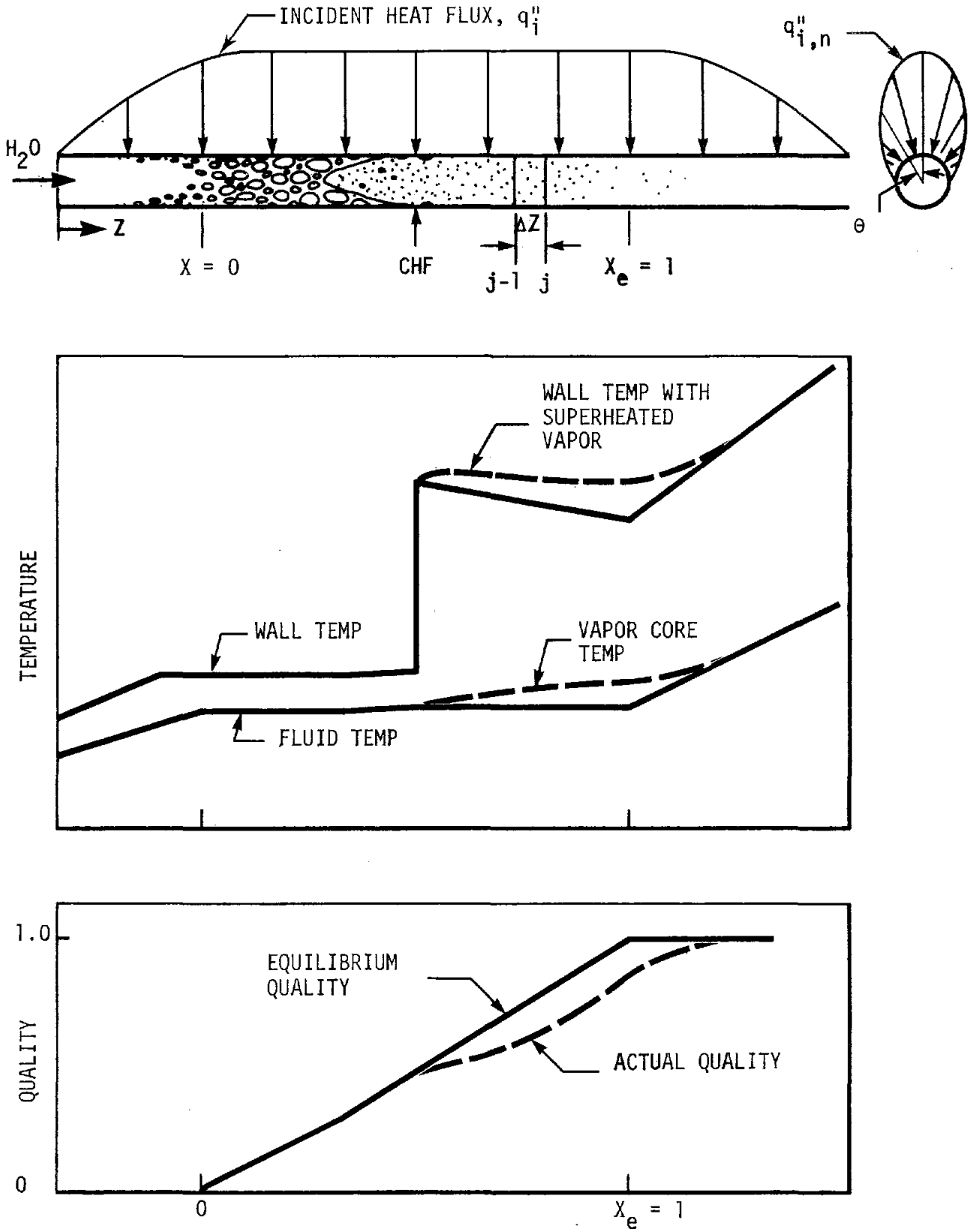

Figure 4. Schematic Representation of Axial Variation in Quality and Temperature

in the following equations. The heat losses consist of three parts: reflected radiation, q_r; emitted radiation, q_e; and convective heat losses, q_c. The heat losses may be expressed as follows:

$$q_L = q_r + q_e + q_c \tag{2a}$$

$$q_r = (1-\alpha)\, D_o\, \Delta Z (q_{i,j-1} + q_{i,j})/2 \tag{2b}$$

$$q_e = F\,\varepsilon\sigma\Delta Z \int_{-\pi/2}^{\pi/2} T_{wo}^{\,4}\, \frac{D_o}{2}\, d\theta$$

$$= F\,\varepsilon\sigma\Delta Z\, \pi \frac{D_o}{2}\, T_{wo,2} \tag{2c}$$

$$q_c = h_c\, \Delta Z \int_{-\pi/2}^{\pi/2} \left(T_{wo} - T_{amb}\right) \frac{D_o}{2} \cos\theta\, d\theta$$

$$= h_c\, \Delta Z\, D_o\, (T_{wo,2} - T_{amb}) \tag{2d}$$

The absorbtivity, α, and emissivity, ε, are set equal to 0.95 and 0.90, respectively, corresponding to values for Pyromark paint.[1] The radiation view factor, F, was determined equal to 0.64 by using a chart of differential area shape factors for two-dimensional radiation exchange.[5] The convective heat transfer coefficient, h_c, is based on a Sandia evaluation[6] as 0.666 W/M^2K (3.78 $Btu/h{\cdot}ft^2F$) for the pilot plant and 0.634 W/m^2K (3.60 $Btu/h{\cdot}ft^2F$) for the commercial plant. The ambient temperature, T_{amb}, is selected equal to 28°C (82°F). The evaluation of the integrals in Equations (2c) and (2d) with an average temperature, $T_{wo,2}$, is a simplification of the analysis to avoid accounting directly for circumferential effects in the overall thermal performance code. Circumferential effects are taken into account as explained later.

The inside and outside wall temperatures are determined from application of the heat transfer rate equations:

$$q_a = h_i \, C_1 \, \pi D_i \, \Delta Z \, (T_{wi,1} - T_H) \tag{3}$$

$$q_a = U \, C_1 \, \pi D_i \, \Delta Z \, (T_{wo,1} - T_H) \tag{4a}$$

$$\frac{1}{U} = \frac{1}{h_i} + \frac{D_i}{2k} \ln \frac{D_o}{D_i} \tag{4b}$$

The heat transfer coefficient, h_i, for the inside tube surface is determined from empirical correlations for different boiling regimes as summarized in Table 1. The selected correlations have all been used in other steam generator analyses. The correlations are based on uniform circumferential heating and have data bases that include the current operating points or are as close to the operating points as could be found. Because of the large range in mass flux for the different proposed operating conditions, several different correlations are selected for CHF and film boiling. A film boiling correlation for non-equilibrium flow after Groeneveld and Delorme[12] is selected to apply to the low mass flux for the pilot plant for both the maximum and minimum panel power conditions. For the commercial plant, the same film boiling correlation is selected for the minimum power case; however, for the maximum panel power, the mass flux is sufficiently high so that the Bishop, et al.[13] film boiling correlation for equilibrium flow is selected.

The parameter C_1 in Equations (3) and (4a) is included in the rate equations to permit a variation of the fraction of tube surface over which thermal conditions are considered uniformly distributed in the circumferential direction. The inner wall temperature, $T_{wi,1}$, and the outer wall temperature, $T_{wo,1}$, are considered average temperatures associated with a circumferential surface area fraction corresponding to C_1.

TABLE 1 - Heat Transfer Correlations Used in GE Solar Receiver Thermal Analysis Program, STAP

REGION	AUTHORS OF CORRELATION
Preheat	Engineering Sciences Data Unit (1967, U.K.), Ref. 7
Subcooled boiling and nucleate boiling	Thom, et al. (1965, U.K.), Ref. 8
CHF - Maximum panel power	
- Pilot plant	Wolf, France & Holmes (1977, GE), Ref. 9
- Commercial plant	France, et al. (1978, ANL), Ref. 10
- Minimum panel power	Biasi, et al. (1967, Italy), Ref.11
Film boiling	
- Maximum panel power	
- Pilot plant	Groeneveld & Delorme (1976, AECL), Ref. 12
- Commercial plant	Bishop, Sandberg & Tong (1965, W), Ref. 13
- Minimum panel power	Groeneveld & Delorme (1976, AECL), Ref. 12
Superheat	Heineman (1960, ANL) Ref. 14
Tube Thermal Conductivity	Huntington Alloy Handbook, Ref. 15

The outer wall temperature, $T_{wo,2}$, used in the heat loss Equations (2c) and (2d) is expressed in terms of $T_{wo,1}$, and the fluid temperature, T_H, as:

$$T_{wo,2} = T_H + C_2 (T_{wo,1} - T_H) \tag{5}$$

The maximum outer wall temperature, $T_{wo,3}$, is similarly expressed as:

$$T_{wo,3} = T_H + C_3 (T_{wo,1} - T_H) \tag{6}$$

Coefficients C_1, C_2, and C_3 are introduced to account in a simplified manner for circumferential heating effects.

The axial variation of temperature and pressure of the fluid is determined from a step-wise application of an energy balance equation. Based on the assumption that tube wall axial conduction heat transfer is negligible, the heat from Equation (1) must be absorbed by the water/steam flowing inside the tube under steady-state conditions. An energy balance yields:

$$H_j - H_{j-1} = q_{a,j}/W \tag{7}$$

For water/steam, the enthalpy, H, can generally be expressed as a function of temperature and pressure.

For single-phase fluid:

$$H = g_1 (T_H, P) \tag{8a}$$

For two-phase fluid:

$$H = g_2 (T_H, X) \tag{8b}$$

$$T_H = g_3 (P) \tag{8c}$$

Since pressure is coupled with the thermal equations through Equations (8), a momentum equation is needed to complete the solution of the thermal-hydraulic problem.

The friction, acceleration, and gravity terms of the momentum equation for steady two-phase separated flow with constant mass flux and small Δz are:[16]

$$\Delta P_{fr} = - \frac{fG^2}{2D_i g_c} (v_f \phi^2_{fo}) \Delta Z \tag{9}$$

$$\Delta P_{ac} = - \frac{G^2}{g_c} \Delta \left(\frac{X^2 v_g}{\alpha_v} + \frac{(1-X)^2}{(1-\alpha_v)} v_f \right) \tag{10}$$

$$\Delta P_{gr} = - \frac{g}{g_c} \left(\alpha_v \rho_g + (1- \alpha_v) \rho_f \right) \Delta Z \tag{11}$$

The coefficient of friction, f, is calculated using an approximation to the Moody chart:[17]

$$f = 0.0055 \left(1 + (20{,}000 \frac{\varepsilon_r}{D_i} + \frac{10^6}{Re}) ^{1/3} \right) \tag{12}$$

The two-phase multipliers used are:

$$\text{For } X \leq 0 \qquad \phi^2_{fo} = 1 \tag{13}$$

$$\text{For } 0 < X \leq X_c \qquad \phi^2_{fo} = \left(1 + \left(\frac{q''}{G}\right)^{0.7}\right)\phi^2_{hom} \tag{14}$$

$$\text{For } X_c < X \leq 1 \qquad \phi^2_{fo} = \left(1 - \left(\frac{1-X}{1-X_c}\right)^{1/n}\right)^n \left(\frac{v_g}{v_f} - \phi^2_{fo,\, X_c}\right) + \phi^2_{fo,X_c} \tag{15}$$

$$\text{where } n = \frac{G}{0.94 \times 10^6} \text{ for G in lb/h-ft}^2$$

The film boiling two-phase multipliers, ϕ^2_{fo}, for $X_c < X \leq 1$ was developed from data presented by Miropol'skii.[18] The value for the nucleate boiling term is after Tarasova[16] for low qualities and matches the Miropol'skii data well up to the CHF quality. After CHF, the two-phase multiplier is no longer the almost linear function of quality it is before CHF, but follows the curve of Equation (15) with "n" a function of mass flux. The pressure drop correlations used in the analytical model are summarized in Table 2.

The void fraction, α_v, in Equations (10) and (11) is related to the slip ratio, S, as follows:

$$\alpha_v = \frac{v_g X}{V_g X + (1-X)\, V_f\, S} \tag{16}$$

The slip ratio is calculated using the following correlation:

$$S = \frac{(102\, e^{-0.6P_r} - 1.1)\,(X + 0.01)}{\sqrt{Fr} + 1.88} + 1.1 \tag{17}$$

TABLE 2 - Correlations Used to Calculate Two-Phase Pressure Drop in Solar Receiver Thermal Analysis Program, STAP

	AUTHORS OF CORRELATION
Slip ratio	Marchaterre and Hoglund, Ref. 19
Coefficient of friction	Moody, Ref. 17
Two-phase multipliers	
Nucleate boiling	Tarasova, Ref. 16
Film boiling	Miropol'skii, Ref. 18

Here, P_r is the thermodynamic reduced pressure and Fr is the Froude number. This slip ratio equation is a close approximation to a correlation presented in graphical form by Marcharaterre and Hoglund.[19]

The pressure drop across each element is calculated from the momentum equation components, Equations (9) through (11). The steam/water properties in the momentum equation for each element are determined from Equation (8) using the conditions at the upstream end of the element, node j-1.

2.2 DESCRIPTION OF THERMAL PERFORMANCE, CODE, STAP

The thermal-hydraulic analysis computer program STAP was developed to predict thermal performance of a panel of a solar-electric central receiver based on the analytical model presented in the previous sub-section. Given any mass flow rate, incident radiation, and inlet conditions this code will predict both outer and inner tube wall temperature distributions along the tube, the pressure drop, the maximum outer tube wall temperature, and the water/steam properties, such as, quality, temperature and pressure along the tube length. Since non-linear terms are in the model equations, an iteration scheme was selected to solve the equations.

Some of the key characteristics are discussed below:

1. Use $T_{wo,1,j-1}$, $T_{H,j-1}$, and P_{j-1} derived for the previous node to calculate $T_{wo,2,j}$ from Equation (5).

2. Substitute the newly derived $T_{wo,2,j}$ into Equation (2) to calculate the heat absorbed by water/steam from Equations (1) and (2) and the current water/steam enthalpy, H_j, from Equation (7).

3. Depending on whether the steam/water is single-phase or two-phase, use either Equation (8a) or Equations (8b) and (8c) to determine the current steam/water temperature $T_{H,j}$ and quality X_j.

4. Calculate $T_{wo,1,j}$ from Equations (3) and (4) using the newly derived $T_{H,j}$.

5. Use the newly calculated $T_{H,j}$ and $T_{wo,1,j}$ to update $T_{wo,2,j}$ with Equation (5) as in step 1.

6. The whole iteration process, steps 1 to 5, continues until the calculated $T_{wo,1,j}$ for consecutive interations are within some specified tolerance.

7. After the tube wall temperature converges, substitute all newly derived thermal properties of water/steam into Equations (9) through (17) to calculate the current water/steam pressure P_j. The whole process can be marched from the tube entrance to the tube outlet.

2.3 DETERMINATION OF TWO-DIMENSIONAL EFFECTS COEFFICIENTS

The coefficient C_1 in the heat transfer rate equations, Equations (3) and (4), was initially varied between 0.5 and 1.0 for the pilot plant maximum heat flux case and performance predictions were, subsequently, made with STAP. The thermal conditions predicted at CHF and at the maximum temperature location were then used as boundary conditions for a two-dimensional finite element model of a half section of the tube (r-θ plane). The finite element model corresponds to Model A presented later in this report as part of the thermal-stress cycling analysis. Inner and outer wall temperature distributions were determined by running the model on the latest GE thermal-stress analysis code TASA-01.[20] The results of these runs showed that, even though the heat flux on the outer wall surface was confined to the top side of the tube receiving incident solar radiation, the heat flux on the inner wall was nonuniformly distributed all around the tube. Consequently, C_1 was selected equal to 1.0 for the final performance evaluation.

The values of C_2 and C_3 were determined by first running STAP with C_1 = 1.0 and estimated values of C_2 and C_3. The predicted thermal conditions at CHF were then used as boundary conditions for the two-dimensional finite element model of the tube which was, subsequently, run on TASA-01. The temperature $T_{wo,1}$ was then determined as an integrated average over the total outer surface and $T_{wo,2}$, as an integrated average over the top portion of the outer surface area which is exposed to solar radiation. Values of C_2 and C_3 were then determined from Equations (5) and (6). This process was iterated between STAP and TASA-01 to obtain final values.

Theoretically this type of correction for the tube wall temperatues should be applied to each node. However, since the conditions at the CHF locations are most important for the subsequent thermal-stress cycling analysis, the temperatue coefficients were evaluated only at the CHF locations. These coefficients were then applied over the total tube length.

2.4 THERMAL PERFORMANCE RESULTS

2.4.1 Model Verification

The thermal performance model was verified by predicting the thermal performance for a boiler tube experimentally tested by Rocketdyne.[21] The single boiler tube, 7.8 mm (0.305 in.) i.d., 19.8 m (65 ft) long, made of 304 SS, was heated with radiant electrical heaters. For the evaluation with STAP, the CHF correlation recently determined from GE experimental work[9] and the non-equilibrium film boiling correlation after Groeneveld and Delorme[12] were used. The other heat transfer correlations used for the evaluation correspond to the summary given in Table 1. The experimental heat flux was reduced 5% to obtain an energy balance and to account for possible thermal losses. Values of C_2 and C_3 were assumed to be the same as determined for the pilot receiver panel with maximum heat flux conditions. Predicted temperature and mass quality distribuitions are shown in Figure 5a. The predicted water/steam temperature agrees well with the measured temperature over the complete length

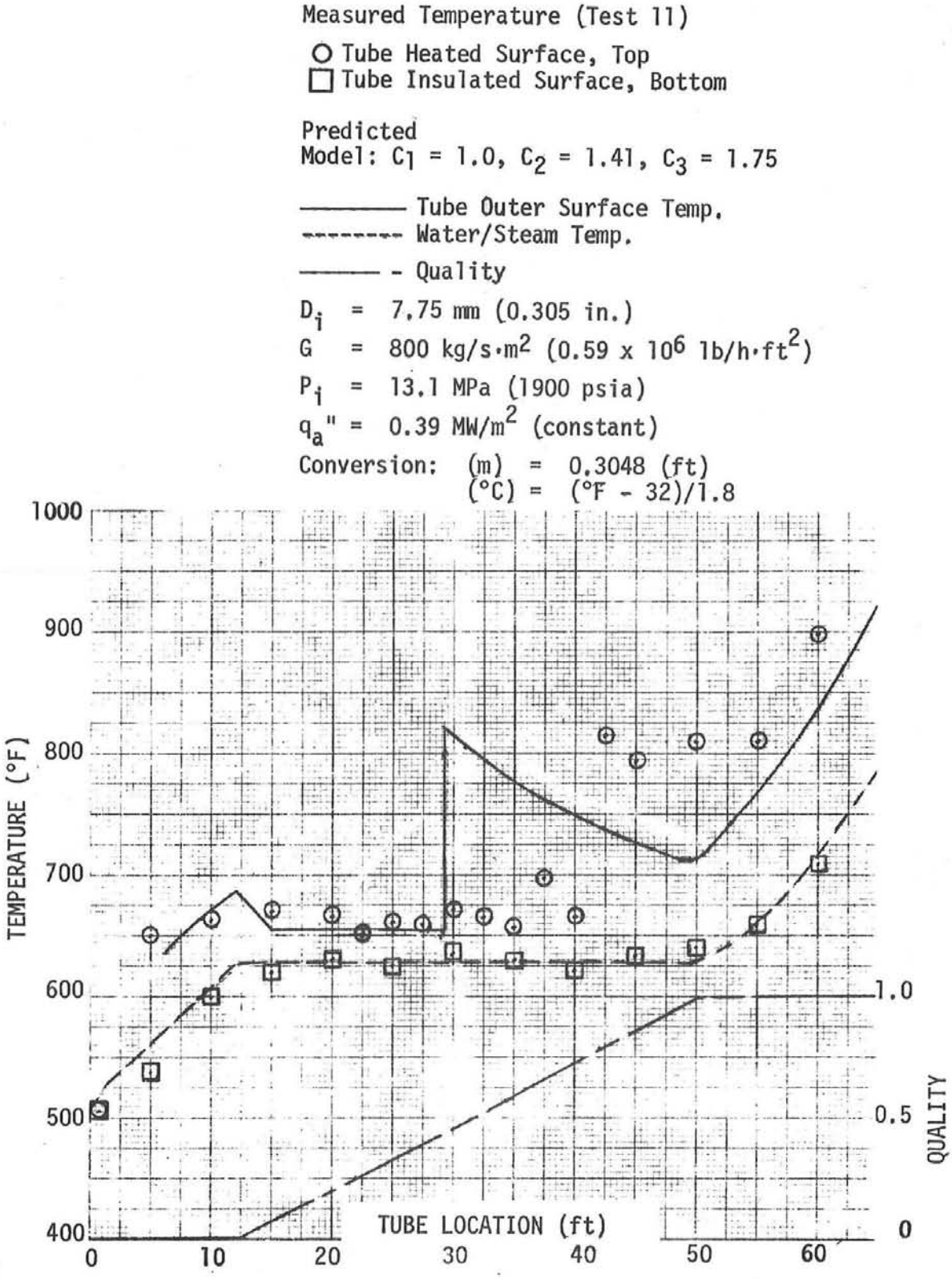

Figure 5a. X_c Based on GE CHF Correlation

Figure 5. Comparison of Thermal Performance Predictions with STAP and Experimental Data (Ref. 20, Test 11)

of the heated section. The predicted outer wall temperatue is $T_{wo,3}$ which corresponds to the maximum outer wall temperature. This predicted maximum temperature agrees well with the measured temperature near the bottom of the heated section. However, a significant difference exists in the region immediately after CHF. The CHF location is indicated by an abrupt increase in outer wall temperature at 8.9 m (29.2 ft) corresponding to a predicted quality of 0.44. The experimental outer wall temperature indicates that CHF occurs at 12.2 m (40.0 ft) corresponding to a quality of 0.74. The disagrement between the predicted and experimentally indicated CHF quality and locations may be the result of the effect of nonuniform circumferential heating. All of the correlations used are based on uniform circumferential heating. Additional experimental data are required to verify current correlations or provide new correlations for the severe circumferential nonuniform heating associated with solar boiler tubes. An additional calculation was performed with STAP with the CHF quality adjusted to 0.74 to correspond to the experimentally indicated quality. Results from this run are presented in Figure 5b with the resulting agreement in the predicted and experimental CHF location.

2.4.2 Receiver Panel Performance Predictions

The thermal performance predicted for the receiver tubes with maximum heat flux are presented in Figures 6 and 7 for the pilot plant, and Figures 8 and 9 for the commercial plant. The results are summarized in Table 3. For the pilot plant the mass flux is reduced by 12% from a value of 460 kg/m^2s (0.339 X 10^6 $lb/h \cdot ft^2$) provided by Sandia to a final value of 405 kg/m^2s (0.299 X 10^6 $lb/h \cdot ft^2$) to maintain the outlet temperature at a specified value of 516°C (960°F). The inlet pressure of 10.54 MPa (1528 psia) is also slightly reduced from a value of 10.69 MPa (1550 psia) provided by Sandia to maintain the outlet pressure at a specified value of 10.45 MPa (1515 psia). For the commercial plant a reduction in mass flux of only 5% was required to maintain the specified outlet temperature. However, the inlet pressure had to be increased significantly to 13.24 MPa (1920 psia) to maintain the specified outlet pressure at 11.14 MPa (1615 psi). This adjustment was necessary as the GE predicted pressure drop of 2.1 MPa (300 Psi) is three times as large as the value initially provided by Sandia.

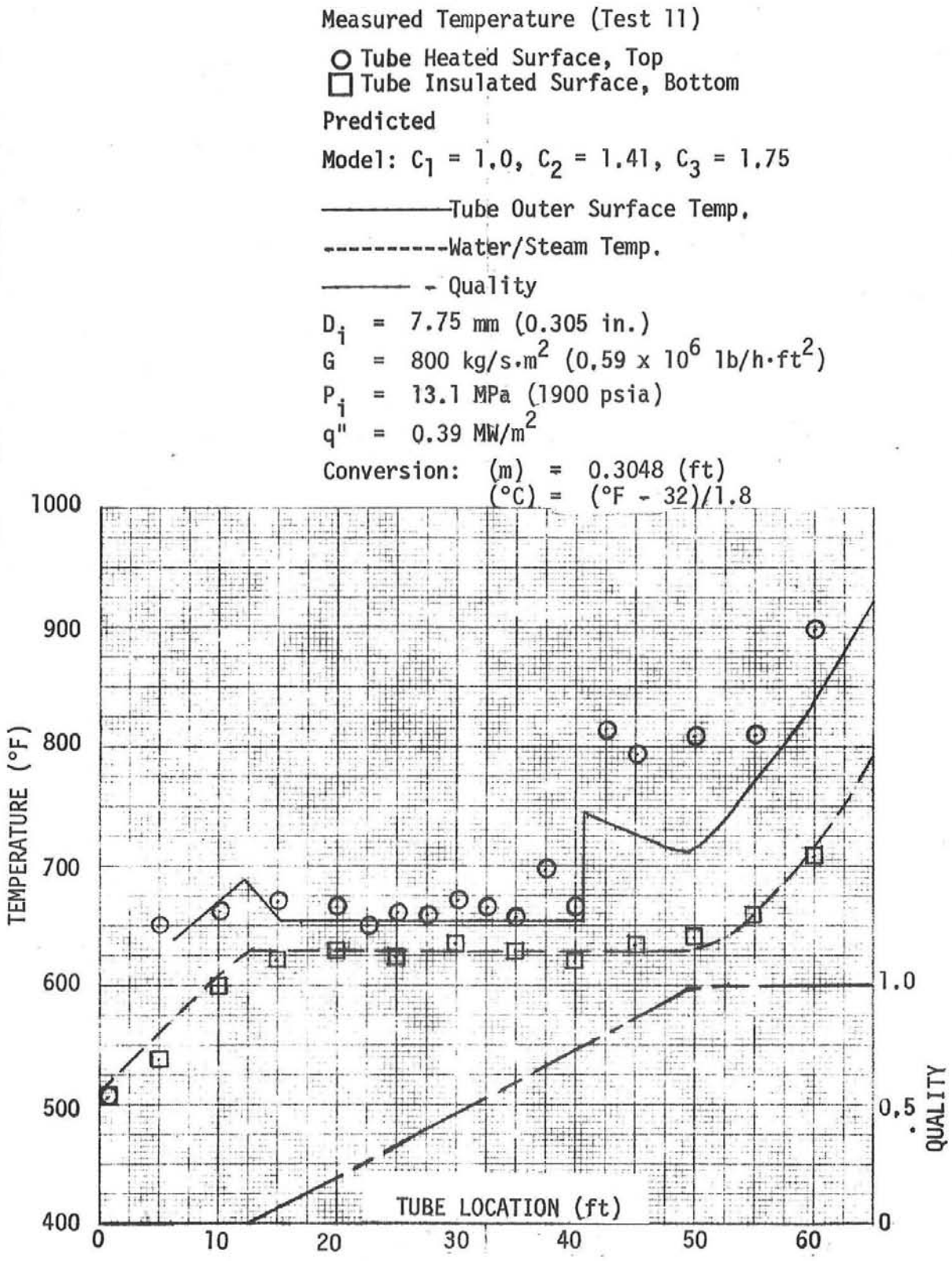

Figure 5b. X_c = 0.74

Figure 5. Comparison of Thermal Performance Predictions with STAP and Experimental Data (Ref. 20, Test 11)

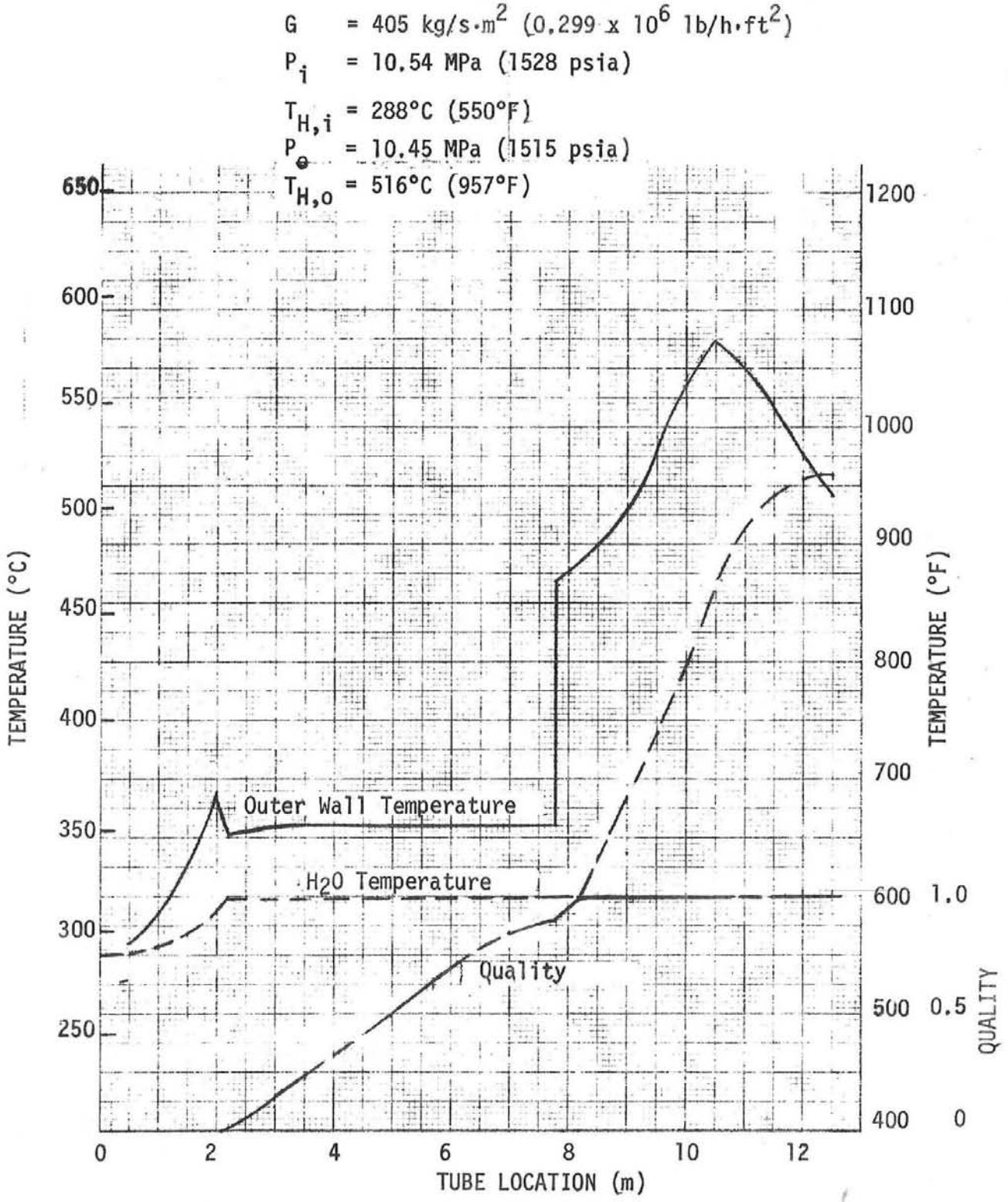

Figure 6. Predicted Performance Profiles for the Maximum Power Boiler Panel for the Pilot Plant Receiver

$G = 405\ kg/s \cdot m^2\ (0.299 \times 10^6\ lb/h \cdot ft^2)$

$P_i = 10.54\ MPa\ (1528\ psia)$

$Q_a/Q_{inc} = 0.86$

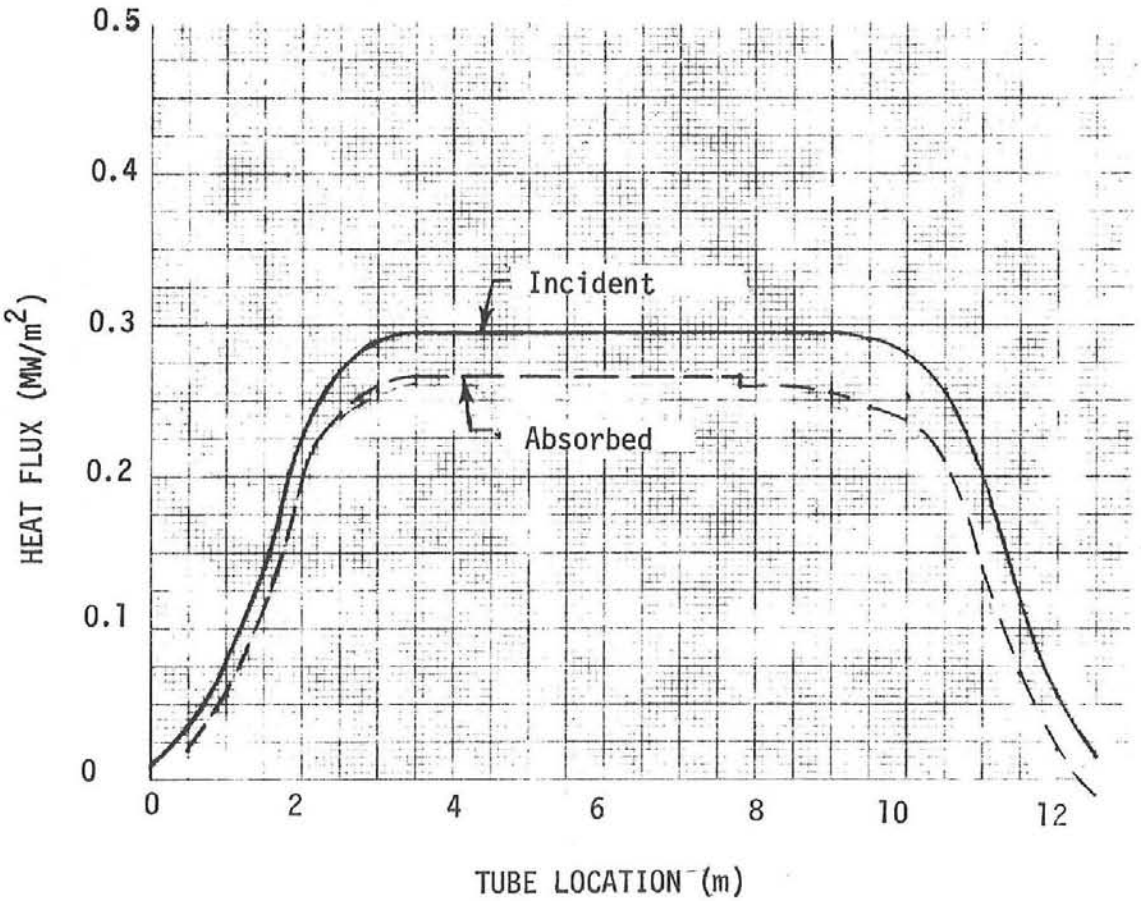

Figure 7. Heat Flux Profiles for the Maximum Power Boiler Panel for the Pilot Plant Receiver

G = 2210 kg/s·m^2 (1.63 x 10^6 lb/h·ft^2)

P_i = 13.24 MPa (1920 psia)

$T_{H,i}$ = 274°C (526°F)

P_o = 11.14 MPa (1615 psia)

$T_{H,o}$ = 516°C (963°F)

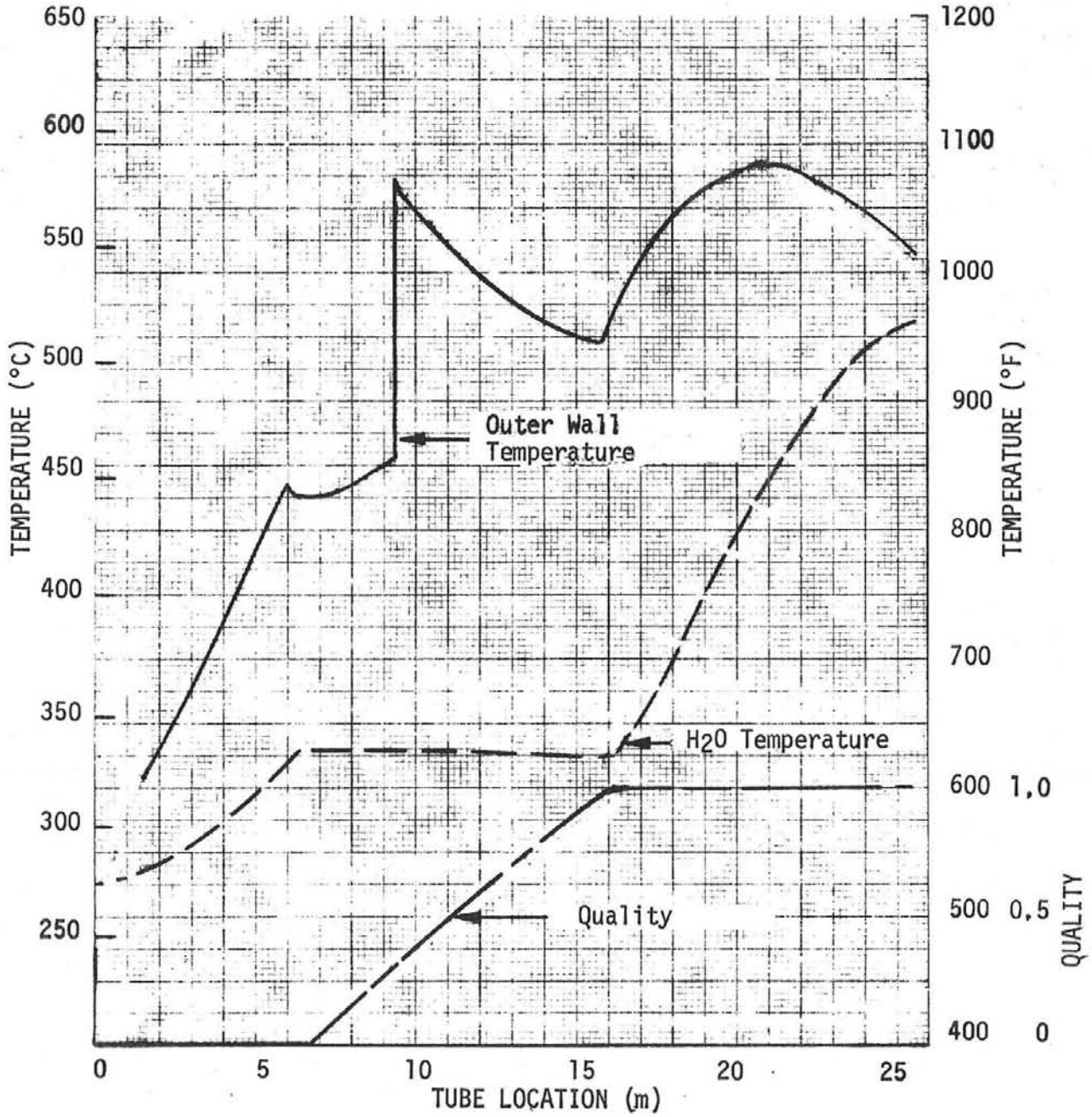

Figure 8. Predicted Performance Profiles for the Maximum Power Boiler Panel for the Commercial Plant Receiver

$G = 2210\ kg/s \cdot m^2\ (1.63 \times 10^6\ lb/hr \cdot ft^2)$

$P_i = 13.24\ MPa\ (1920\ psia)$

$Q_a/Q_{inc} = 0.91$

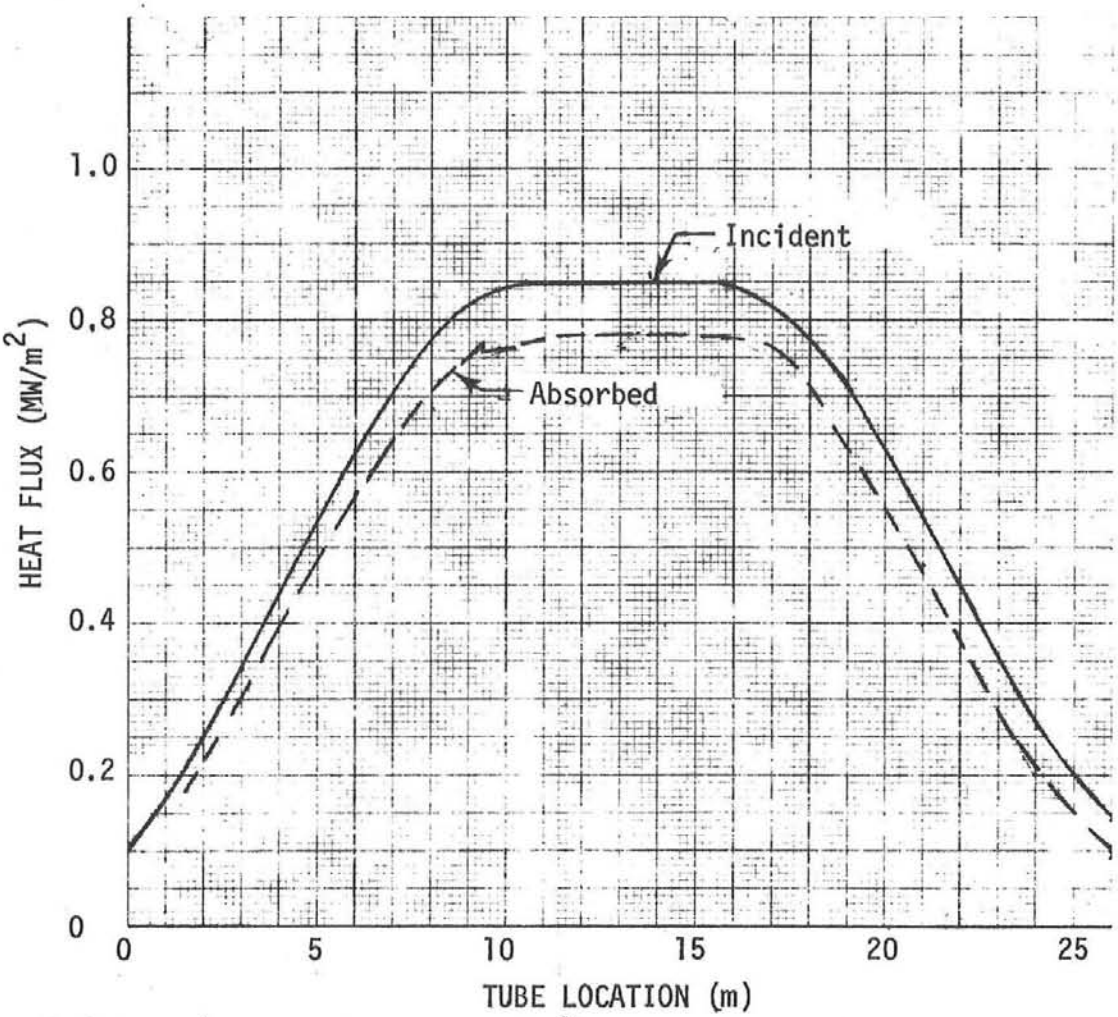

Figure 9. Heat Flux Profiles for the Maximum Power Boiler Panel for the Commercial Plant Receiver

Table 3 - Summary of Thermal Performance Analysis Results

Plant Heat Flux Condition	Pilot Maximum	Commercial Maximum	Commercial 80% Maximum	Pilot Minimum	Commercial Minimum
Tube					
Material	Incoloy 800	Incoloy 800	Incoloy 800	Incoloy 800	Incoloy 800
D_i mm	6.83	6.83	6.83	6.83	6.83
D_o mm	12.70	12.70	12.70	12.70	12.70
Length m	12.5	25.5	25.50	12.5	25.50
Model					
C_1	1.0	1.0	1.0	1.0	1.0
C_2	1.41	1.68	1.68	1.071	1.184
C_3	1.75	2.36	2.36	1.128	1.335
View Factor, F	0.64	0.64	0.64	0.64	0.64
Operating Conditions					
T_i °C	288	274	274	288	214
T_o °C	516	516	516	500	516
P_i MPa	10.54	13.24	12.60	10.47	10.32
P_o MPa	10.45	11.14	11.14	10.45	10.24
$q_{i,max}''$ MW/m^2	0.295	0.850	0.680	0.053	0.072
$q_{a,max}''$ MW/m^2	0.266	0.784	0.624	0.038	0.056
G $kg/s \cdot m^2$	405	2210	1750	32.6	97.9
(10^6 $lb/h \cdot ft^2$)	(0.299)	(1.63)	(1.29)	(0.024)	(0.0722)
$T_{wo,max}$ °C	578	586	568	612	592
X_c	0.89	0.30	0.33	1.00	1.00
$q_{a,ave}''$ MW/m^2	0.200	0.549	0.436	0.016	0.028
Q_a kW/tube	31.7	177.7	141.2	2.53	8.96
Q_a/Q_i	0.86	0.91	0.90	0.37	0.58

The predicted thermal conditions at CHF for the pilot and commercial receiver panels for maximum heat flux were used in subsequent thermal-stress cycling analysis to evaluate the tube fatigue life. The maximum incident heat flux of 0.295 and 0.85 MW/m^2 for the pilot and commercial plants resulted in corresponding maximum absorbed heat flux values of 0.266 and 0.784 MW/m^2, respectively. Analysis of a case with 80% maximum incident heat flux for the commercial plant receiver was conducted after the thermal-stress cycling analysis showed that the fatigue life for the commercial receiver tubes with 100% maximum heat flux was lower than the required 30-year design life. The results for the commercial receiver with 80% maximum incident heat flux are also summarized in Table 3.

The thermal performance predicted for the receiver tubes with minimum heat flux are presented in Figures 10 and 11 for the pilot plant and Figures 12 and 13 for the commercial plant. The results are also summarized in Table 3. For both cases, the heat losses exceed the incident heat flux near the tube outlet and result in negative absorbed heat flux values. The total absorbed heat flux is only 37 and 58% of the incident heat flux (see Table 3) for the pilot and commercial receiver panels, respectively. The steam outlet temperature for the pilot plant is 500°C (932°F) instead of the specified value of 516°C (960°F). This is the maximum outlet temperature achievable by varying the mass flux. The mass flux for the pilot plant was determined by iteration to achieve a steam outlet temperature as close as possible to 516°C, resulting in 32.6 kg/m^2s (0.024×10^6 $lb/h \cdot ft^2$) compared with a Sandia supplied value of 43.7 kg/m^2s (0.0322×10^6 $lb/h \cdot ft^2$). For the commercial case with minimum heat flux, Figures 12 and 13, the specified outlet temperature of 516°C is achieved with a mass flux of 97.9 kg/m^2s (0.0722×10^6 $lb/h \cdot ft^2$) compared with a Sandia supplied value of 116.3 kg/m^2s (0.0857×10^6 $lb/h \cdot ft^2$).

Results of the thermal analysis for both the maximum and minimum heat flux cases are used in dynamic stability evaluations described in a later section of this report.

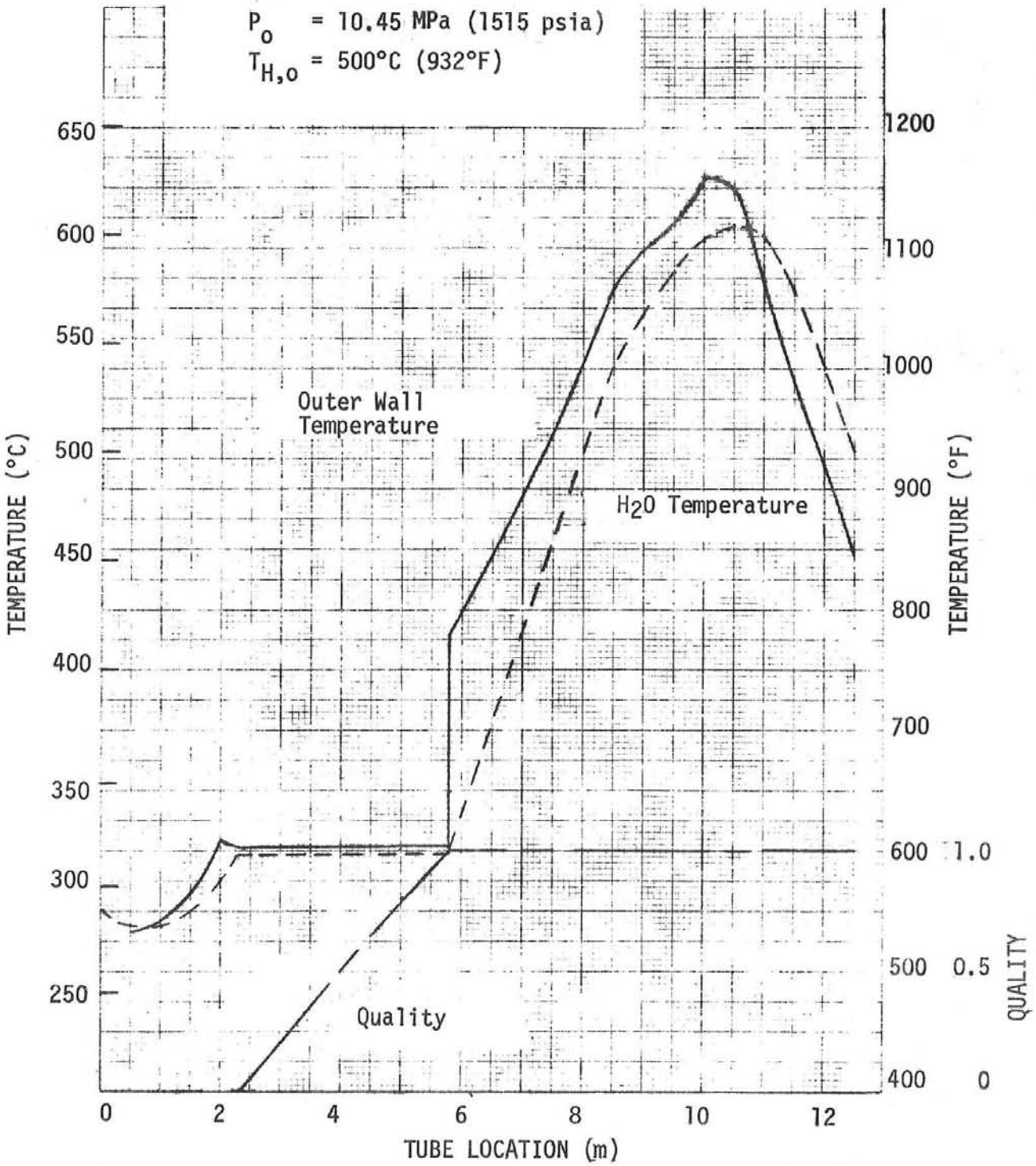

Figure 10. Predicted Performance Profiles for the Minimum Power Boiler Panel for the Pilot Plant Receiver

$G = 32.6\ kg/s \cdot m^2\ (0.024 \times 10^6\ lb/h \cdot ft^2)$

$P_i = 10.47\ MPa\ (1519\ psia)$

$Q_a/Q_{inc} = 0.37$

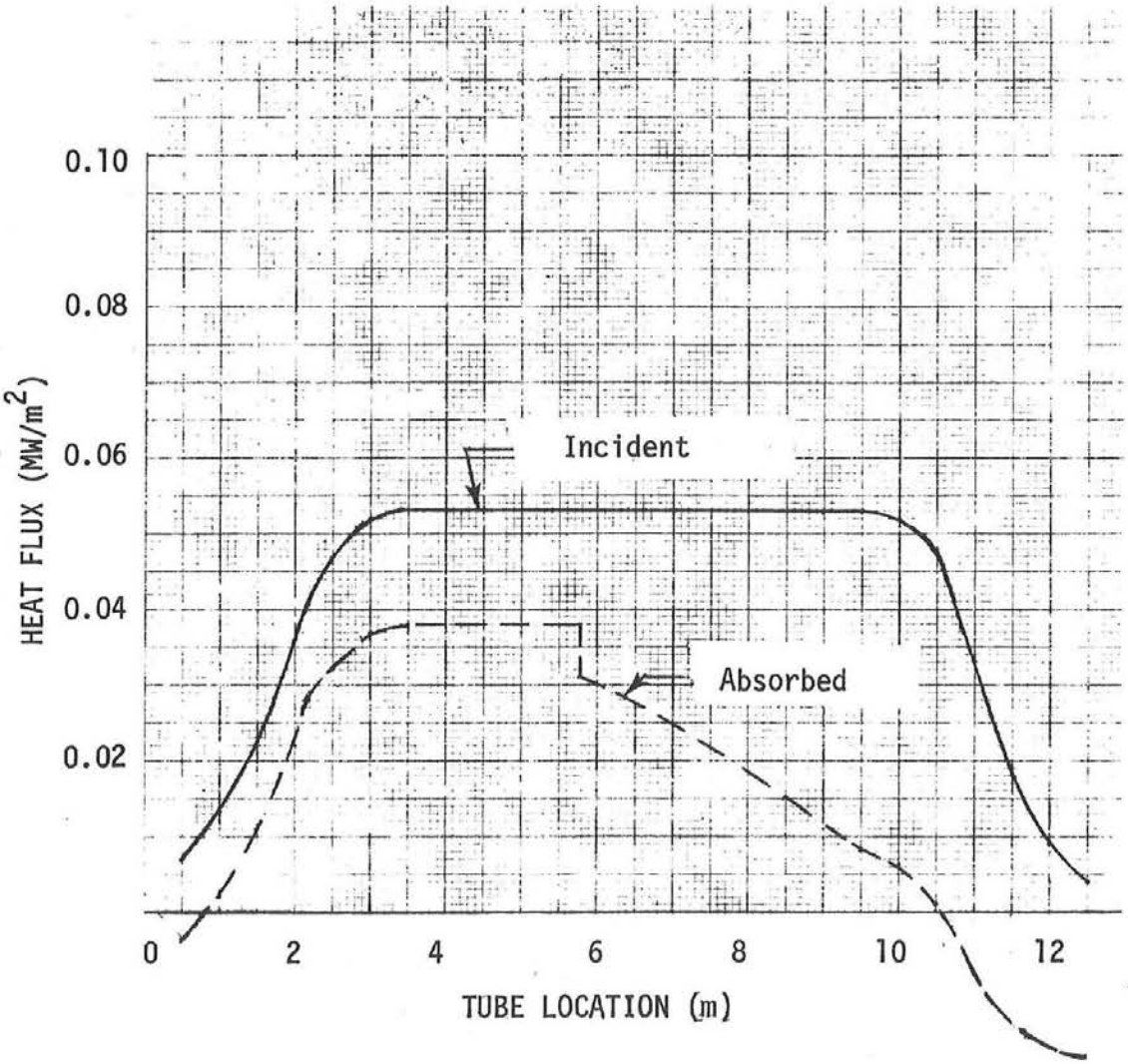

Figure 11. Heat Flux Profiles for the Minimum Power Boiler Panel for the Pilot Plant Receiver

G = 97.9 kg/s·m^2 (0.72 x 10^6 lb/h·ft^2)

P_i = 10.32 MPa (1947 psia)

$T_{H,i}$ = 214 °C (417°F)

P_o = 10.24 MPa (1485 psia)

$T_{H,o}$ = 516°C (962°F)

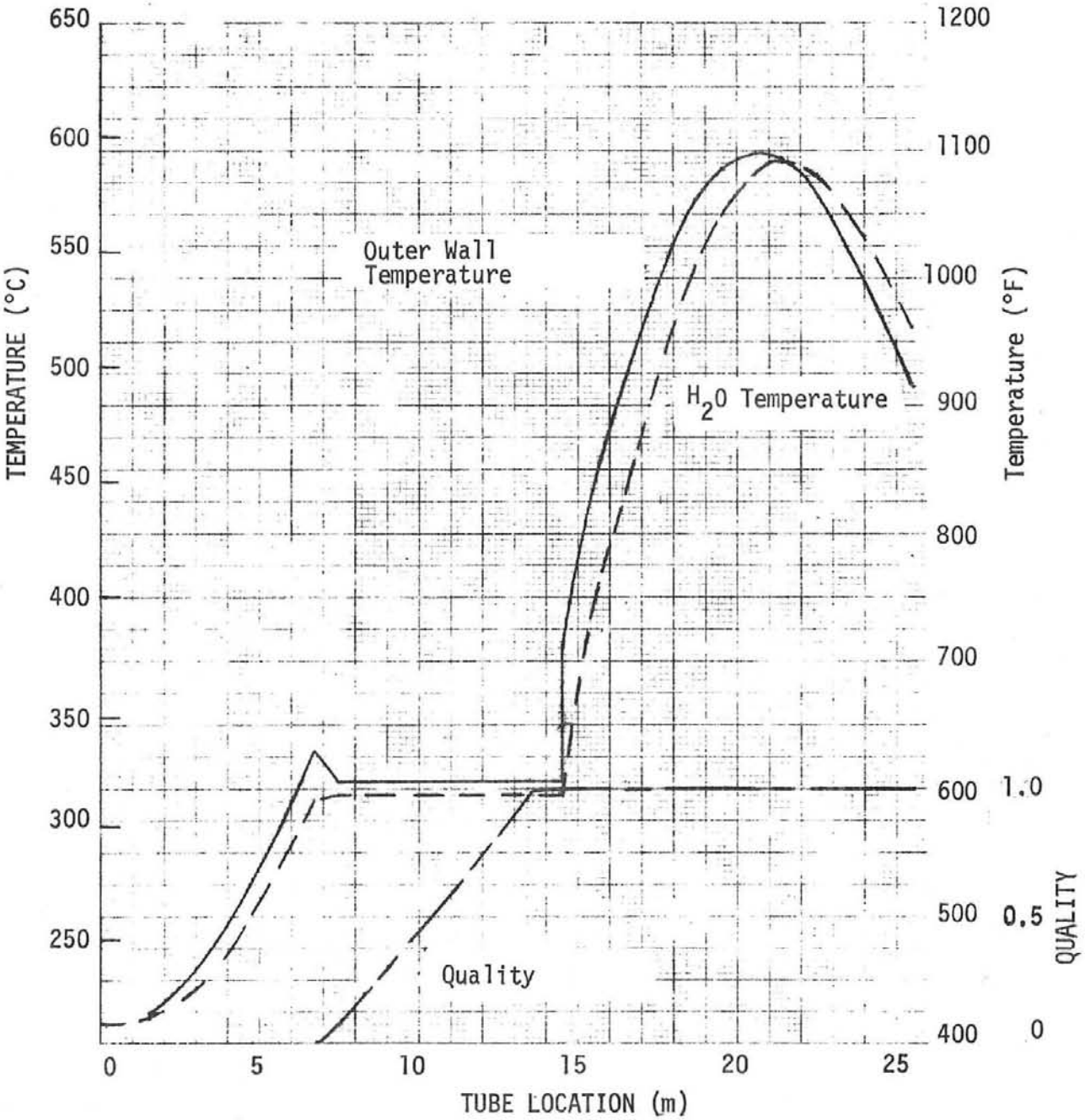

Figure 12. Predicted Performance Profiles for the Minimum Power Boiler Panel for the Commercial Plant Receiver

$G = 97.9\ kg/s \cdot m^2\ (0.072 \times 10^6\ lb/h \cdot ft^2)$

$P_i = 10.32\ MPa\ (1947\ psia)$

$Q_a/Q_{inc} = 0.55$

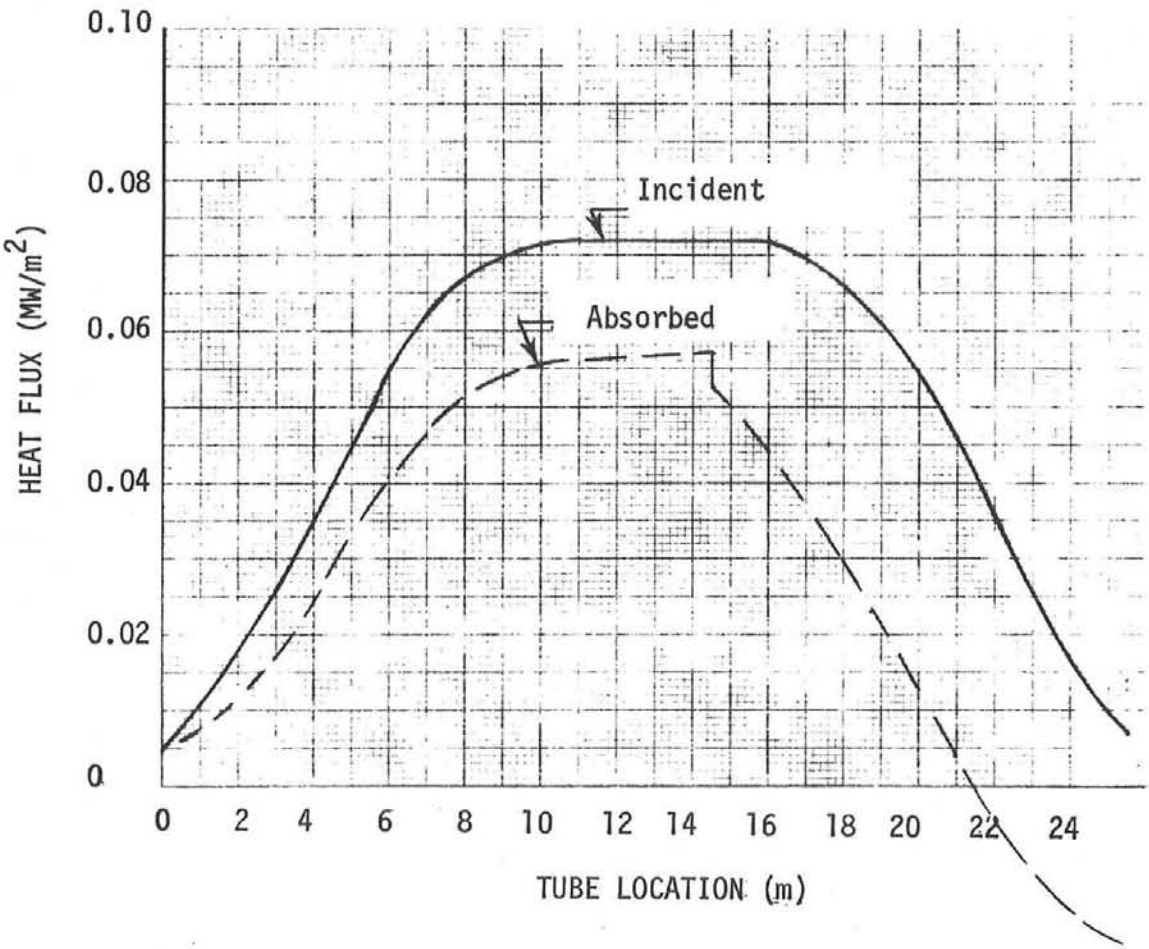

Figure 13. Heat Flux Profiles for the Minimum Power Boiler Panel for the Commercial Plant Receiver

3. THERMAL-STRESS CYCLING ANALYSIS

3.1 TRANSITION BOILING CHARACTERISTICS

The flow structure with CHF and a transition boiling region for a solar heated steam generator tube is illustrated in Figure 14. The flow preceeding the CHF point is dispersed annular flow which is characterized with a film of liquid water adjacent to the tube wall. The heat transfer process is very effective and is called nucleate boiling, even though bubble nucleation may be suppressed, by analogy to pool boiling. As the liquid film evaporates, it decreases in thickness and at CHF the film finally breaks up into rivulets and dry spots. After the rivulets have evaporated the wall is covered with bulk vapor containing entrained droplets, and heat transfer is by film boiling with a heat transfer coefficient considerably lower than for the wet region immediately preceeding CHF. Because of the locally unstable flow conditions of the transition boiling zone, oscillations occur, which, in turn, produce temperature oscillations in the tube wall temperatures and thermally induced stresses which can significantly reduce tube life and even lead to fatigue of the tube wall.

Temperature oscillations in the transition boiling zone were recently measured by Argonne National Laboratory (ANL) during a sodium heated generator test.[22] Thermocouples were embedded in the tube wall to measure temperature response. Two types of temperature oscillations were observed. Relatively high frequency fluctuations that are inherent in the transition boiling region were superimposed on lower frequency fluctuations with larger amplitude which are system induced. These temperatue fluctuations cause the stress oscillations and potential fatigue damage.[23-26] The frequency of the system induced fluctuations and the length of the transition boiling zone movement are peculiar to each individual system. Because of the current lack of system detail for the solar heated receiver subsystems, the analysis in this report is restricted to the effect of the inherent fluctuations in the transition

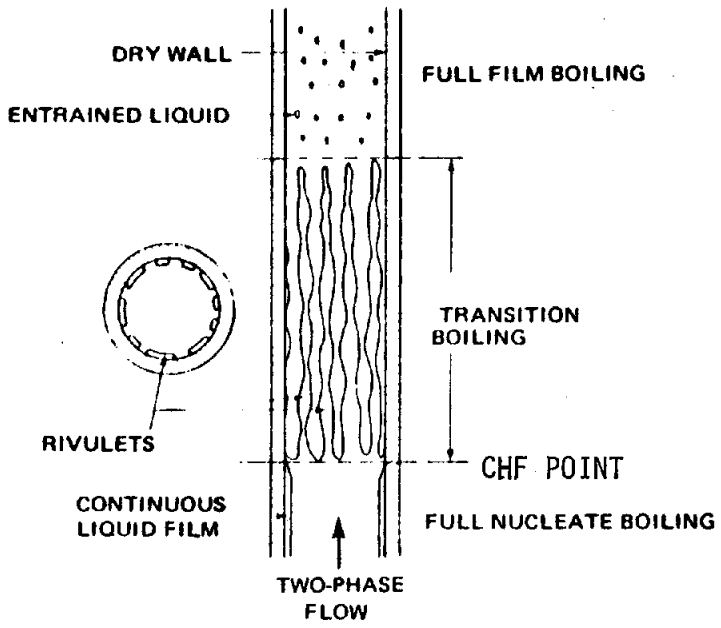

Figure 14. Elements of Transition Boiling Model

boiling zone. Typical inherent oscillations in the transition boiling zone from the ANL test are presented in Figure 15. The average period of these oscillations is about 3 seconds.

Temperature oscillations in the transition boiling zone were also recently measured by Rocketdyne during an electrical radiant-heated steam generator test.[21] Typical temperature oscillation measurements with a thermocouple mounted on the outside of the tube wall are shown in Figure 16. These oscillations have a period of about 8 seconds. Higher frequency oscillations may have been damped out by the tube wall. Also, because of the short duration of the temperature oscillations it is possible that the oscillations may have been influenced by small changes in the system parameters of water pressure, flow rate or inlet temperature to the test section.

For the thermal-stress cycling analysis presented in this report the 8-s period observed during the Rocketdyne test was selected as an upper limit and the 3-s period observed during the ANL test, as a possible lower limit. Consequently, the analysis is performed for both periods.

3.2 ANALYTICAL MODEL

A rivulet model[24,25] previously described for a sodium heated steam generator tube is used to describe the temperature oscillations in the transition boiling zone for the solar heated receiver tube. The temperature oscillations determined during the ANL test presented in Figure 15 were modeled with 3.7 rivulets and 21% wetness (circumference wetted by rivulets). Variation of the number of rivulets and the percent wetness has a direct effect on the temperature oscillations as shown in Figure 17.

Because of the lack of detailed temperature oscillation measurements for the solar heated receiver tubes, it was decided to use a similar rivulet spacing and the same percent wetness as determined for the ANL test tube for the current analysis. However, because solar heating is one-sided, two possible

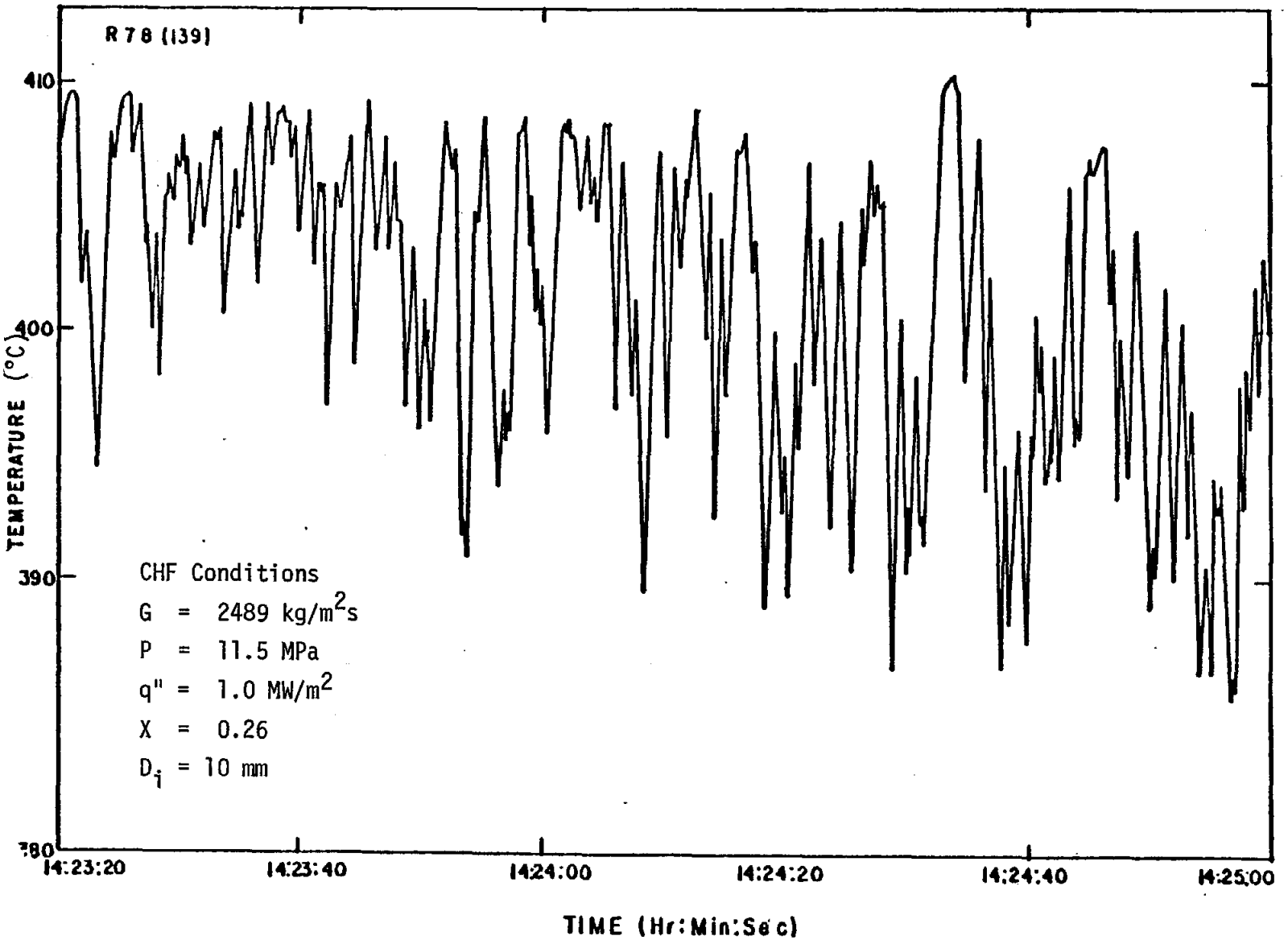

Figure 15. Example of CHF Temperature Oscillations During Sodium-Heated Steam Generator Test Simulating 64% CRBRP Power (Ref. 22, p58)

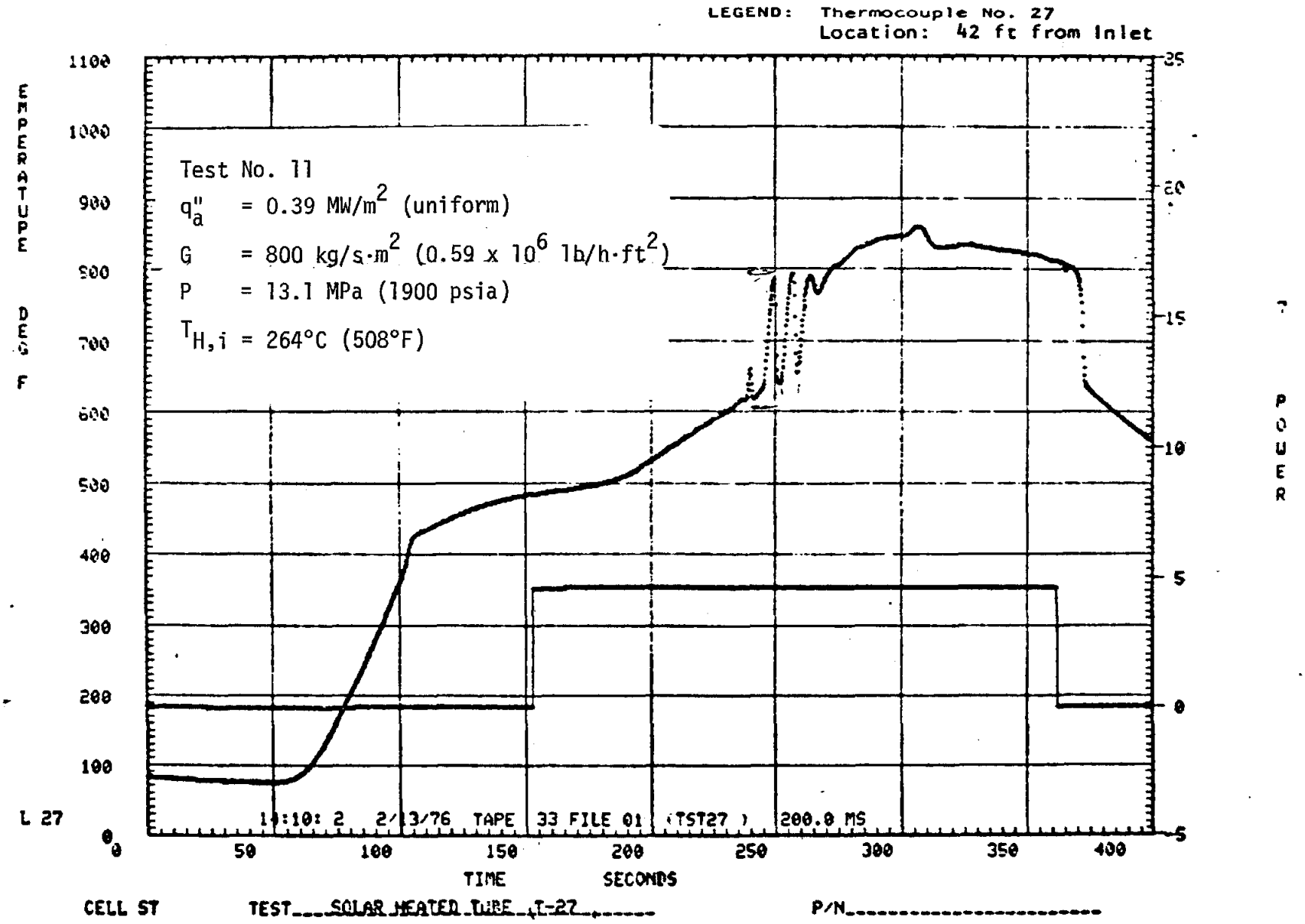

Figure 16. Example of CHF Temperature Oscillation During Radiant-Heated Steam Generator Test (Ref. 21, p92)

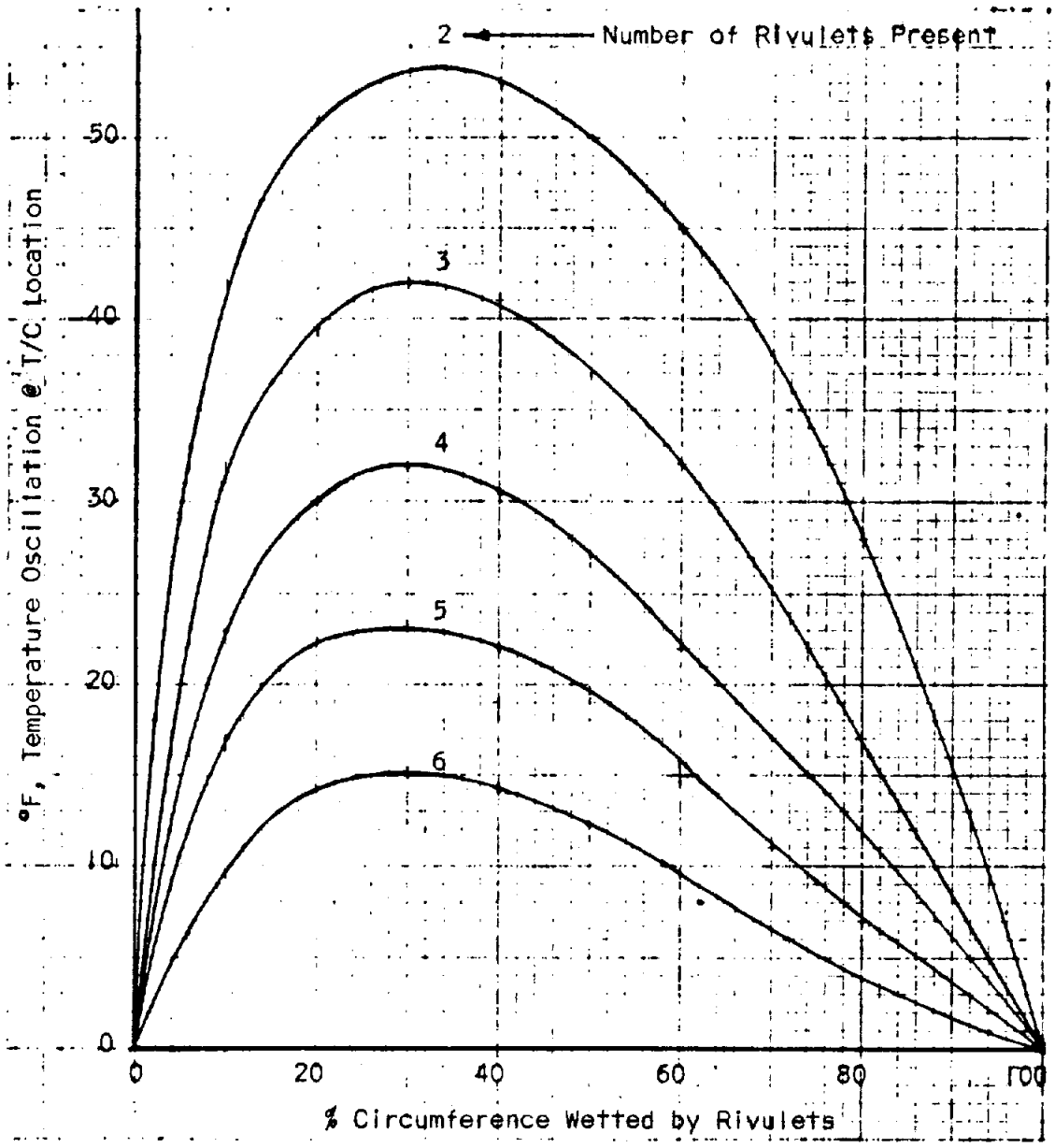

CONDITIONS:

1 - Simulated 64% Power In CRBRP
2 - Three Second Period of Oscillation
3 - Symmetrical Rivulet Patterns

Figure 17. Rivulet Model Characteristic (Ref. 24)

alternate rivulet arrangements are considered as illustrated in Figure 18. For Model A, the back side of the tube, which is insulated, remains wet at all times while two rivulets oscillate on the front side. For Model B, the front side is the same as for Model A; however, the back side now also has two oscillating rivulets, resulting in a total of four rivulets uniformly distributed around the circumference.

A general purpose finite element thermal-stress code, TASA-01,[20] was used for both the thermal studies and the subsequent cyclic stress evaluation. The two finite element models corresponding to Models A and B are shown in Figures 19 and 20, respectively. The variations of heat transfer coefficients on the inner surface are also illustrated in the Figures.

It was anticipated that the thermal and stress gradients would be higher at the inner surface of the tube during the temperature oscillations. Hence, the finite element models were constructed with smaller elements toward the inside wall. In the two-rivulet case, Model A, the back half of the tube is assumed not exposed to temperature oscillations and no large gradients of either temperature or stress were anticipated. Hence, large elements, as shown in Figure 19, were used for the back half of the tube for Model A to reduce computational costs.

Only elastic stress analysis was performed. This was based on the consideration that at a case of high cycle fatigue as for the CHF induced oscillations, elastic behavior must prevail for the tube to endure the large number of stress reversal cycles. Temperature dependent material properties (thermal conductivity, coefficient of thermal expansion, Young's modulus, and Poisson's ratio) were used to obtain accurate results. These properties were taken from the Huntington Alloy Handbook,[15] and the ASME B&PV Code Case 1592.[27]

It was also assumed that plane cross sections of the tube remain plane at all time and that the tube can expand and contract along the longitudinal direction (i.e., the generalized plane strain approach was used). This assumption

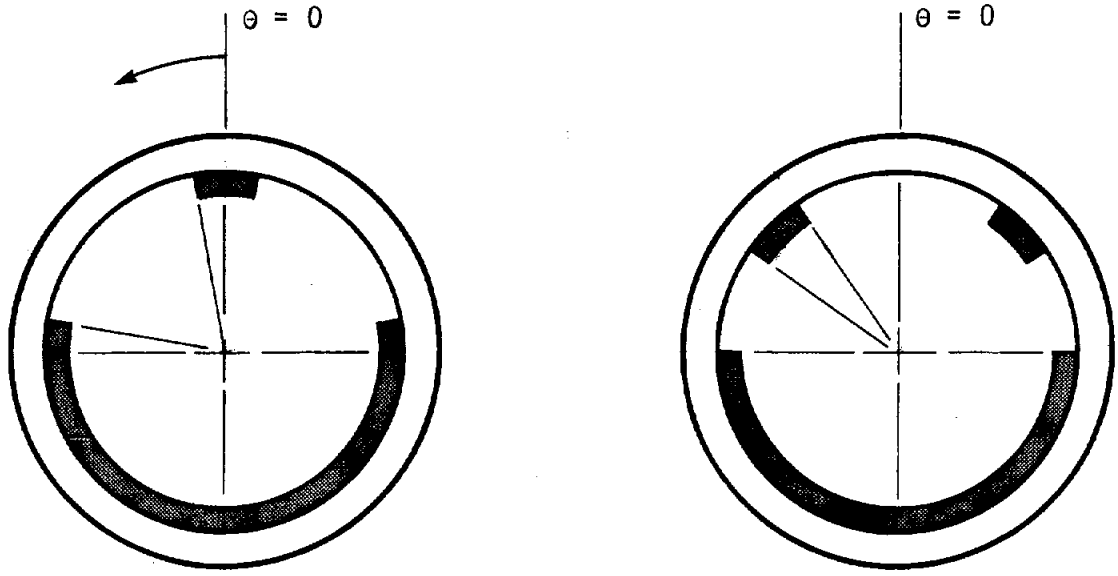

(a) Model A, 2 Rivulets

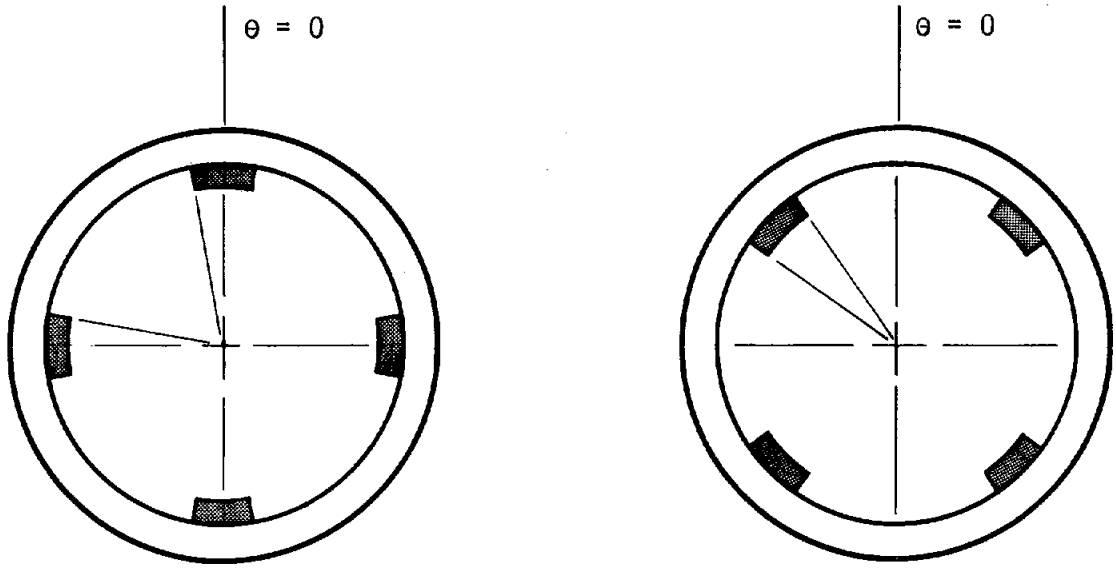

(b) Model B, 4 Rivulets

Figure 18. Rivulet Models for Evaluating Temperature Oscillations

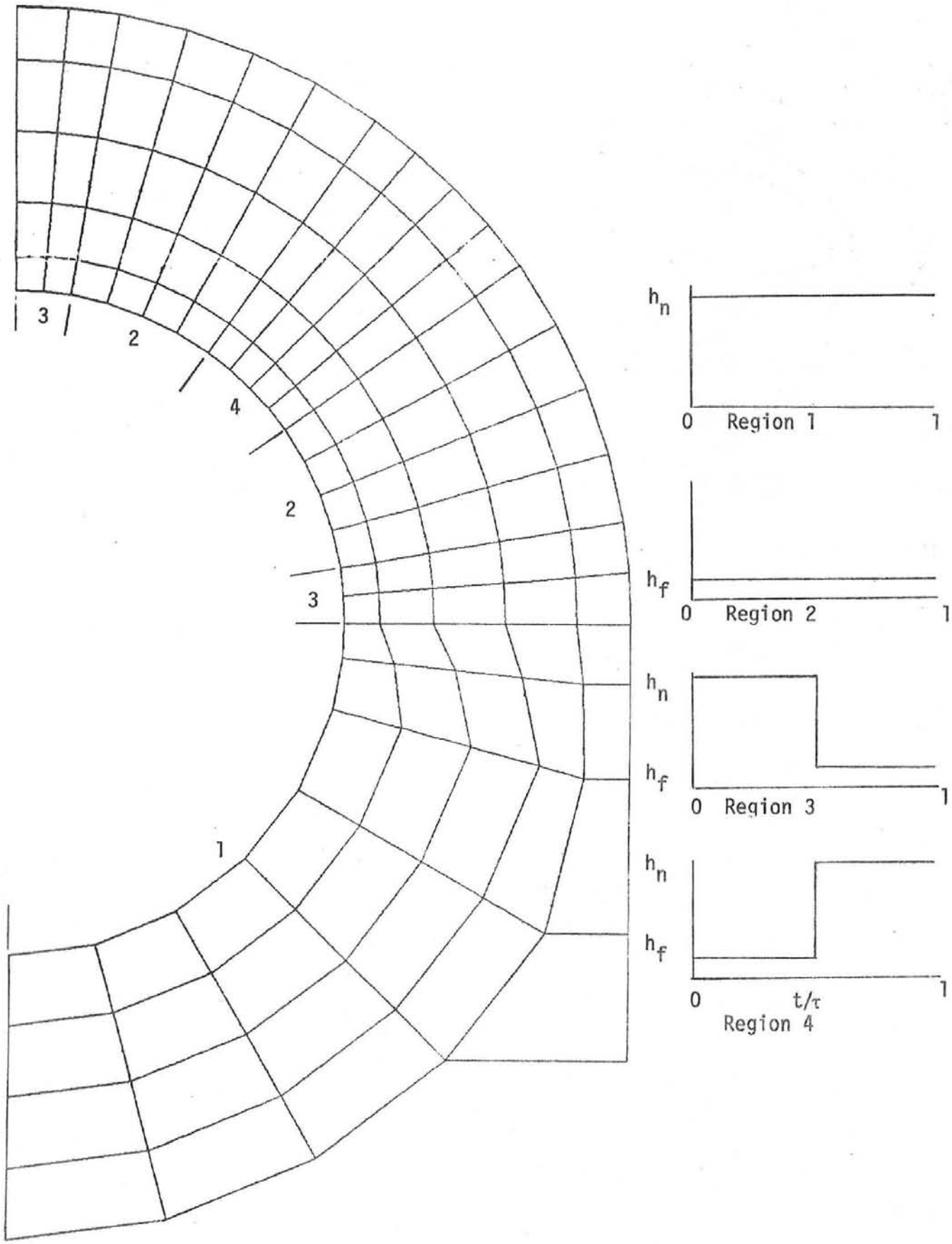

Figure 19. Finite Element Model A, 2 Rivulets, and Heat Transfer Coefficient Application

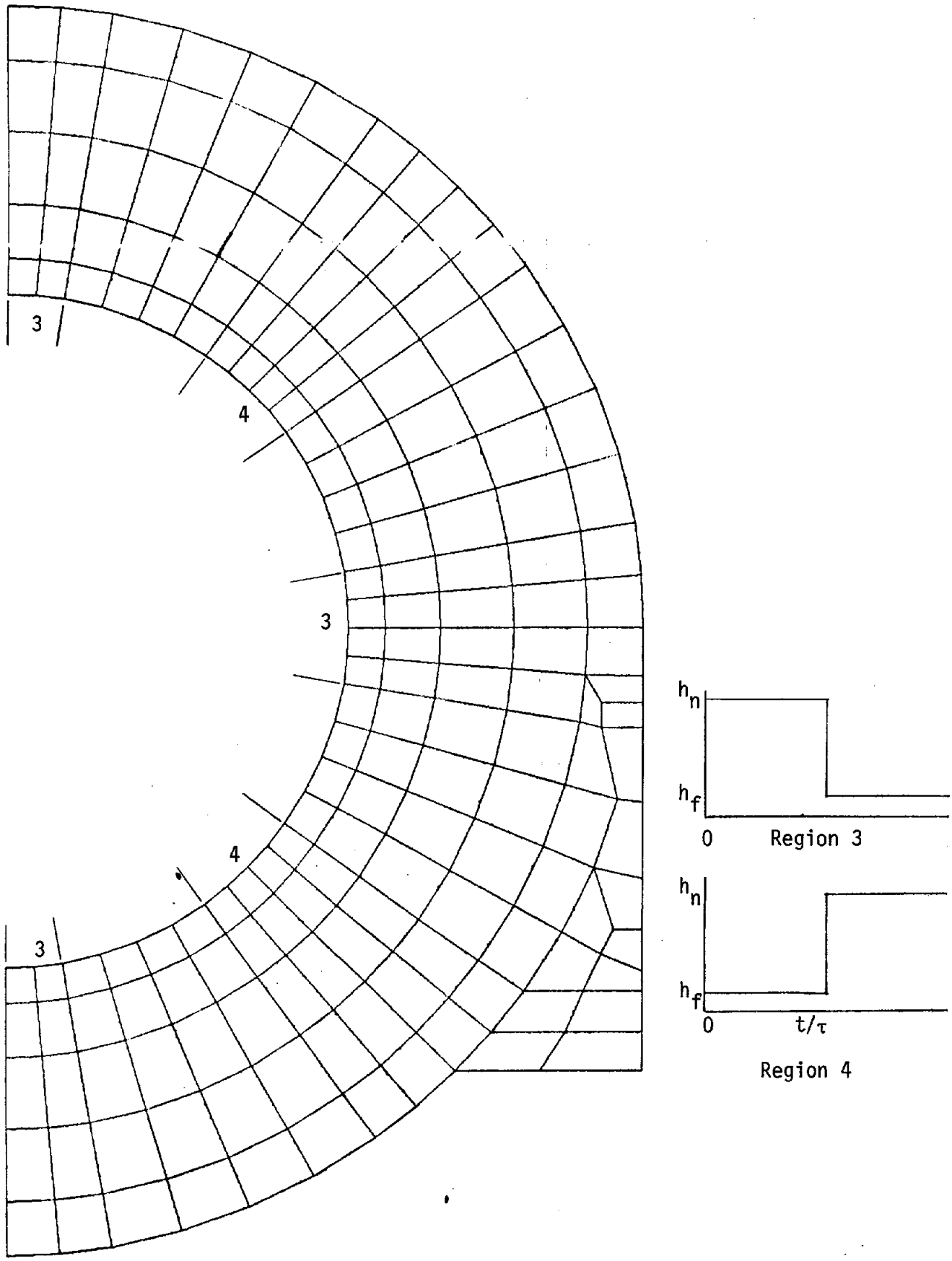

Figure 20. Finite Element Model B, 4 Rivulets, and Heat Transfer Coefficient Application

inhibits the warping of a tube cross section and may increase the stress at a local hot spot or a cold spot and, also, may increase the stress range at such locations between temperature extremes.

Since the tube geometry and the thermal loading are symmetrical about the mid-longitudinal plane of the tube, $\theta = 0$ and $\theta = 180°$, only half of the tube is considered for analysis. To simulate this symmetry, the cut boundary was not permitted to deform circumferentially nor allowed to possess a rate of change of radial deformation with respect to the θ coordinate. However, the tube was permitted to deform radially according to its thermal expansion.

3.3 THERMAL ANALYSIS

The analysis to evaluate temperature responses as a function of time was first performed for the receiver panel tubes with maximum heat flux for the pilot and commercial plants. Analyses were performed with Model A (2 rivulets) and Model B (4 rivulets) with 8-s and 3-s periods. The boundary conditions consisting of fluid pressure and temperature, heat transfer coefficients, and heat flux are summarized in Table 4, based on results from the overall thermal performance analysis presented in Section 2. A heat flux condition corresponding to 80% maximum heat flux for the commercial plant receiver was selected after the thermal-stress results showed that the fatigue life for the commercial plant with maximum heat flux is less than the required design life.

Temperature response of the outer and inner walls as a function of time at the location of maximum temperature oscillation are presented in Figures 21 and 22 for maximum heat flux conditions for the pilot and commercial plants, respectively. Conditions are analyzed with Model A with a period of 8 s and with Model B with periods of 8 and 3 seconds. Maximum temperature oscillations occur on the inner wall surface near the radial plane of maximum heat flux. As the transition wave changes from nucleate boiling to film boiling, the temperature increases on both the inner and outer walls. Conversely, with the change from film boiling to nucleate boiling the temperature decreases on both

Table 4. Boundary Conditions For Thermal Oscillation Analysis

	Pilot Plant	Commercial Plant	
	Maximum Heat Flux	Maximum Heat Flux	80% Maximum Heat Flux
Tube			
Material	Incoloy 800	Incoloy 800	Incoloy 800
D_i mm	6.83	6.83	6.83
D_o mm	12.70	12.70	12.70
CHF Condition			
P_i MPa (psia)	10.5 (1520)	13.0 (1880)	12.4 (1800)
T_H °C (°F)	314 (598)	331 (627)	327 (621)
h_n $kW/m^2C(Btu/h\cdot ft^2F)$	59.0 (10400)	133.5 (23530)	111.8 (19710)
h_f $kW/m^2C(Btu/h\cdot ft^2F)$	2.21 (390)	7.77 (1370)	6.58 (1160)
$q_i"$ MW/m^2	0.295	0.850	0.680
$q_a"$ MW/m^2	0.266	0.768	0.618
Model and Oscillation period, s	A-8 B-8,3	A-8 B-8,3	B-3

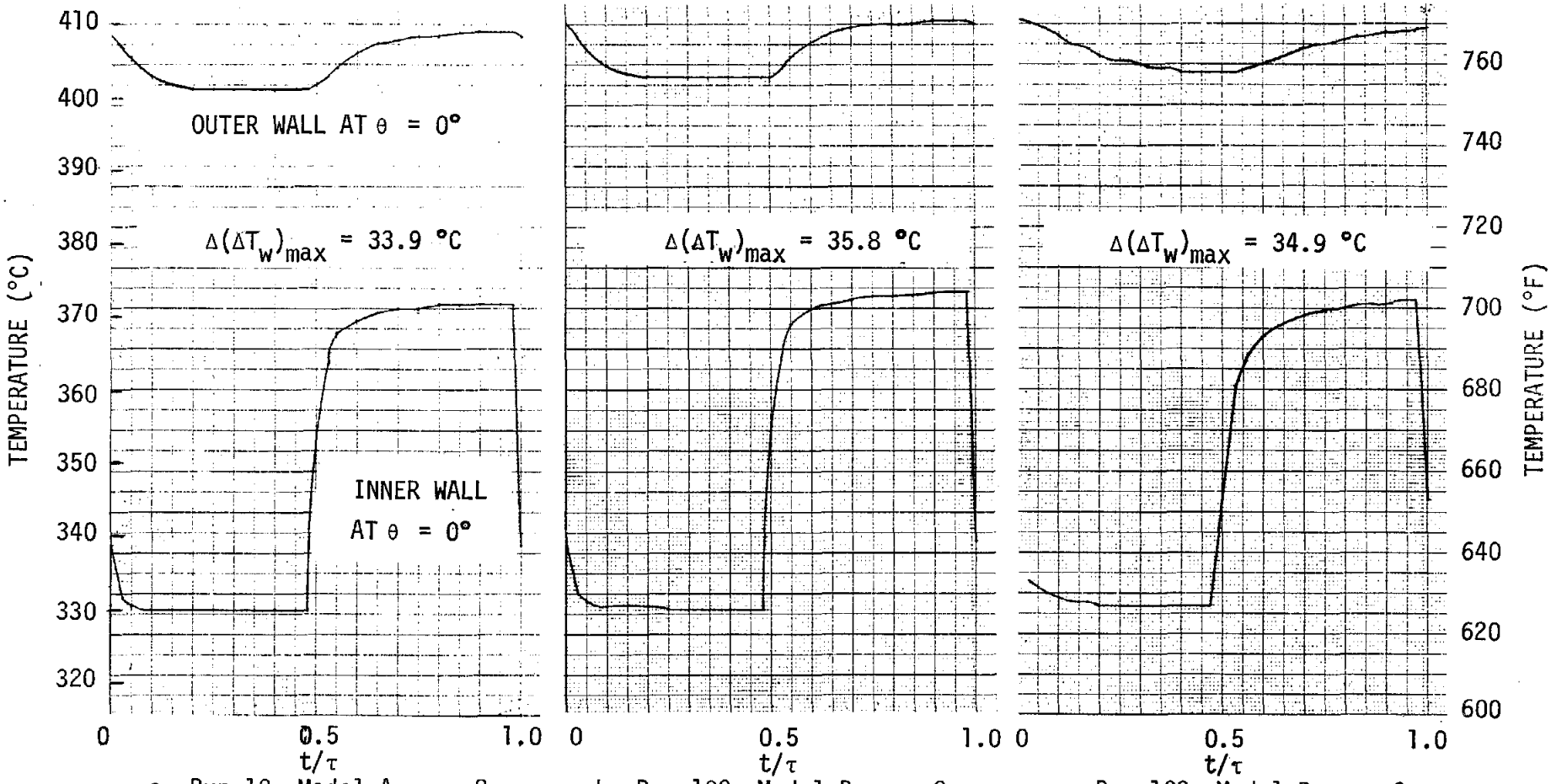

a. Run 12, Model A, τ = 8 s b. Run 102, Model B, τ = 8 s c. Run 103, Model B, τ = 3 s

Figure 21. Temperature Profiles at Maximum Temperature Oscillation for the Pilot Plant Receiver Tubes with Maximum Heat Flux

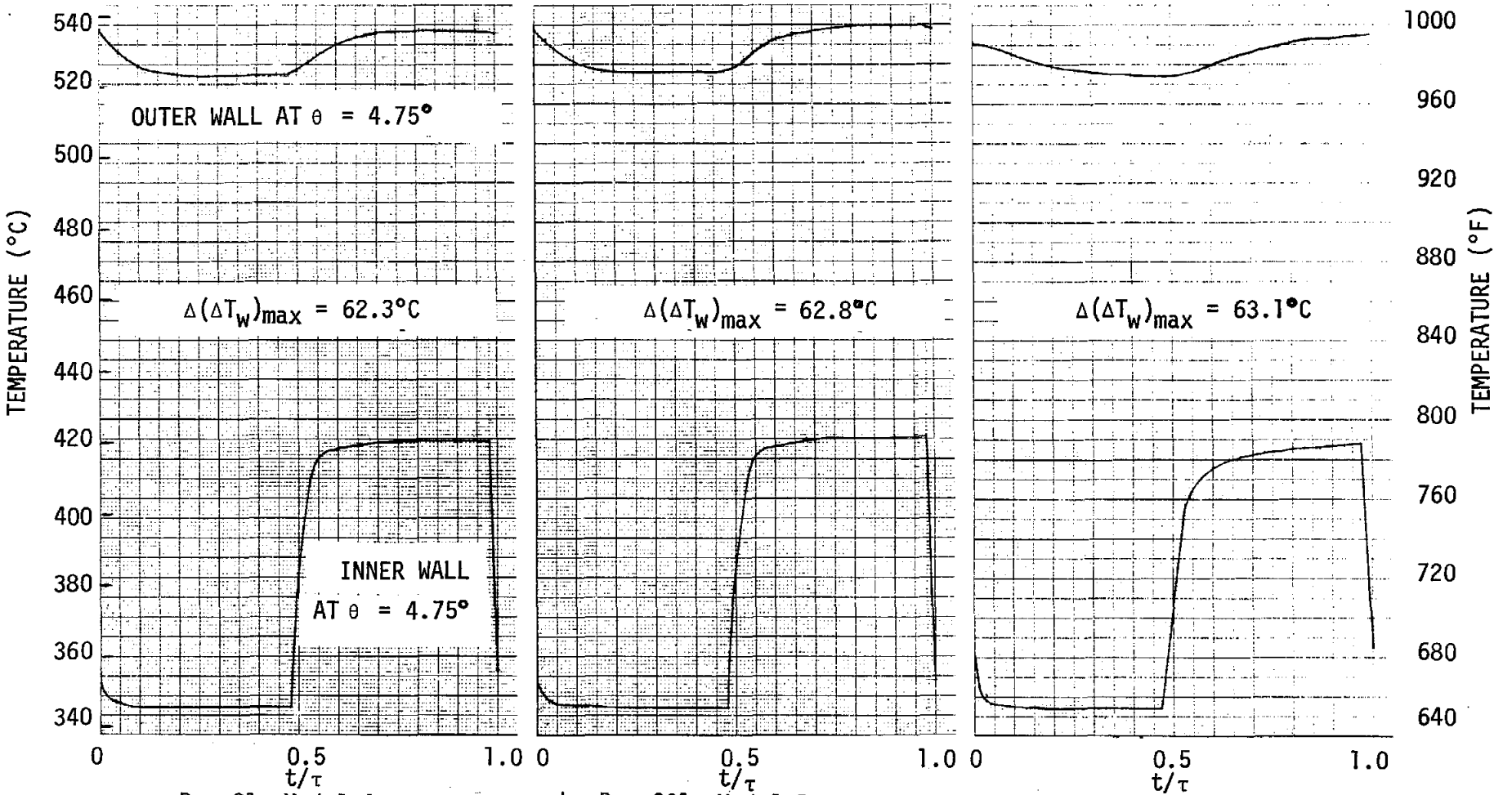

a. Run 21, Model A, τ = 8 s b. Run 201, Model B, τ = 8 s c. Run 202, Model B, τ = 3 s

Figure 22. Temperature Profiles at Maximum Temperature Oscillation for the Commercial Receiver Tubes with Maximum Heat Flux

walls. The rate of temperature change on the outer wall is about the same for both changes in the heat transfer coefficient. However, on the inner wall the temperature change corresponding to the transition from film boiling to nucleate boiling occurs much faster than for the inverse change from nucleate to film boiling. The faster temperature response for the former condition results from the much shorter time constant for nucleate boiling compared with film boiling. The heat transfer coefficients for nucleate boiling and film boiling, summarized in Table 4, have ratios of 27 for the pilot plant and 17 for the commercial plant.

Representative temperature contours for the maximum heat flux conditions are presented in Figures 23 through 25 for the pilot plant and in Figures 26 through 28 for the commercial plant. Parts a and b represent contours during the first and second half of the oscillation period, respectively. These contours illustrate the oscillating rivulets in the upper half of the tube for Model A, presented in Figures 23 and 26, and over both halves for Model B, presented in Figures 24 and 25 for the pilot plant and Figures 27 and 28 for the commercial plant. Temperature contours obtained every tenth of the oscillation period were used to obtain an indication of the radial and circumferential temperature gradients and, thus, guide the selection of candidate conditions with maximum and minimum gradients for subsequent stress analysis.

Quantitative results for maximum temperature oscillations are summarized in Table 5. The maximum temperature difference, $\Delta(\Delta T_w)_{max}$, between the maximum and minimum temperature difference across the tube wall is a parameter approximately proportional to an alternating stress amplitude. The results show only slightly more severe conditions obtained with Model B then Model A. Also the effects on temperature gradients resulting from a change in the oscillation period from 8 to 3 s is small. This latter effect is in agreement with previous results using a sinusoidally oscillating trapezoidal wave front model.[23] However, as the oscillation period is further decreased, or frequency increased, a drop in the temperature gradients leading to reduced alternating stress levels is expected.

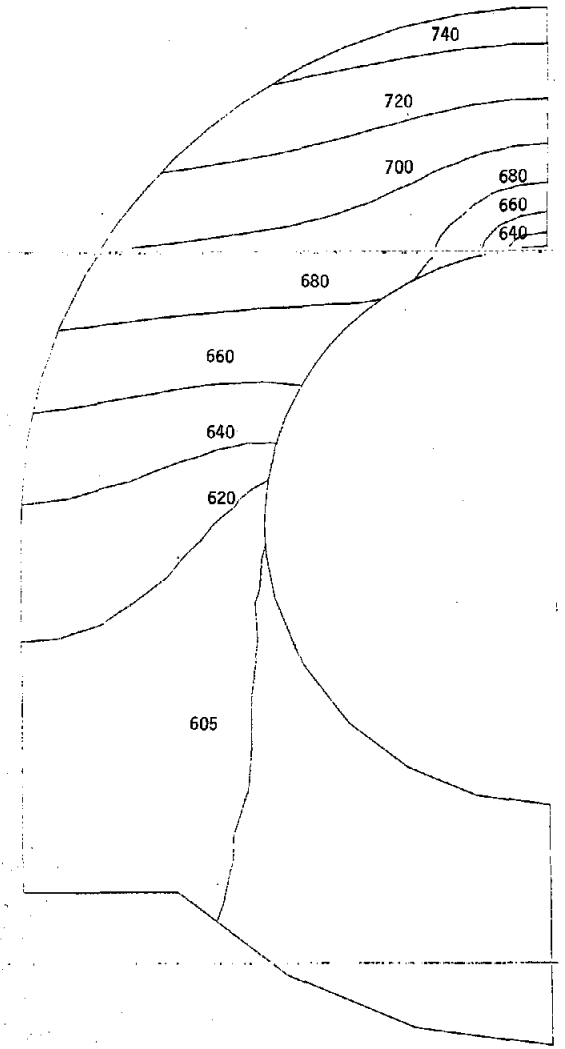

a. $t/\tau = 0.2$

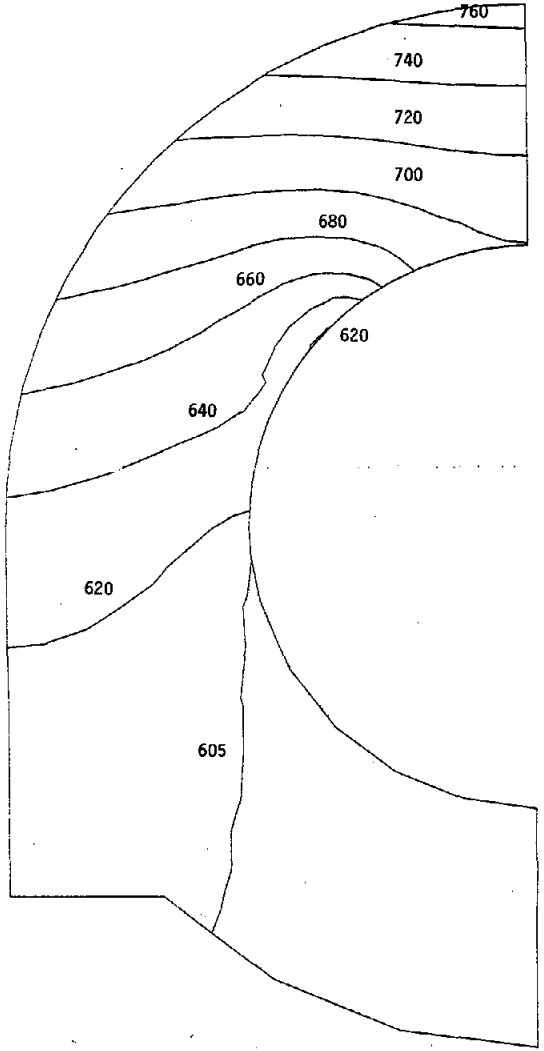

b. $t/\tau = 0.9$

Figure 23. Temperature Contours for the Pilot Plant Receiver Tube, Run 12, Model A, τ = 8 s. Units: (°F). Conversion (°C) = (°F - 32)/1.8

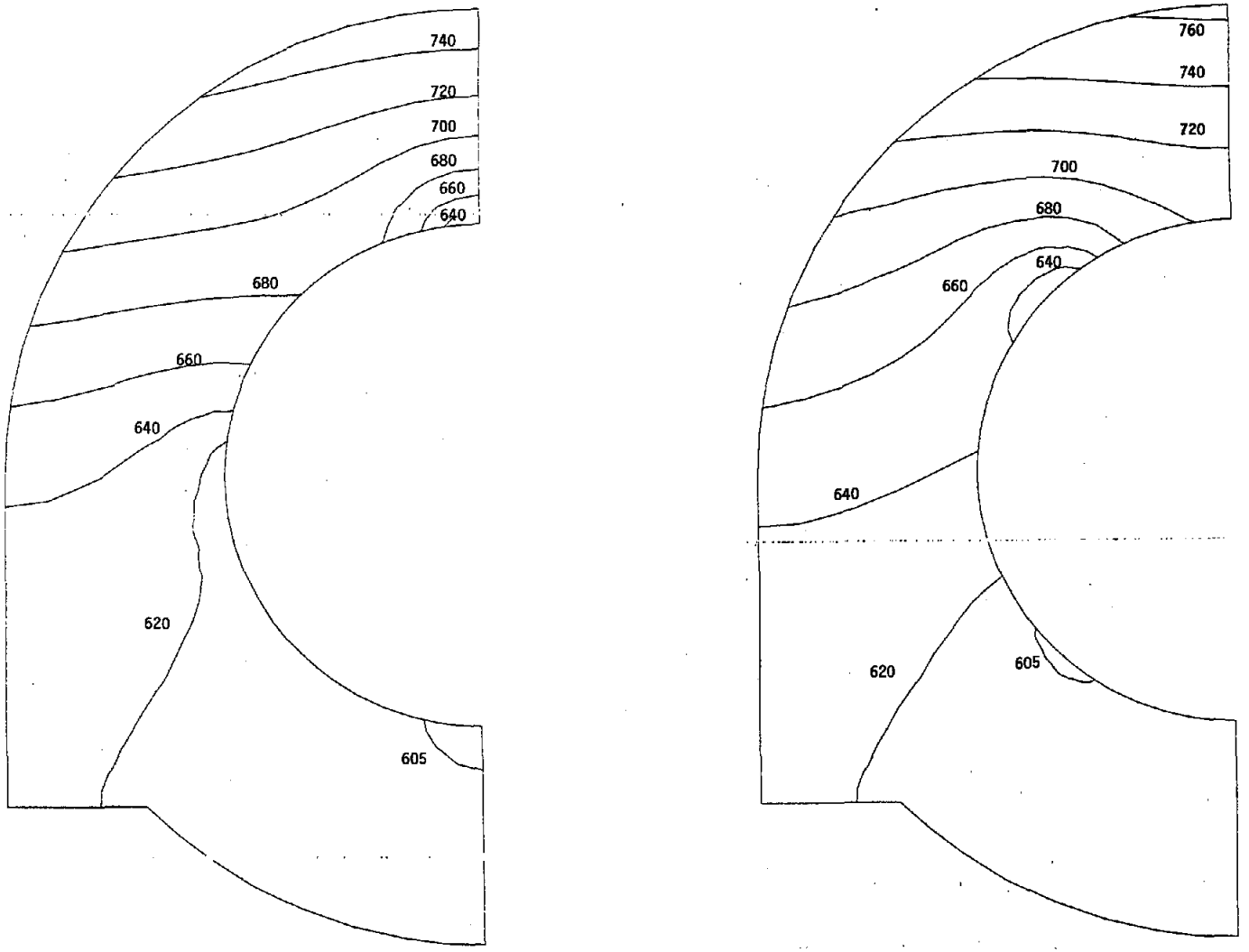

a. $t/\tau = 0.2$

b. $t/\tau = 0.9$

Figure 24. Temperature Contours of the Pilot Plant Receiver Tube, Run 102, Model B, τ = 8 s. Units: (°F). Conversion: (°C) = (°F - 32)/1.8

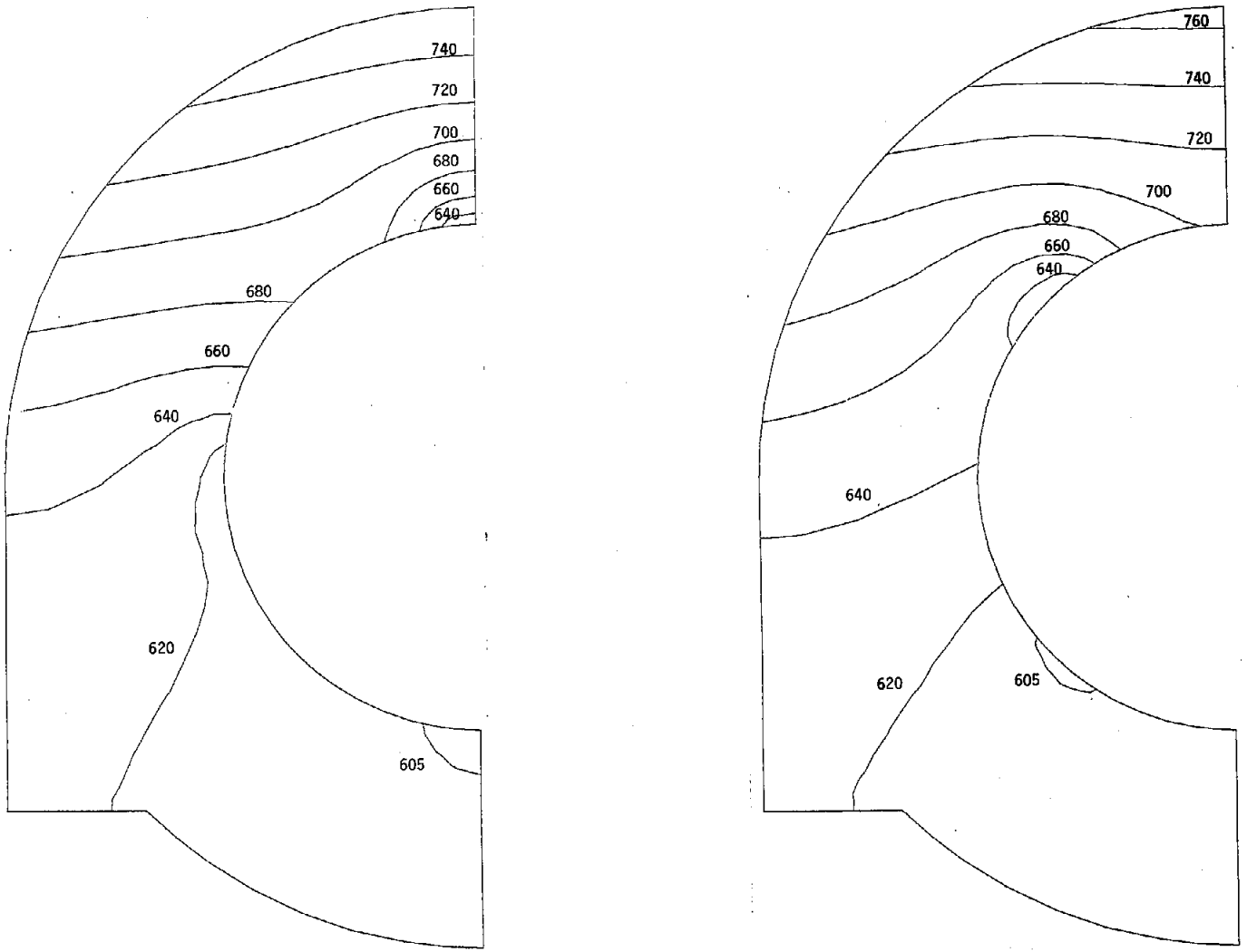

a. $t/\tau = 0.4$

b. $t/\tau = 0.9$

Figure 25. Temperature Contours for the Pilot Plant Receiver Tube, Run 103, Model B, τ = 3 s. Units: (°F). Conversion (°C) = (°F - 32)/1.8

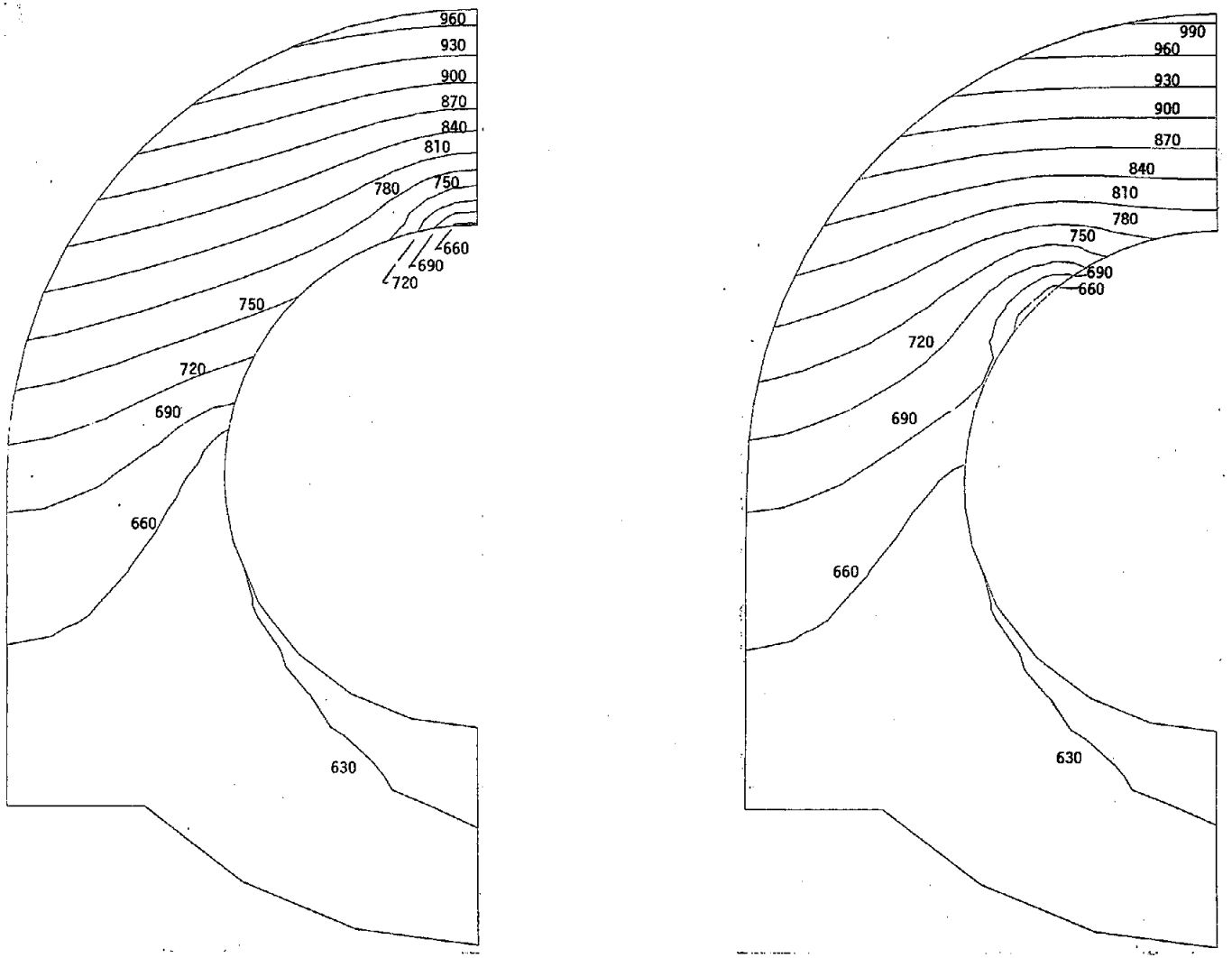

a. $t/\tau = 0.2$

b. $t/\tau = 0.9$

Figure 26. Temperature Contours for the Commercial Plant Receiver, Run 21, Model B, $\tau = 8$ s. Units: (°F). Conversion (°C) = (°F - 32)/1.8

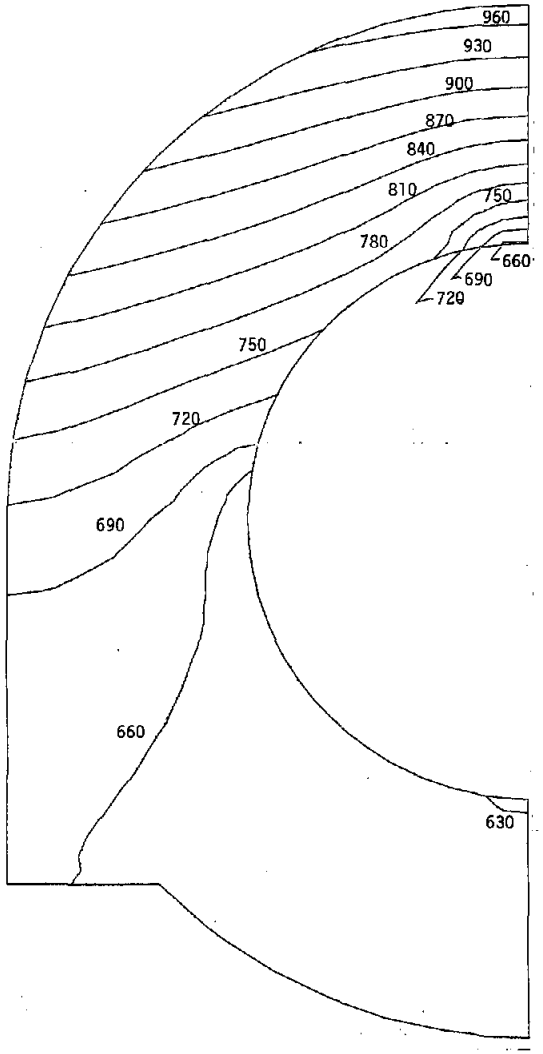

a. $t/\tau = 0.2$

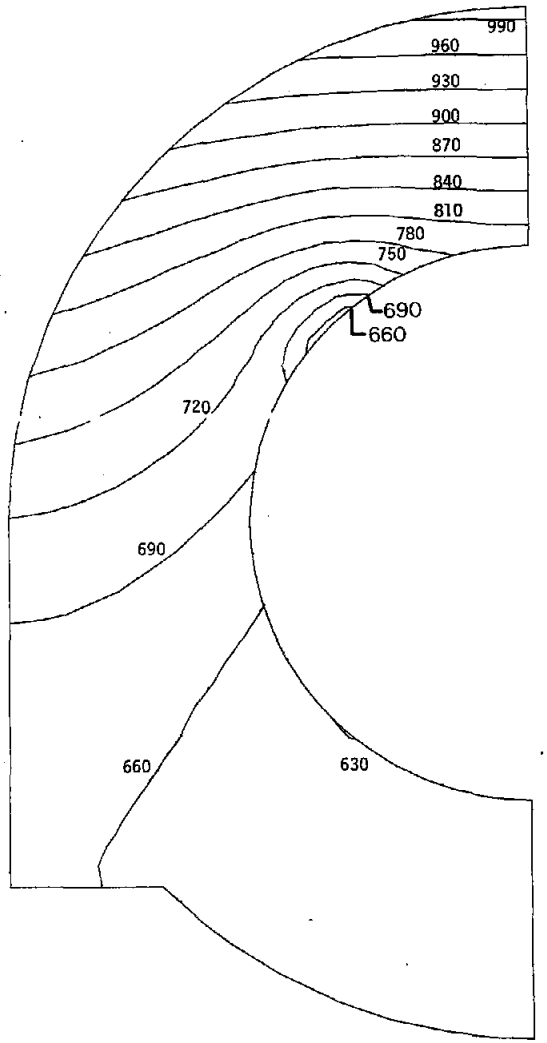

b. $t/\tau = 0.9$

Figure 27. Temperature Contours for the Commercial Receiver Tube, Run 201, Model B, τ = 8 s. Units: (°F). Conversion: (°C) = (°F - 32)/1.8

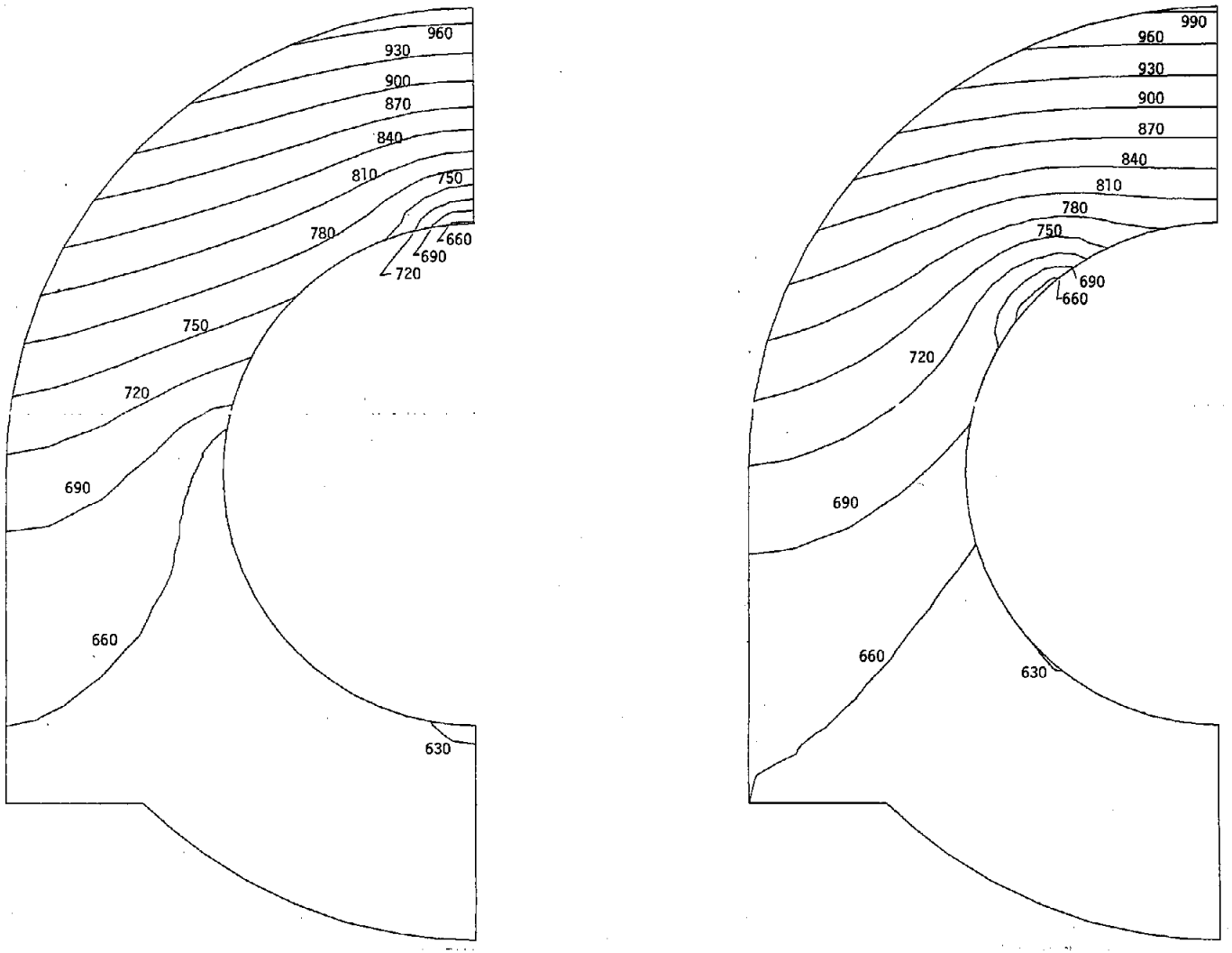

a. $t/\tau = 0.4$

b. $t/\tau = 0.9$

Figure 28. Temperature Contours for the Commercial Reciever Tube, Run 202, Model B, $\tau = 3$ s. Units: (°F). Conversion: (°C) = (°F - 32)/1.8

TABLE 5 - Thermal Oscillation Results

PLANT	HEAT FLUX	RUN NO.	MODEL	OSCILLATION PERIOD s	$\Delta T_{i,max}$ °C	$\Delta T_{w,max}$ °C	$\Delta(\Delta T_w)_{max}$ °C
Pilot	Maximum	12	A	8	41.9	71.2	33.9
		102	B	8	42.9	72.3	34.9
		103	B	3	41.7	72.8	35.8
Commercial	Maximum	21	A	8	75.2	177.9	62.3
		201	B	8	75.9	178.8	62.8
		202	B	3	74.3	178.1	63.1
	80% Maximum	301	B	3	64.7	147.2	54.1

3.4 STRESS ANALYSIS

3.4.1 Discussion of Method

The results of the thermal analysis with temperature distribution throughout the tube cross section were used as input to the stress analysis. A two-dimensional Cartesian coordinate system was used to define the stress components. The stress analysis was performed with a finite element generalized plane strain model by using the stress portion of the computer code TASA-01.[20] In the generalized plane strain analysis there are four stress components to be considered: the normal stress component σ_{22} which is perpendicular to the boundary forming the line of symmetry of the cross section, the normal stress component σ_{11} which is perpendicular to component σ_{22} in the cross-sectional plane, the shear stress σ_{12} which lies in the plane of these two normal stresses, and the axial stress σ_{33} which is along the axial direction of the steam tube and is perpendicular to the cross section. All the stress components obtained from the analysis are cyclic with respect to time. Maximum stresses at the inside wall surface occur in the region where the rivulet oscillates with maximum heat flux (θ = 0 in Figure 18) and at a time instance when the rivulet region is fully wet. The minimum stresses occur in the same region when it is fully dry and the rivulet is about to appear, i.e., at the end of the film boiling time period.

Several series of stress analyses were performed to predict the design life of the steam tubes. Analyses were performed for the receiver panel tubes for the pilot and commercial plants. The thermal boundary conditions and the thermal results which form the basis for the stress analysis are summarized in Tables 4 and 5, respectively.

Analysis results show that Model B (4-rivulet model) gives slightly higher stress than Model A (2-rivulet model). This is in agreement with the thermal results which also show the maximum $\Delta(\Delta T_w)$ to be slightly higher for Model B. Hence, only the Model B stress results are summarized in this report.

The stress computation model in the TASA-01 code can perform a plane strain analysis instead of a generalized plane strain analysis. In the plane strain analysis, all plane cross sections remain plane and axial (perpendicular to the cross section) movement is completely inhibited. Length of a tube between any two cross sections would remain constant even with temperature changes in the tube. This restraint obviously creates high compressive axial stress when the tube temperature is much higher than the reference (stress-free) temperature. A more realistic model is the generalized plane strain model in which plane cross sections remain plane but axial movements of the cross sections are allowed. To obtain stresses corresponding to the generalized plane strain model from the stresses of the plane model, the following method is used:

$$\sigma_{ij}^{G} = \sigma_{ij}^{P} - \sigma_{ij}^{I} \tag{18}$$

Here, σ_{ij} is any one of the four stress components, superscript G indicates generalized plane strain model, superscript P indicates plane model, and superscript I indicates an isothermal case. The stresses of the isothermal case are obtained by taking the average temperature over the tube cross section at the instance of the cycle when the stresses are calculated as input and performing a plane strain analysis. After the operation of the right hand side of Equation (18), the stresses due to the restrained axial movement are relieved and the resulting stresses are those that would be obtained from a generalized plane strain computation. Note that even though the restriction of the plane strain model is in the axial direction, stresses in other directions may be affected due to the effect of the Poisson's ratio and other geometrical boundary conditions.

Fatigue damage to the steam tube is caused by oscillation of strain (which can be related to stress oscillation) during a temperature oscillation cycle. To calculate this stress oscillation, the maximum and the minimum stresses during a cycle must be known. The concept of stress intensity (the maximum difference

of any two principal stresses) was used to reduce a three-dimensional stress state into a one-dimensional stress for the purpose of calculating this stress oscillation.

Design fatigue curves of Incoloy 800H are shown in Figure 29 from the ASME code Section III, Subsection NA[28] and in Figure 30 from ASME Code Case 1592.[27] The latter is for application at temperatures above 427°C (800°F). Since, at the location of the highest stress oscillation (inside tube wall surface near $\theta = 0$, Figure 18), the temperature is never higher than 427°C (800°F) (see Figures 21 and 22), the former curve will be applied in the current analysis.

3.4.2 Stress and Fatigue Results

The commercial plant temperature oscillations in the transition boiling region were analyzed with 8-s and 3-s periods. Figures 31 and 32 shown the stresses for an 8-s period at the instances of maximum and minimum stress intensity, respectively. The location is near the line of tube symmetry at $\theta = 0$ with maximum heat flux and rivulet oscillation. It is seen that the shear component σ_{12} is small due to symmetry.

The principal stresses can be calculated from the stress components as follows:

$$S_1 = \frac{\sigma_{11} + \sigma_{22}}{2} + \sqrt{\left(\frac{\sigma_{11} - \sigma_{22}}{2}\right)^2 + \sigma_{12}^2} \qquad (19)$$

$$S_2 = \frac{\sigma_{11} + \sigma_{22}}{2} - \sqrt{\left(\frac{\sigma_{11} - \sigma_{22}}{2}\right)^2 + \sigma_{12}^2} \qquad (20)$$

Note that the axial stress, σ_{33}, is a principal stress, S_3.

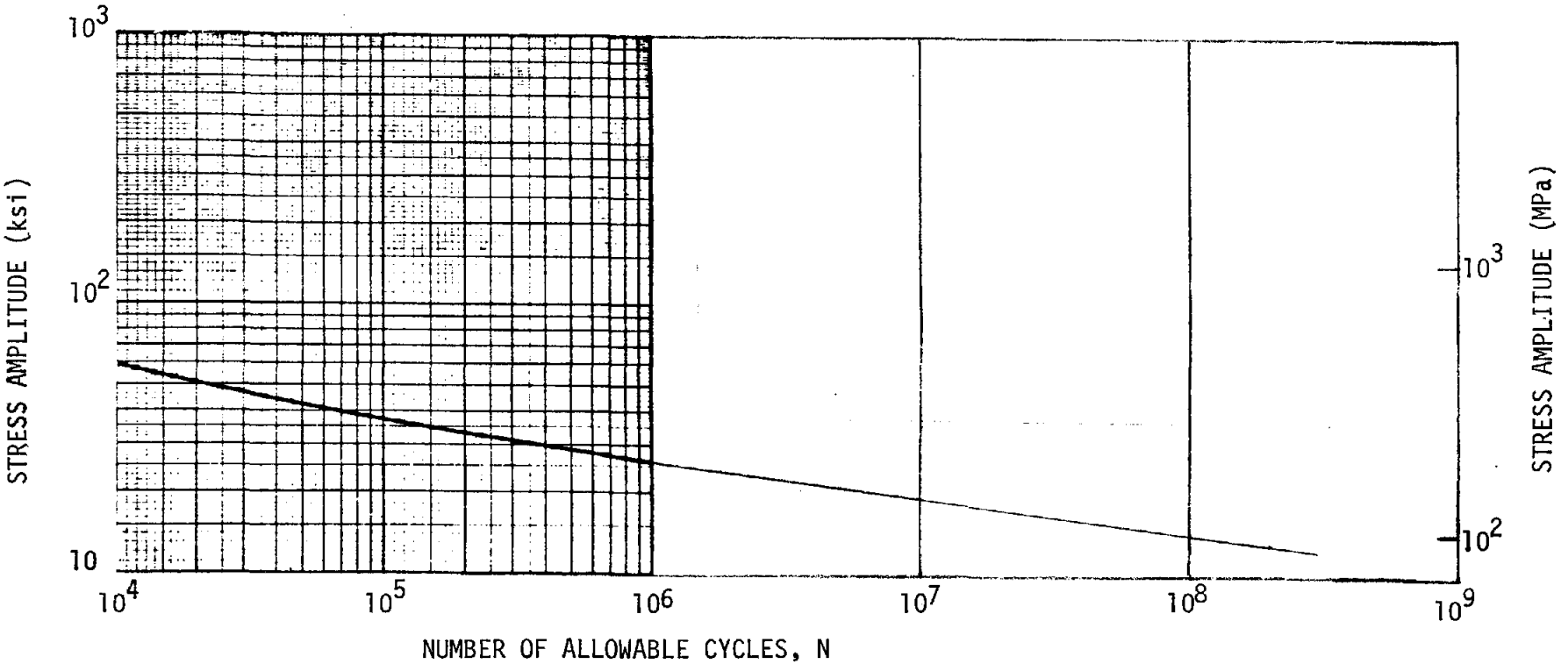

Figure 29. Design Fatigue Curve for Inoloy 800H for Temperatures Below 427°C (800°F), Ref. 28

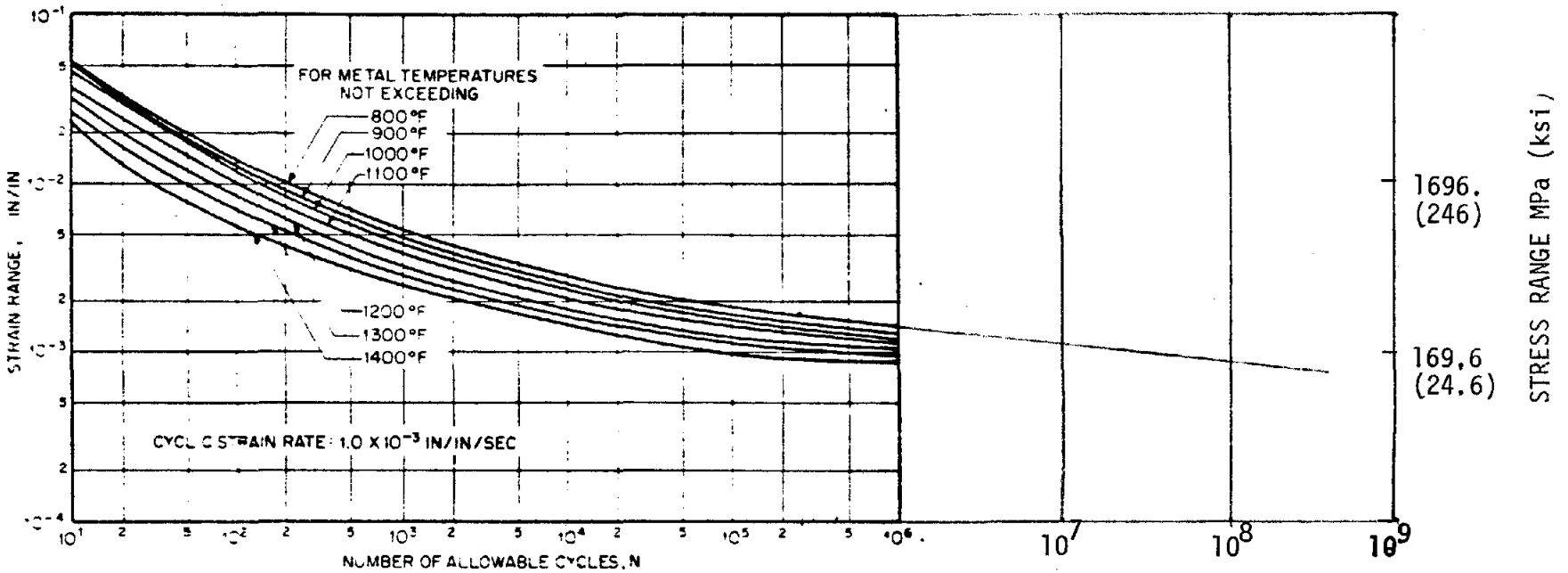

Figure 30. Design Fatigue Curve for Incoloy 800H for Temperatures Above 427°C (800°F), Ref. 27

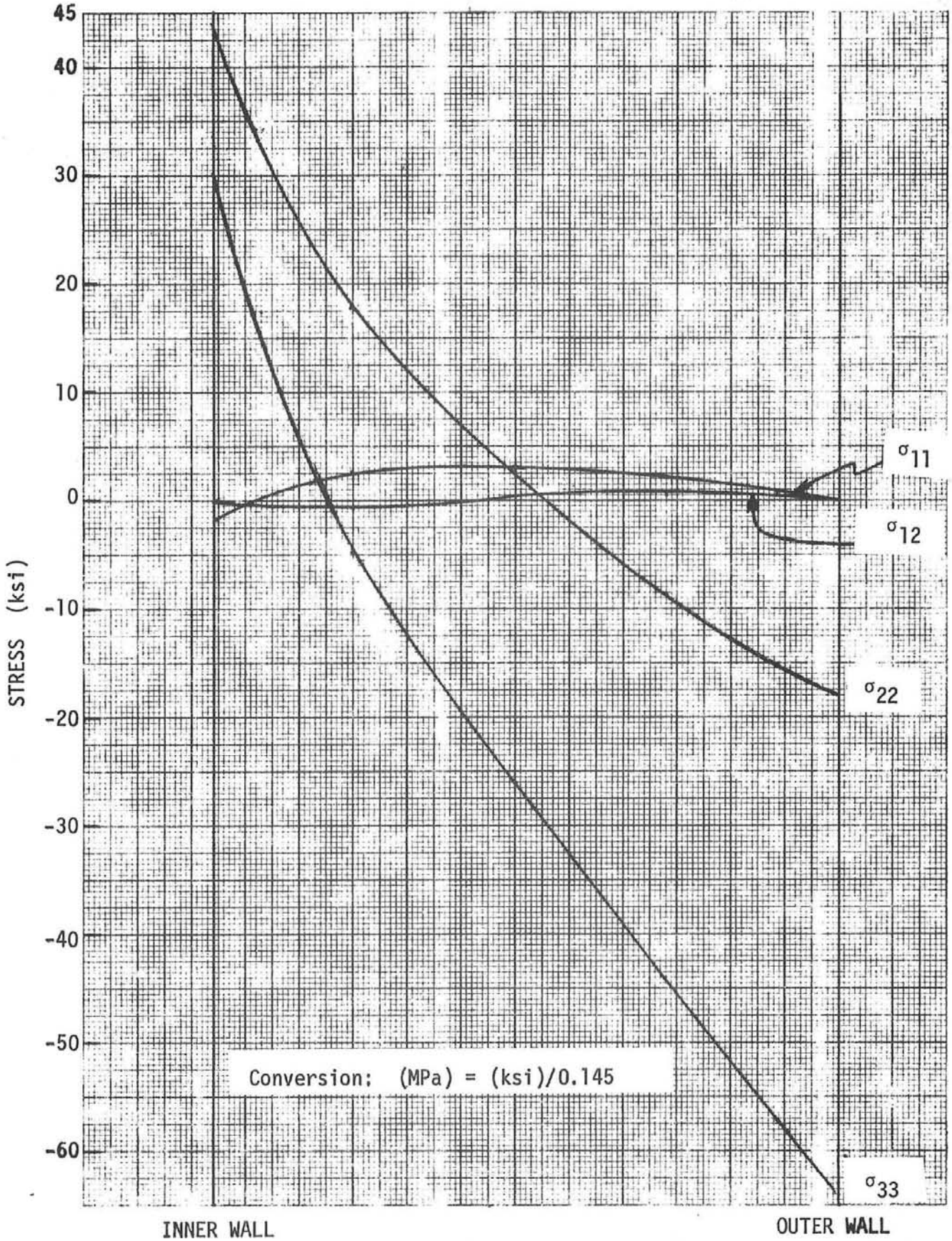

Figure 31. Stress Components at Maximum ΔT_W for the Commercial Plant with Model B at 8-s Period and with Pressure Load

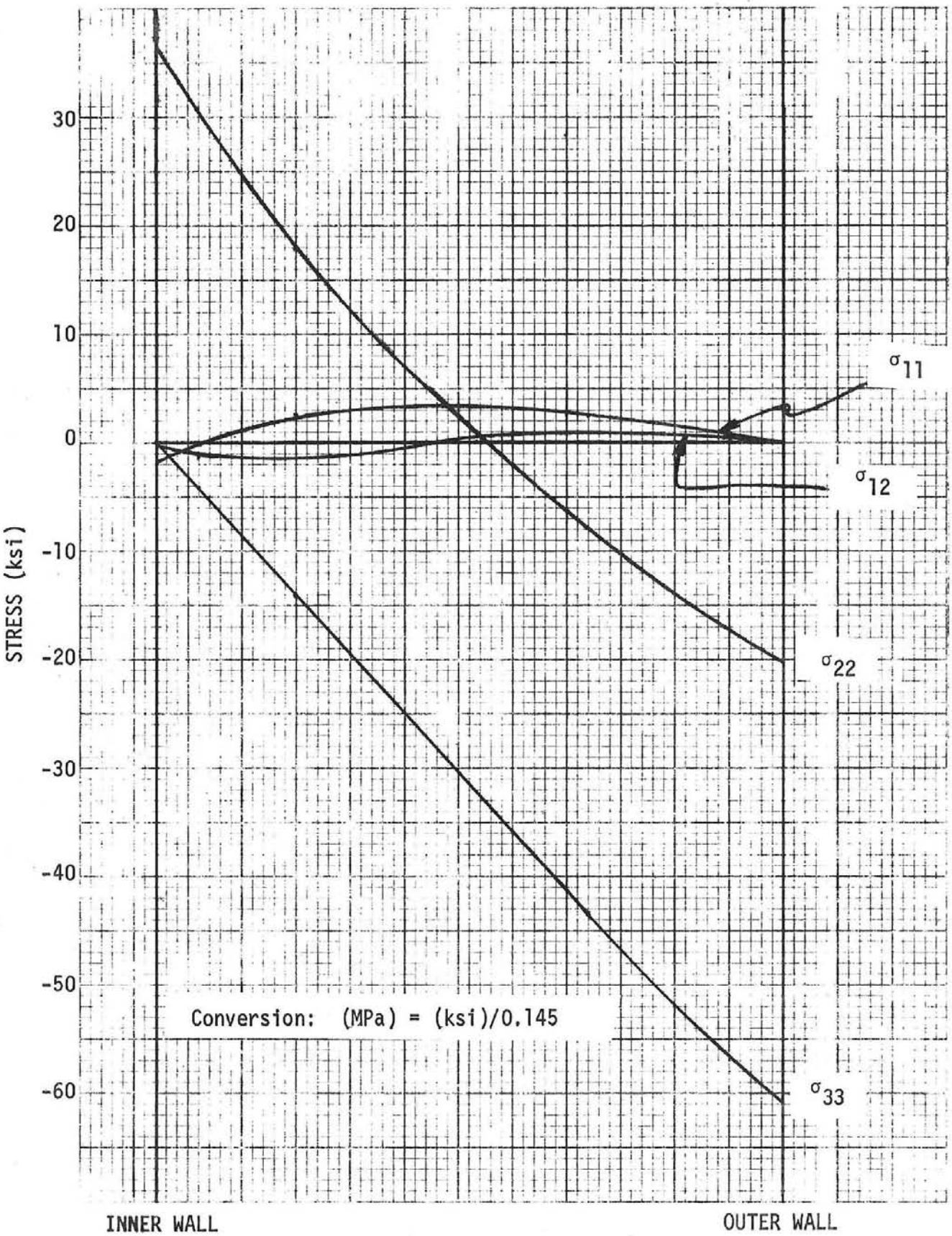

Figure 32. Stress Components at Minimum ΔT_w for the Commercial Plant with Model B at 8-s Period and with Pressure Load

In accordance with the maximum shear stress theory as a failure criterion, the alternating stress amplitude, S_{alt}, and the mean stress, S_m, can be calculated from the principal stresses based on the procedures provided in the ASME Boiler and Pressure Vessel Code, Section III, Subsection NA. Since the design fatigue curves are based on experimental tests involving a complete stress reversal, i.e., zero mean stress, an equivalent alternating stress amplitude, S_{eq}, with adjusted zero mean has to be calculated. The calculation is based on the procedure (modified Goodman's Diagram) established in ASME Boiler and Pressure Vessel Code for Design by Analysis in Section III and VIII, Division 2. The ultimate tensile strength of 455 MPa (66 ksi) for Incoloy 800H is used. The calculated results of S_{alt}, S_m and S_{eq} are tabulated in Table 6.

It is of interest to note that the steam pressure, being constant, will not contribute to the alternating stress, S_{alt}, but will contribute to the mean stress, S_m. However, from Table 6, it is noted that the quantity $S_m + S_{alt}$ for all cases for the commercial plant is greater than the yield stress of 116 MPa at 427°C (16.8 ksi at 800°F). Under these circumstances, the correction by Goodman's method is done with a modified mean stress equal to $\sigma_y - S_{alt}/2$, where σ_y is the yield stress. This correction is thus independent of the calculated mean stress. For this reason, the stress components (such as shown in Figures 31 and 32) are better exhibited with respect to the temperature variation alone to enhance the fact that the stress oscillation is induced by temperature variation only. These stress components for the commercial plant with an 8-s period are shown in Figures 33 and 34 for the instances of maximum stress and minimum stress, respectively.

The commercial plant with a 3-s oscillation period was analyzed with the same method. The stress components are shown in Figures 35 and 36 and the results are also summarized in Table 6. The equivalent stress amplitude is very close to that obtained for the 8-s period.

TABLE 6 - Stress Results for the Thermal-Stress Cycling Analysis

CONDITIONS						
Plant	Heat Flux	Model	Oscillation Period s	Alternating Stress Amplitude w/ Mean Stress S_{alt}, MPa, (KSI)	Mean Stress S_m, MPa, (KSI)	Equivalent Alternating Stress Amplitude with Adjusted Zero Mean S_{eq}, MPa, (KSI)
Commercial	Maximum	B	8	100.87 (14.63)	95.98 (13.92)	105.49 (15.30)
Commercial	Maximum	B	3	104.25 (15.12)	99.70 (14.46)	108.18 (15.69)
Commercial	80% of Maximum	B	3	84.60 (12.27)	70.74 (10.26)	91.91 (13.33)
Pilot	Maximum	B	8	44.68 (6.48)	1.03 (0.15)	44.88 (6.51)

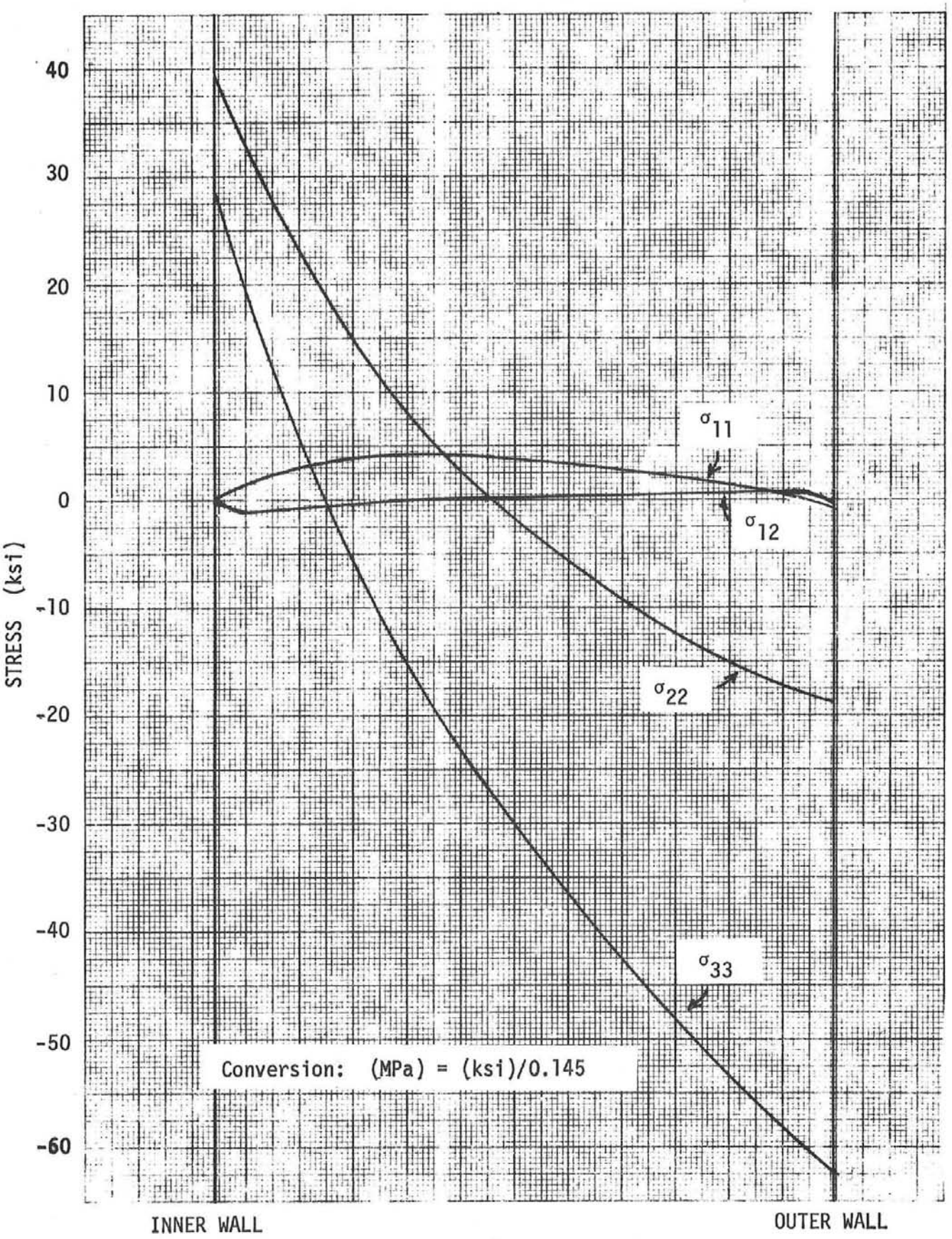

Figure 33. Stress Components at Maximum ΔT_w for the Commercial Plant with Model B at 8-s Period and Without Pressure Load

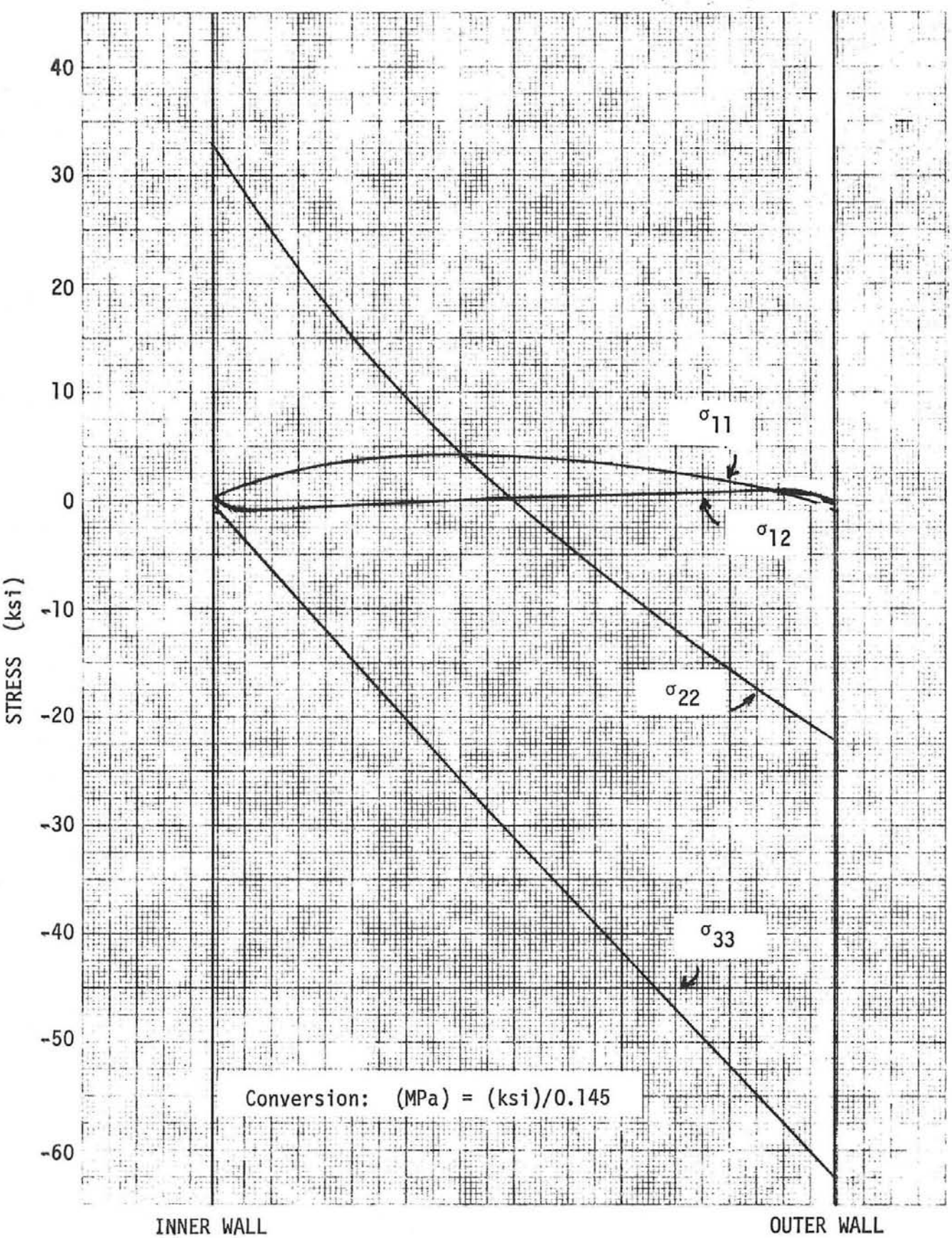

Figure 34. Stress Components at Minimum ΔT_w for the Commercial Plant with Model B at 8-s Period and Without Pressure Load

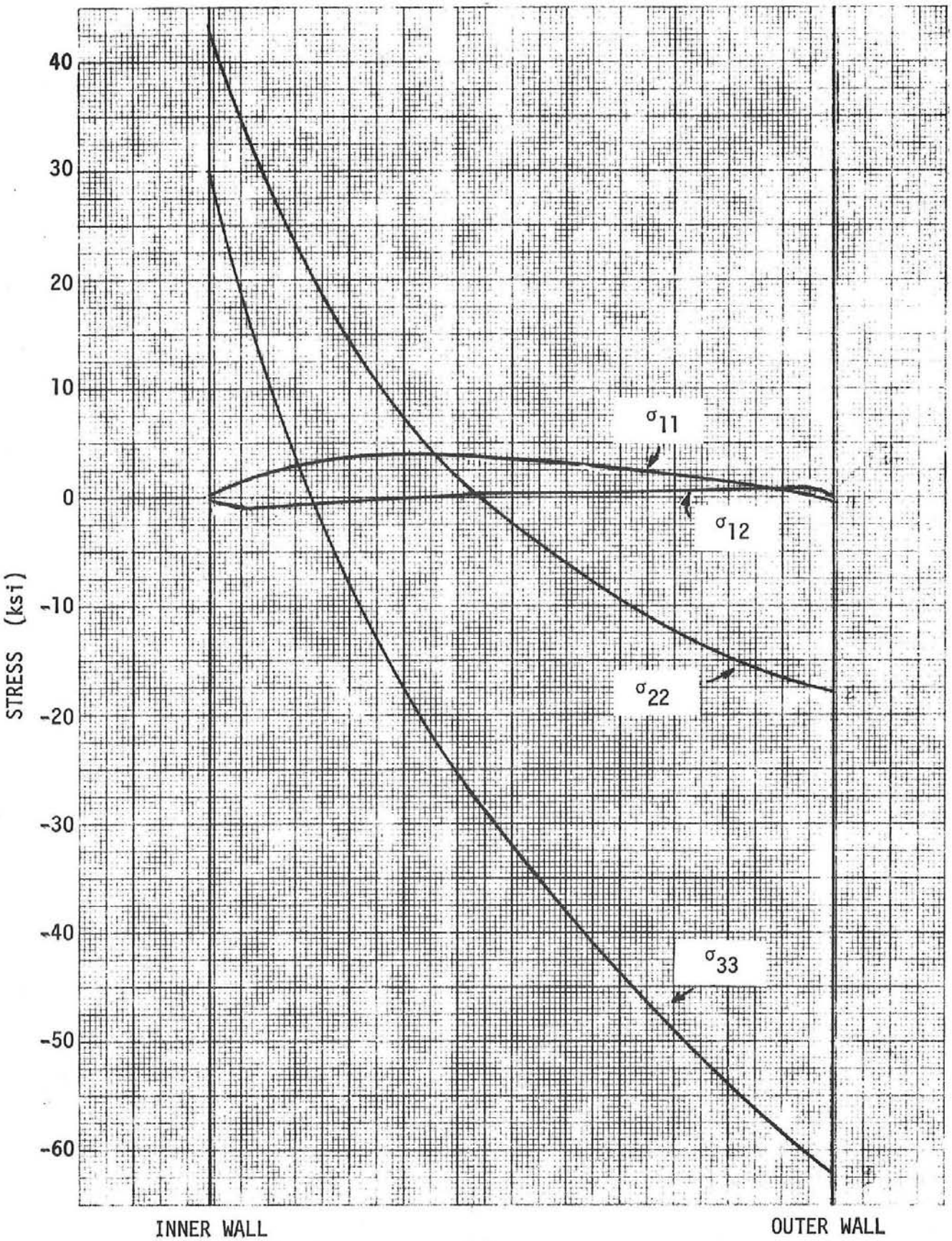

Figure 35. Stress Components at Maximum ΔT_W for the Commercial Plant with Model B at 3-s Period and Without Pressure Load

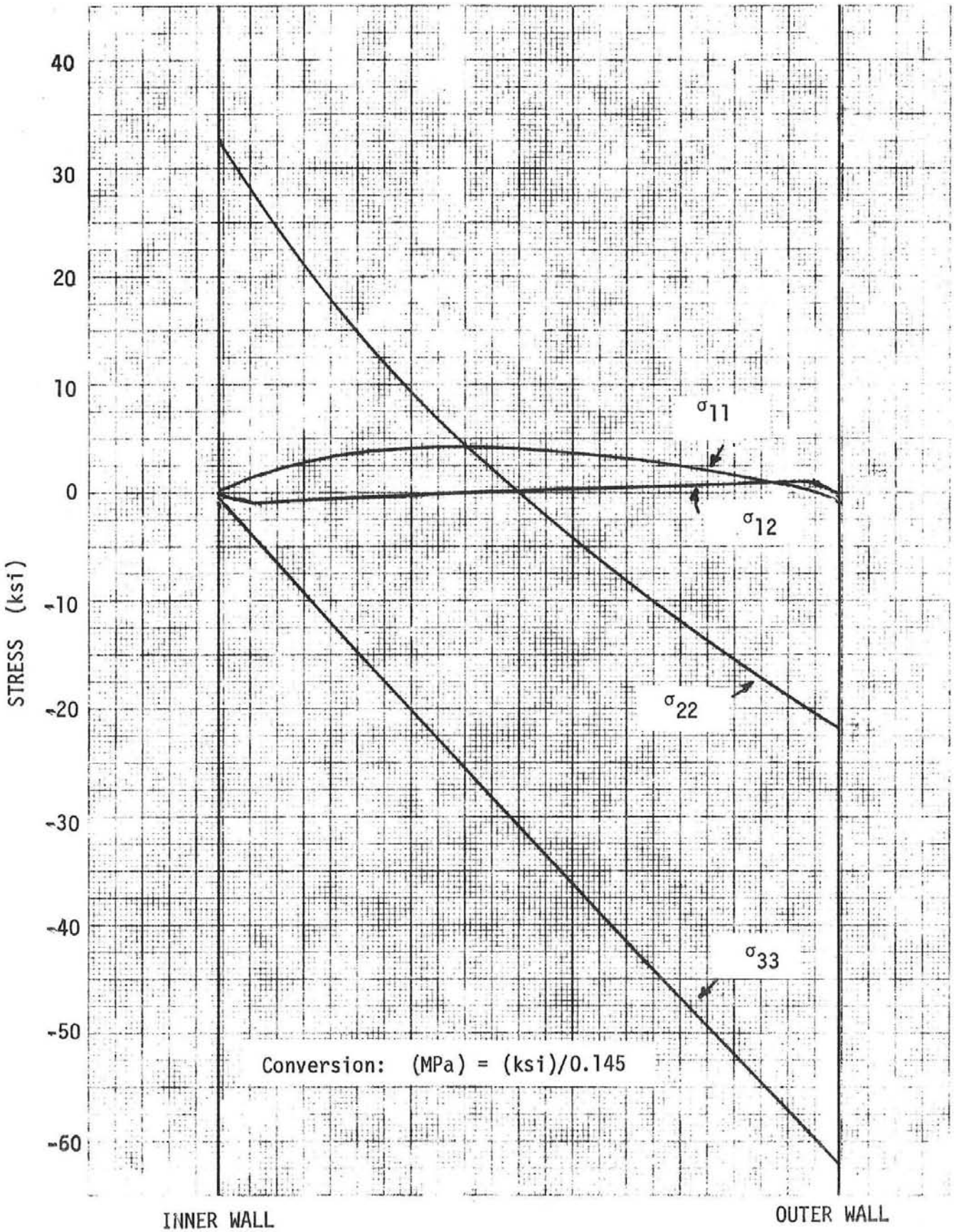

Figure 36. Stress Components at Minimum ΔT_w for the Commercial Plant with Model B at 3-s Period and Without Pressure Load

The equivalent stress amplitudes of both the 8-s and the 3-s cases are used in Figure 29 to find the allowable design fatigue cycles of 7×10^7 cycles and 6×10^7 cycles, respectively. These are converted into 47 years and 15 years, respectively, based on an operating schedule of 10 hours per day and 330 days per year. Table 7 summarizes these results, based on ASME Code Section III, Subsection NA. Similar results based on the ASME Code Case 1592 fatigue curve are also presented in Table 7 for comparison purposes. As discussed in Subsection 3.4.1, the results based on the Section III, Subsection NA fatigue curve apply for the current situation.

A case with reduced heat flux for the commercial plant receiver tubes was selected for analysis to achieve at least a 30-year design life with a 3-s period. Figure 29 shows that a stress reduction of 12% from the previous 3-s case is required to obtain this longer life. It was estimated that a 20% reduction in heat flux was needed to assure a 12% stress reduction. When this was done, the stress was actually reduced by 15% and a tube life of 51 years was obtained, as shown in the summary of Table 7. The corresponding stress components are shown in Figures 37 and 38.

Similar stress analysis was applied to the conditions of the pilot plant with an 8-s oscillation period. The stress components at the maximum and minimum ΔT_w are shown in Figures 39 and 40, respectively. The corresponding equivalent stress amplitude is only 44.88 MPa (6.51 ksi). This stress amplitude is much lower than the "endurance limit" of the fatigue curves and indicates a fatigue life much longer than 30 years. Based on the results of the studies on the commercial plant with 8-s and 3-s oscillation periods under similar heat transfer conditions, it was concluded that the stress magnitudes for the pilot plant with a 3-s period would be very close to those of an 8-s period and the corresponding fatigue life would also be much longer than 30 years. The stress and fatigue life results are summarized in Tables 6 and 7.

TABLE 7 - Fatigue Life of Receiver Tubes with CHF Temperature Oscillations

Plant	Heat Flux	Model	Oscillation Period s	ASME B&PV CODE SECTION III SUBSECTION NA		ASME B&PV CODE CASE 1592	
				Cycles	Years	Cycles	Years
Commercial	Maximum	B	8	7×10^7	47	5×10^6	3.4
Commercial	Maximum	B	3	6×10^7	15	4.5×10^6	1.1
Commercial	80% of Maximum	B	3	2×10^8	51	2×10^7	5
Pilot	Maximum	B	3&8		>>30		>>30

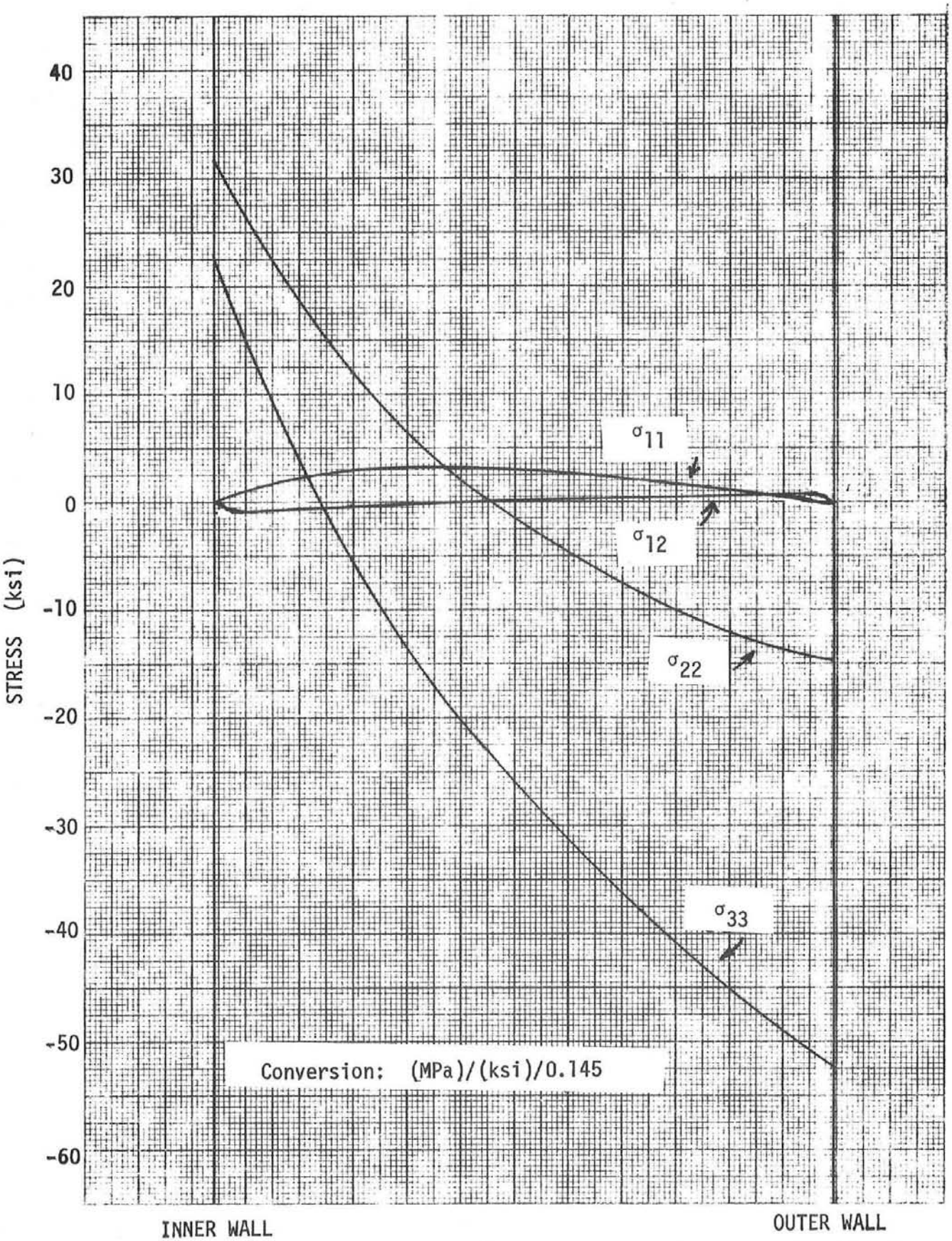

Figure 37. Stress Components at Maximum ΔT_w for the Commercial Plant with Model B at 3-s Period with Reduced Heat Flux and Without Pressure Load

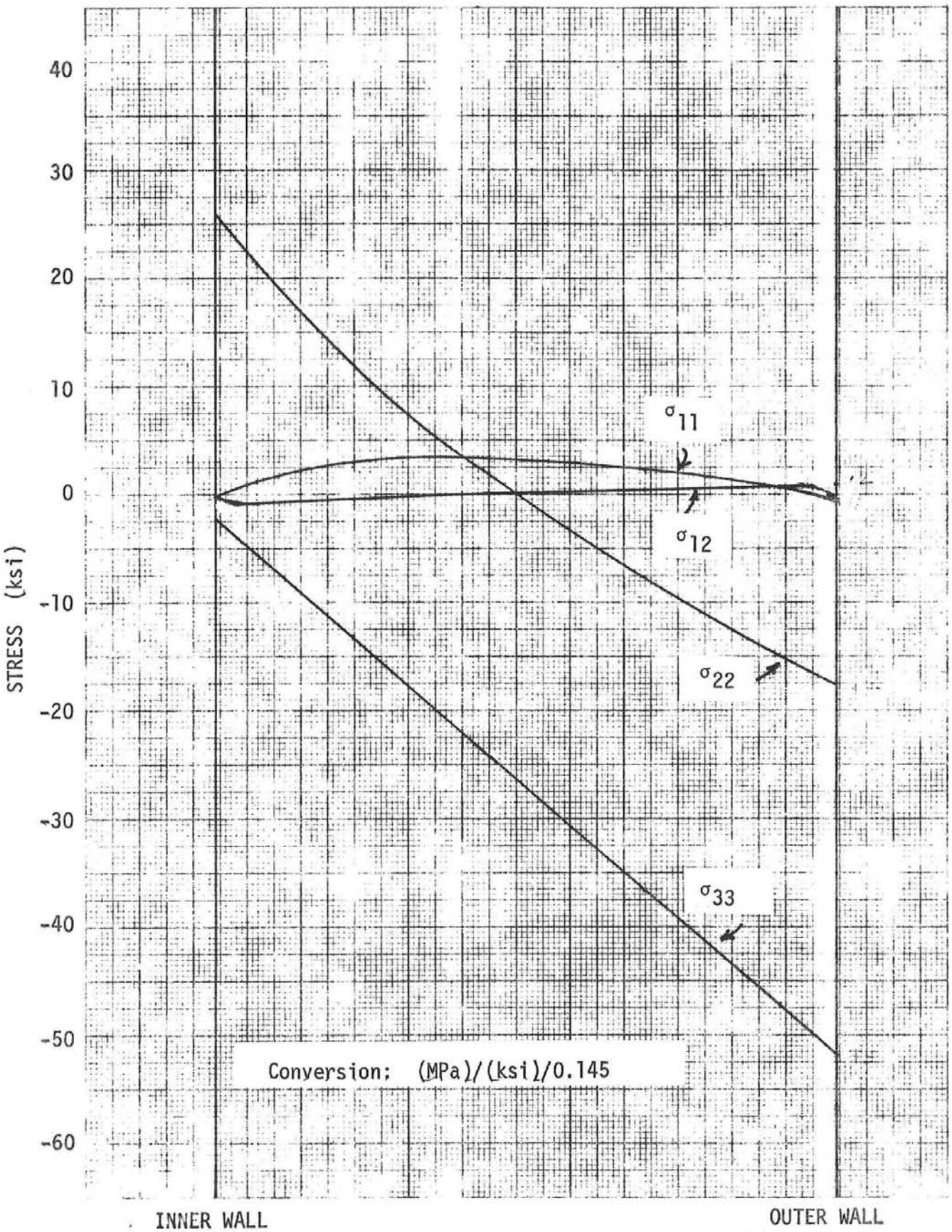

Figure 38. Stress Components at Minimum ΔT_w for the Commercial Plant with Model B at 3-s Period with Reduced Heat Flux and Without Pressure Load

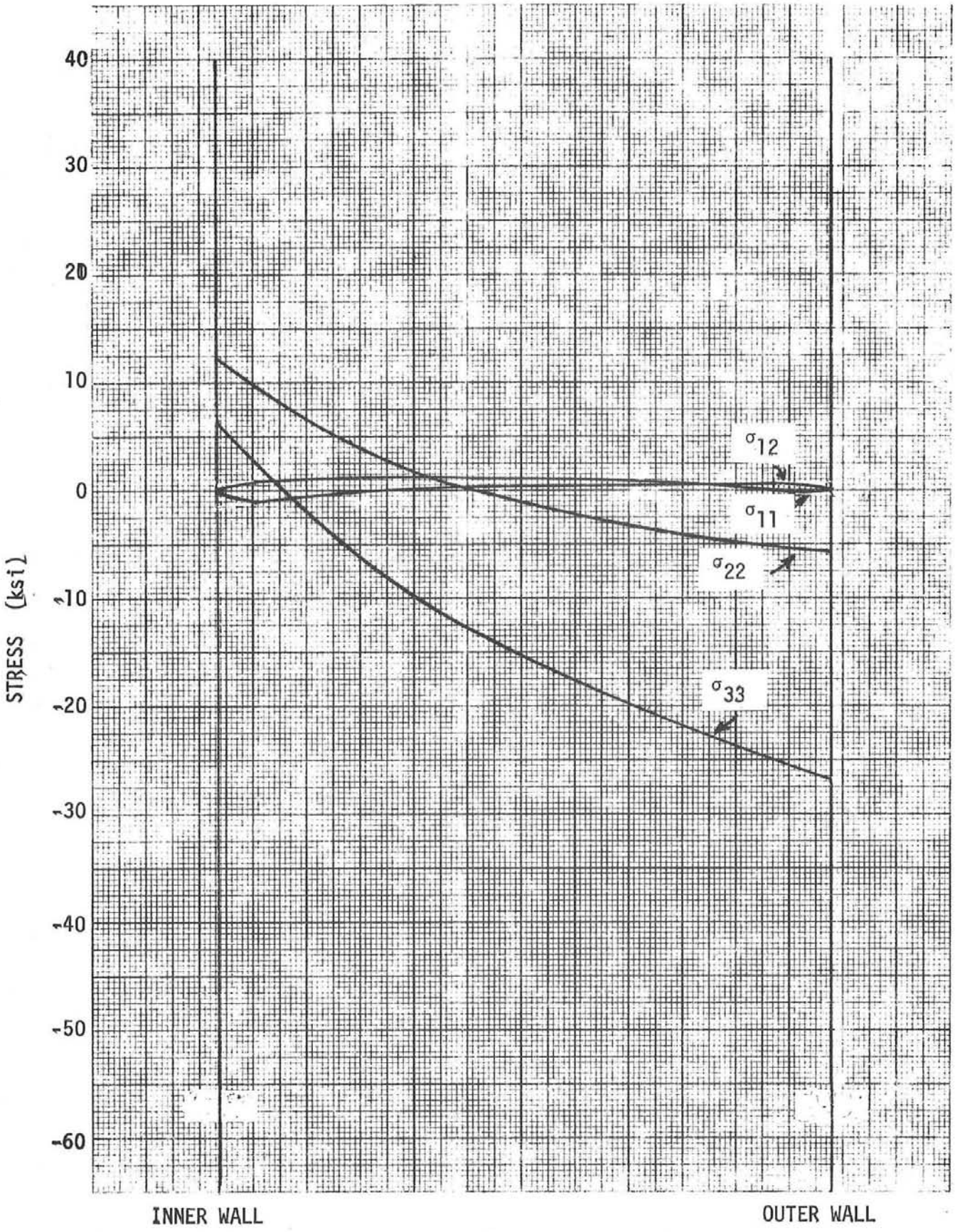

Figure 39. Stress Components at Maximum ΔT_w for the Pilot Plant with Model B at 8-s Period and Without Pressure Load

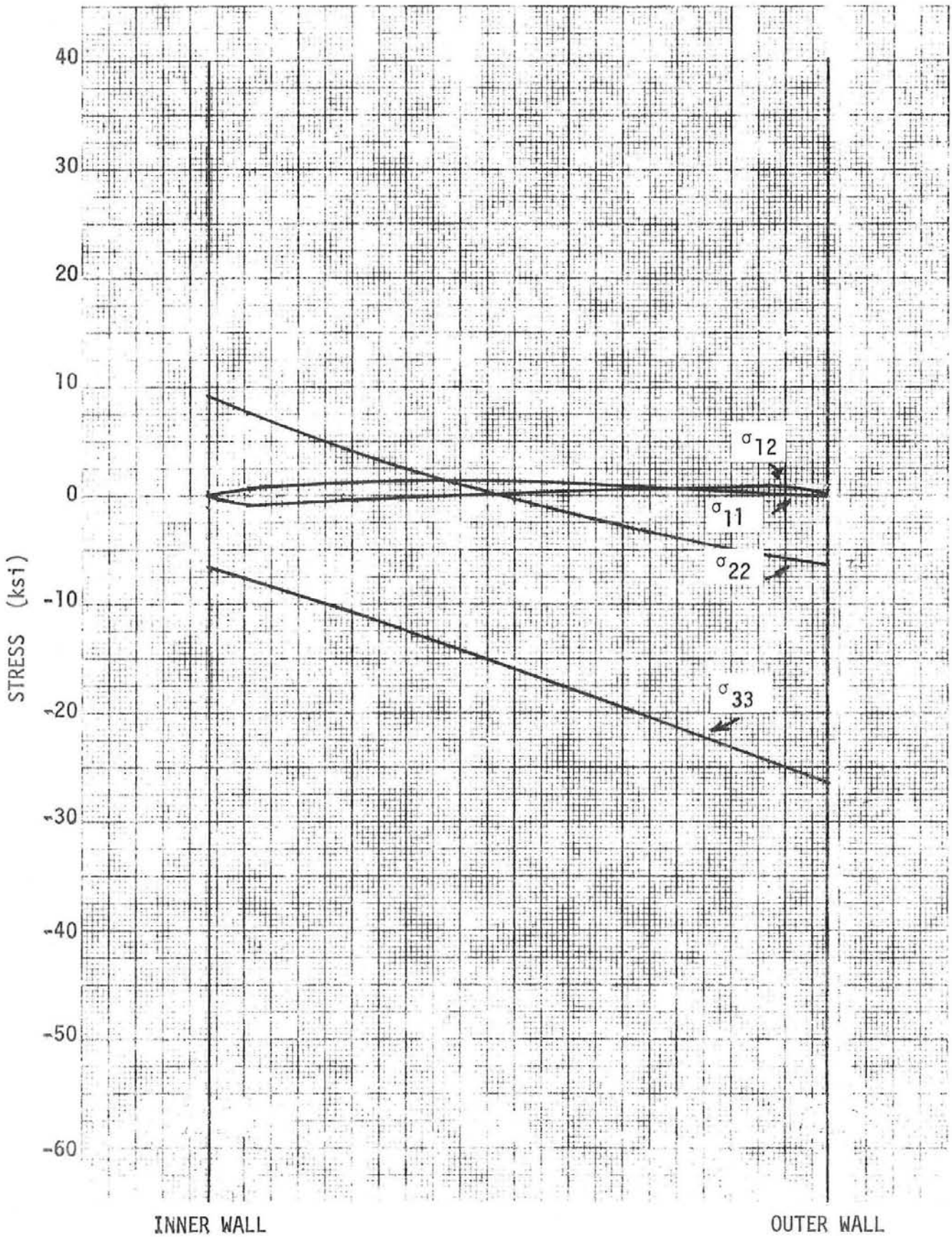

Figure 40. Stress Components at Minimum ΔT_w for the Pilot Plant with Model B at 8-s Period and Without Pressure Load

4. HYDRAULIC STABILITY INVESTIGATION

4.1 POSSIBLE MODES of INSTABILITIES

Components which transfer heat and experience phase change of the working fluid are candidates for both static and dynamic instability problems. The most common types are the static Ledinegg and the dynamic density-wave instabilities. Static instability is possible when the channel pressure drop versus mass flow rate characteristic has a negative sloping region and occurs when the pump characteristic has multiple intersections with the channel characteristic. The dynamic density wave instability results from interaction between flow and void generation. The solar receiver panels are investigated for both types of instabilities in this work.

In a system consisting of combinations of parallel and series segments, several modes of dynamic instability can occur. The important consideration in the analysis of this case is the choice of the constant-pressure points or boundaries of the system. For a solar receiver consisting of multiple tubes in parallel in each panel, and, in turn, multiple panels in parallel with each other, at least three modes of instability could occur in a selected panel.

In the first mode, only those few tubes which happen to receive a slightly higher heat flux or lower flow rate in any particular panel oscillate, or the tubes oscillate out of phase in such a manner that the constant-pressure boundaries are now the receiver panel inlet and exit. In this case the piping upstream and downstream of the panel headers does not participate and has no effect on the dynamics of the system.

In the second mode, all the tubes in a particular panel oscillate in phase, with oscillations between boiler panels out of phase. In this case the constant pressure boundaries become the common mixing plena upstream and downstream of the panels.

In the third mode, all the tubes and panels oscillate in phase. In this case the rest of the loop (i.e., the inlet piping from a selected constant pressure point to the boiler panel inlet and the exit piping from the boiler panel exit to the constant pressure point) participates in the dynamics of the system and, therefore, should be included in the mathematical model. The constant pressure points in this case are selected as the inlet and exit of a large mixing chamber. For this mode of oscillation the actual resistance of the piping is important.

The investigation of dynamic instability in this report is restricted to the first mode, i.e., inter-tube oscillations in a particular panel. Based on loop inspection, it is believed that this is the most likely mode of instability. The liquid single-phase flow resistance resulting from the control valve and the filter upstream of each boiler panel has a stabilizing effect, and, therefore, should contribute to make the second and third modes more stable than the first mode.

4.2 STATIC LEDINEGG INSTABILITY

The mass flow rate of the maximum and minimum heat flux conditions for the pilot and commercial plant receivers was varied and the pressure drop calculated with the thermal performance code, STAP. The pressure drop as a function of nondimensionalized mass flux for all four cases is presented in Figure 41 from 0.8 to 1.2 times the nominal mass flux. The results show complete positive sloping regions for the pilot plant receiver panels indicating no static Ledinegg instability. For the commercial plant receiver panels, short flat regions occur for both the maximum and minimum heat flux cases. However, the slope of the pump characteristics is probably still less than the channel characteristics, i.e.,

$$\left.\frac{\partial \Delta P}{\partial G}\right)_{\text{pump}} < \left.\frac{\partial \Delta P}{\partial G}\right)_{\text{channel}} \tag{21}$$

Consequently, no Ledinegg instability would occur for the commercial plant.

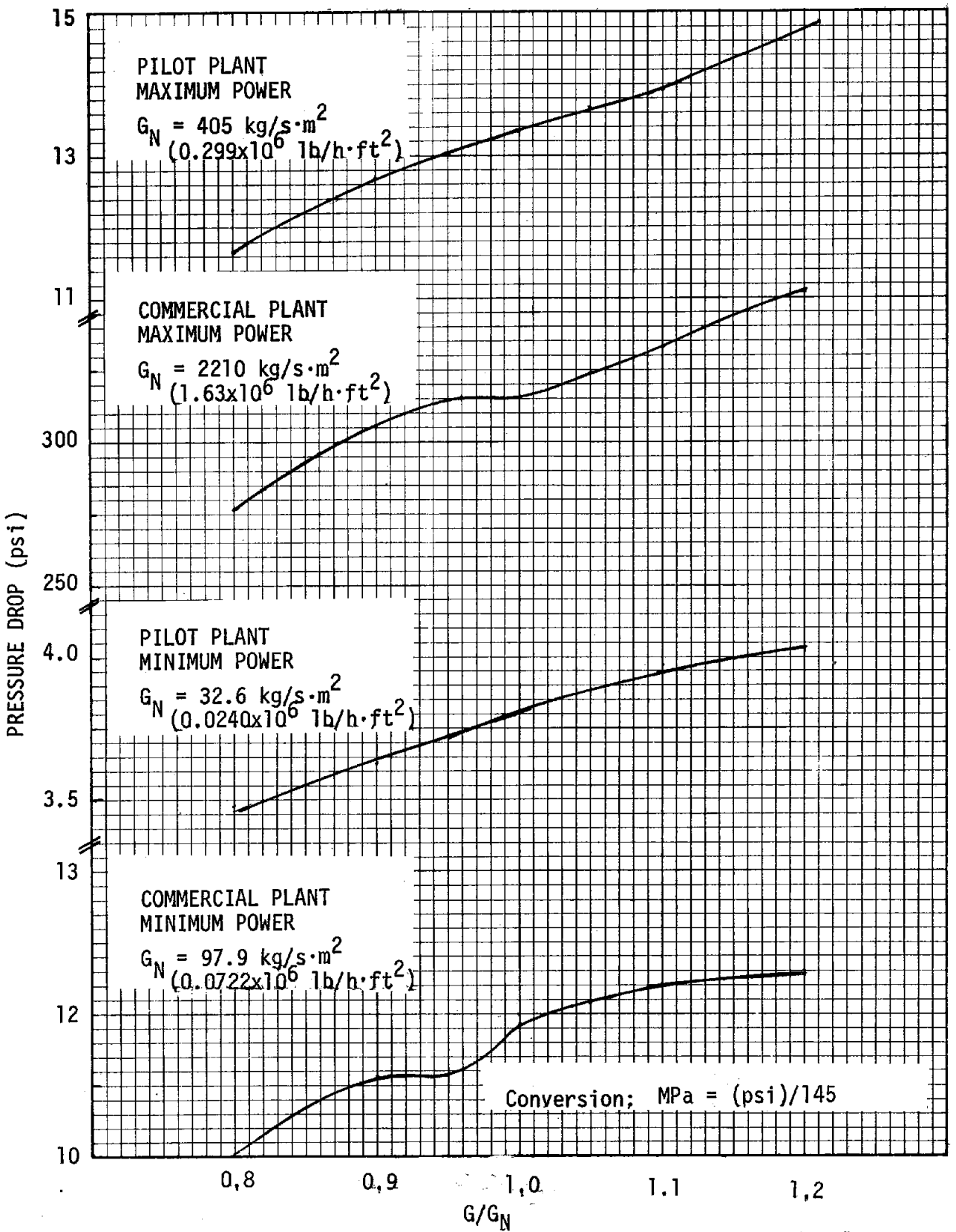

Figure 41. Pressure Drop as a Function of Nondimensional Mass Flux

4.3 DYNAMIC INSTABILITY MODEL

A relatively simple analytical model of a boiling channel was used to determine the occurrence of density wave instability in the solar receiver panels. The analytical tool, NUFREQ2, used for this analysis is a modified version of a frequency-domain model and code, NUFREQ, developed primarily for BWR stability investigations.[29,30] This code is capable of modeling a loop or portions of a loop consisting of a heated section, an unheated outlet riser, an unheated single-phase inlet portion, and a circulation pump, as illustrated in Figure 42. The various parts of the system can have an arbitrary orientation. The boundary condition used is that the pressure drop between two points is constant. The stability and dynamic response are investigated by oscillating the heated-section-inlet flow rate and examining the pressure drop perturbation between the boundary points by calculating the corresponding transfer functions.

The main modifications to the NUFREQ code include a change to account for axial variation of the heat flux in the single-phase liquid region, and an addition to include a superheat steam region. The former modification was previously added for application of the model to sodium-heated steam generators.[31] The modification to add the superheat regime was included as part of the current work to permit application to once-through steam generators. The model for the superheat regime includes both a heated region and an adiabatic riser. The analysis is similar to that performed in the two-phase boiling regime and is summarized in Appendix A.

The pilot plant and commercial plant panels were modeled to achieve an adequate dynamic representation of their features.

The main features and assumptions of the code and model are enumerated and discussed below:

(a) Constant-pressure system - The pressure gradient along the channel is considered to be small so that selective pressure dependant

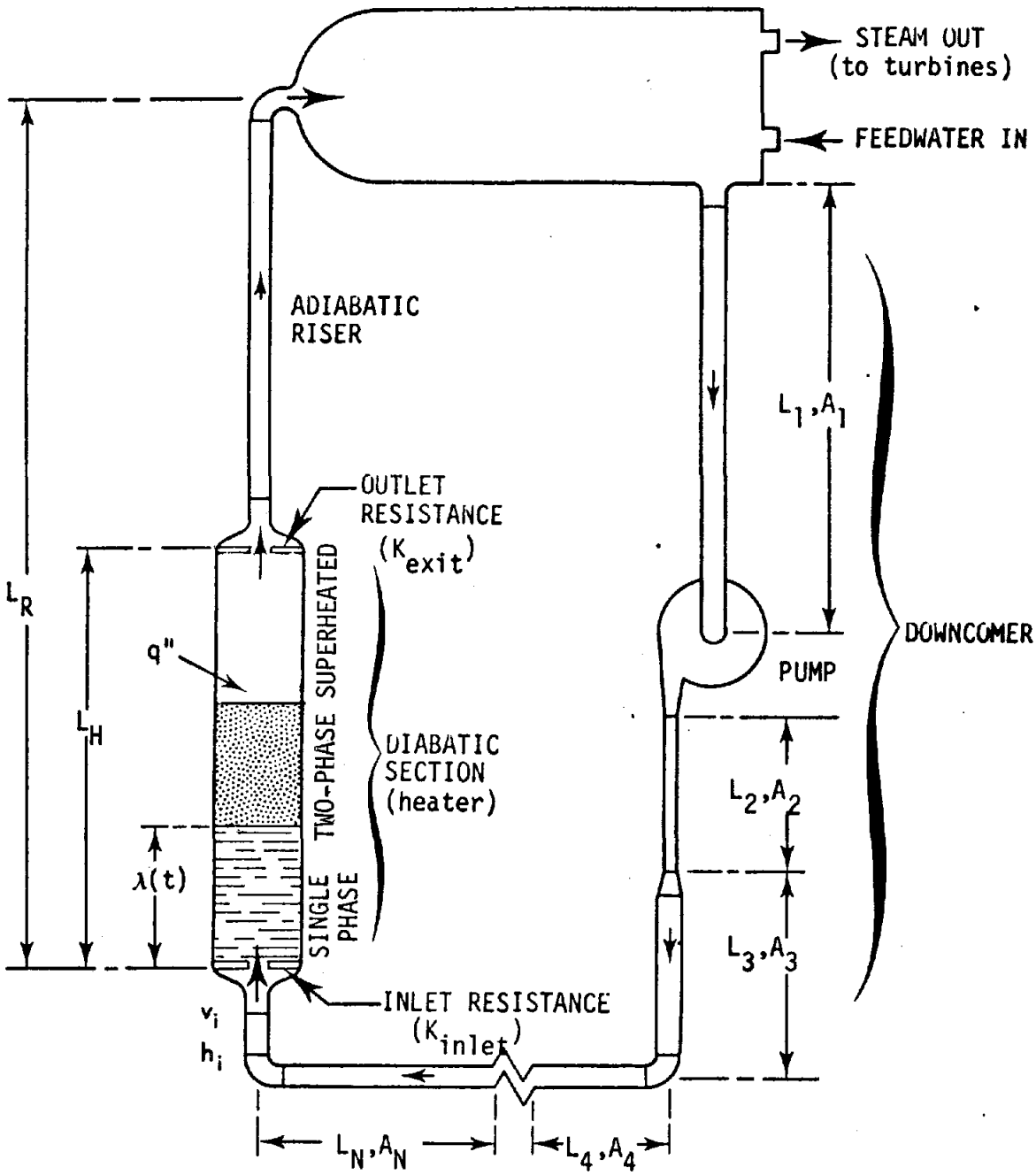

Figure 42. Representation of a Typical Test Section and Loop by the NUFREQ2 Code

properties are assumed constant. These properties include: liquid density, gas density in the two-phase flow region, specific heat in the subcooled region, and the latent heat of vaporization.

(b) Homogeneous two-phase flow in thermodynamic equilibrium - The NUFREQ2 code utilizes a simple homogeneous two-phase pressure drop model. Subcooled boiling in the single-phase region is not considered. In order to realistically represent the pressure drops in the single-phase, and two-phase and superheat regions of the panel tubes, the values initially calculated by NUFREQ2 were corrected to match the output from the panel thermal-hydraulic performance code, STAP. The effect of subcooled boiling in the single-phase region was partly included by adjusting the friction factor.

(c) Axial variation of heat flux - In the single-phase region the axial variation of heat flux is considered (in the modified version of NUFREQ) while uniform heat flux values are assumed in the boiling region and the superheat region. For steam generators exhibiting strong axial variations of the heat flux, it is important to predict correctly the location of the boiling boundary (point where flow reaches saturation under assumed equilibrium conditions). Indeed the location of this point strongly influences the dynamics of the boiling channel. The effect of nonuniform heat flux distribution on the pressure drop in the two-phase region is probably less important since most of the frictional pressure drop occurs near the exit of the channel and, therefore, depends mostly on the exit quality rather than the axial quality distribution.

(d) Tube wall - The tube is assumed uniformly thick, thereby neglecting the effect of the weld on the back side between each two adjacent tubes. A sensitivity analysis is used to check this assumption.

(e) Circumferential variation of heat flux - The heat flux is uniformly distributed around the circumference of the tube, thereby, neglecting the effect of one-sided heating. A sensitivity analysis is used to check this assumption.

(f) Unheated sections at the inlet and outlet of the tubes - The unheated horizontal portion (0.43 m for the pilot plant and 0.46 m for the commercial plant) of the tubes at the exit was modeled as a horizontal riser. The outlet bend was represented with a loss coefficient. The total resistance of the unheated inlet piping (including the inlet contraction, the resistance of the pipe and any local resistance from bends) was accounted for as an inlet orifice loss. There is no approximation involved in such a representation of the system.

4.4 DYNAMIC STABILITY EVALUATION

The stability of the pilot and commercial plant receiver panels was examined by oscillating externally the inlet flow rate and observing the response of the pressure drop perturbation. The system crosses the threshold of instability for a certain state (i.e., for a set of operating conditions) and at a given oscillation frequency, when the calculated pressure drop perturbation between two points of imposed constant pressure vanishes. Under those conditions, since the boundary conditions imposed on the system are satisfied with oscillatory flow, the system becomes unstable. Denoting by $\delta\Delta p_1$, $\delta\Delta p_2$, and $\delta\Delta p_3$ the pressure drop perturbations in the single-phase liquid, two-phase boiling, and single-phase gas portions of the system considered, at the threshold of instability, for a certain frequency ω, we have

$$\delta\Delta P_1(\omega) + \delta\Delta P_2(\omega) + \delta\Delta P_3(\omega) = 0 \qquad (22)$$

A convenient stability criterion can be developed from Equation (22) and illustrated in terms of the Nyquist plot. The Nyquist plots of this report represent the ratio $(\delta\Delta P_2(\omega) + \delta\Delta P_3(\omega))/\delta\Delta P_1(\omega)$. The system becomes unstable when the locus of the "open-loop transfer function" crosses the real axis to the left of the -1 point.

4.4.1 Pilot Plant

The Nyquist plots for the pilot plant receiver panels with no inlet orificing for maximum and minimum heat flux conditions are presented in Figures 43 and 44, respectively, and the results are summarized in Table 8. The results show that the system is unstable for both conditions. The oscillation period for onset of instability is 9.4 s for the maximum heat flux condition. For the minimum heat flux condition, several periods are likely for the onset of instability, from a high value of 76 s to a low value of 6.4 s.

The ratio of steady-state values of the single-phase liquid frictional pressure drop, $\Delta P_{\ell,fr}$, to the total pressure drop, $\Delta P_{tot,fr}$, can be used as a rough parameter correlating stability. Criteria based on the value of this ratio required for stability vary widely in the literature.[32] One of the most notable is the Griffith criterion which states that two conditions must exist before density oscillations will occur: (1) the ratio of the exit specific volume to the specific volume of the inlet liquid phase should be greater than three and (2) the pressure drop in the liquid phase should be less than one-third the total pressure drop.

For the pilot plant cases, the ratios of specific volumes are about 23 and the pressure drop ratios $\Delta P_{\ell,fr}/\Delta P_{tot,fr}$, summarized in Table 8, are 0.031 and 0.018 for the maximum and minimum heat flux conditions, respectively. Thus, the Griffith criterion confirms the possibility of dynamic instability as predicted with NUFREQ2.

The degree of instability of a system can be examined by progressively varying some parameter and observing the approach toward stability. In the present case, this was done by increasing the loss coefficient, K_{or}, for a tube inlet orifice, thereby increasing the inlet pressure drop. For the maximum heat flux condition, cases were run with K_{or} = 50, 100, 125, and 150. The results show that K_{or} = 125 is the lowest K_{or}-value at which the system is stable. The Nyquist plot for this case is presented in Figure 45. For the

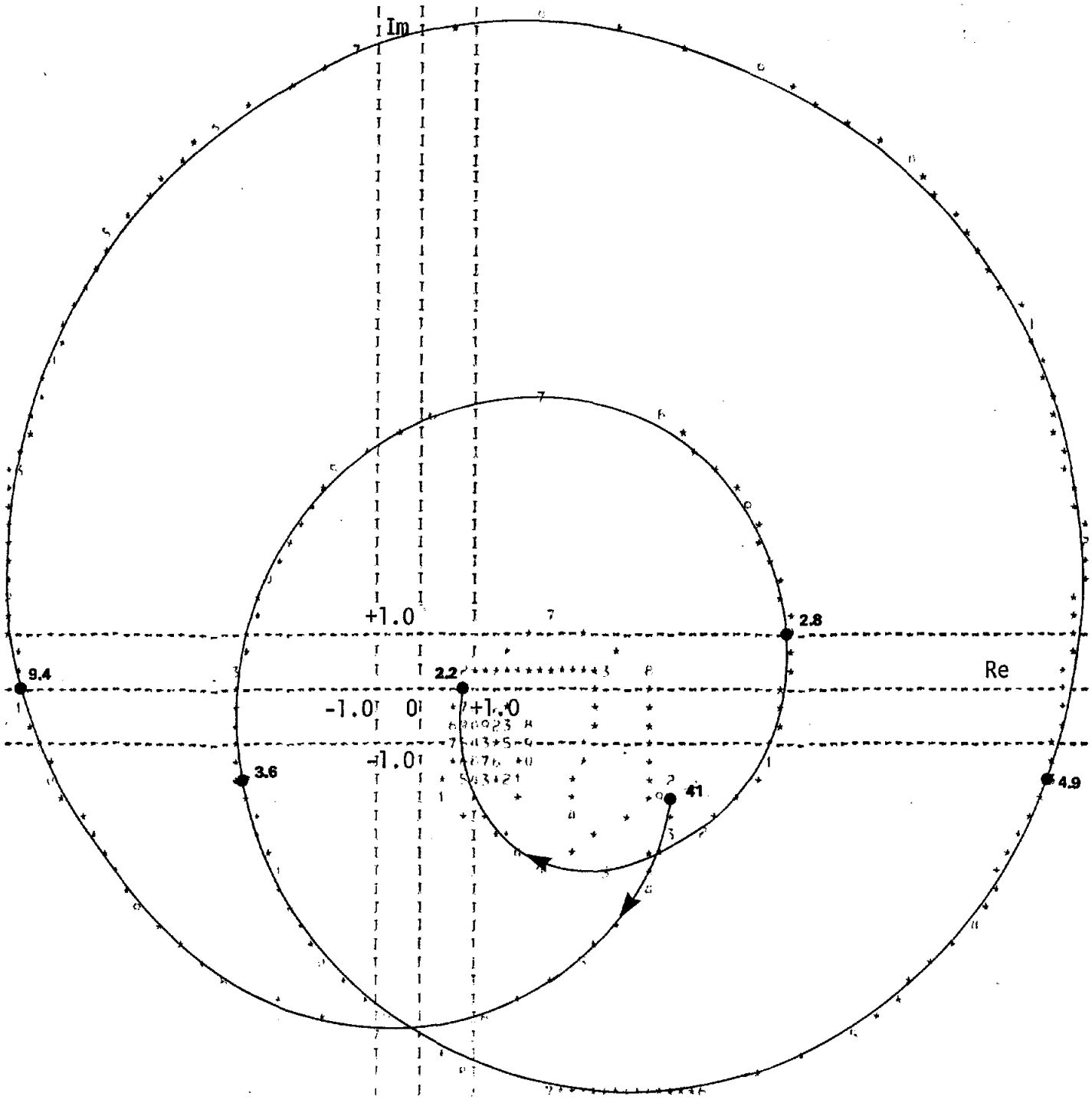

Figure 43. Nyquist Plot for the Pilot Plant Receiver Panel with Maximum Heat Flux and K_{or} = 0. (The oscillation period is marked on the locus in seconds.)

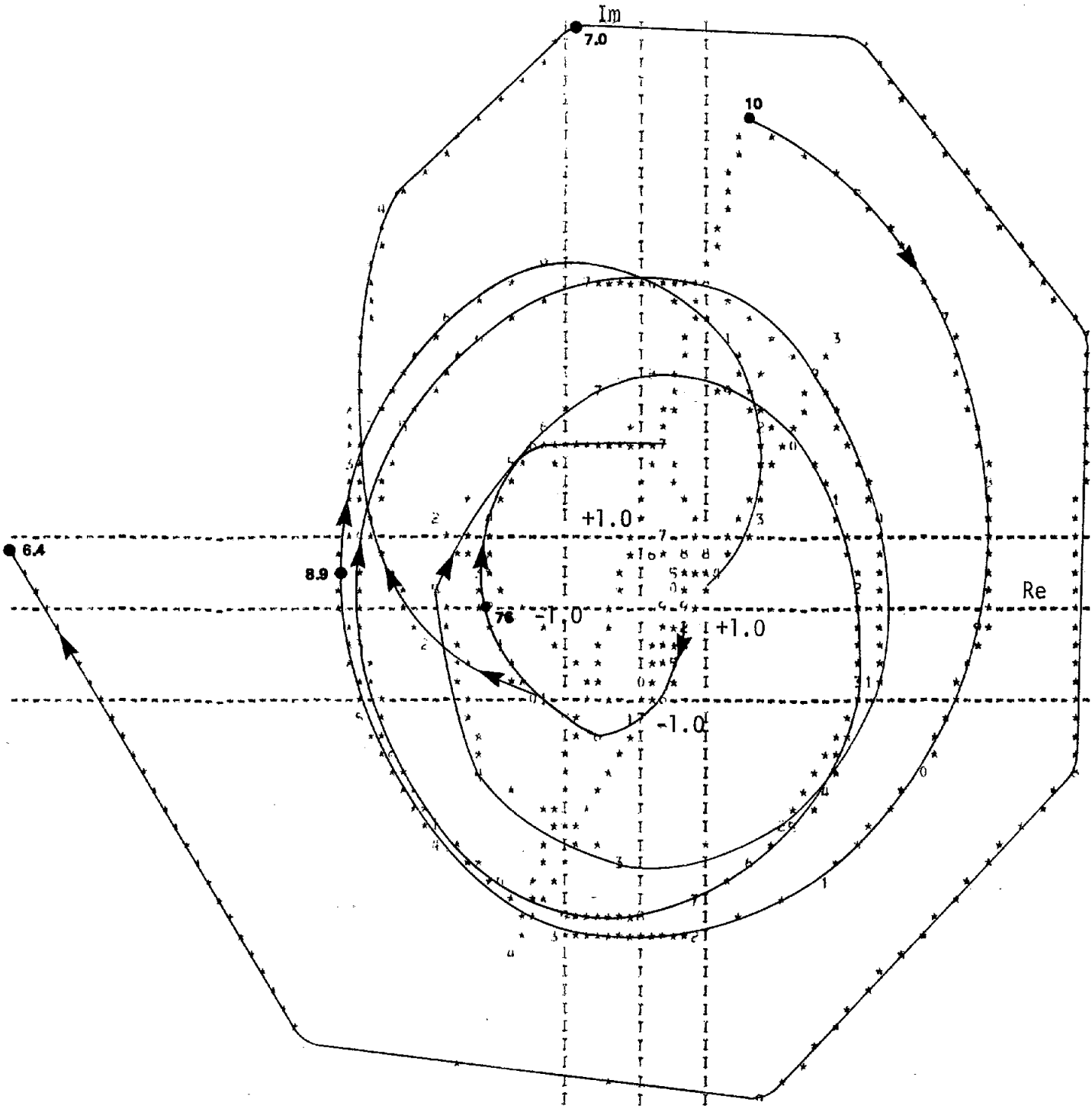

Figure 44. Nyquist Plot for the Pilot Plant Receiver Panel with Minimum Heat Flux and K_{or} = 0. (The oscillation period is marked on the locus in seconds.)

TABLE 8 - Dynamic Stability Results

Plant	Maximum Incident Heat Flux MW/m^2	K_{or}	PREDICTED State	Period for Instability s	$\frac{\Delta P_{\ell,fr}}{\Delta P_{tot,fr}}$	ΔP_{or} KPa	(psi)
Pilot	0.295	0	Unstable	9.4	0.031	0	
	0.053	0	Unstable	76,8.9,6.4	0.018	0	
	0.295	125	Stable	-	0.21	14.4	(2.09)
	0.053	1500	Unstable	36.	0.58	1.1	(0.16)
Commercial	0.850	0	Unstable	4.9	0.044	0	
	0.072	0	Unstable	85,35,22.5	0.033	0	
	0.850	125	Stable	-	0.27	414	(60.1)
	0.072	1500	Stable	-	0.10	9.1	(1.32)

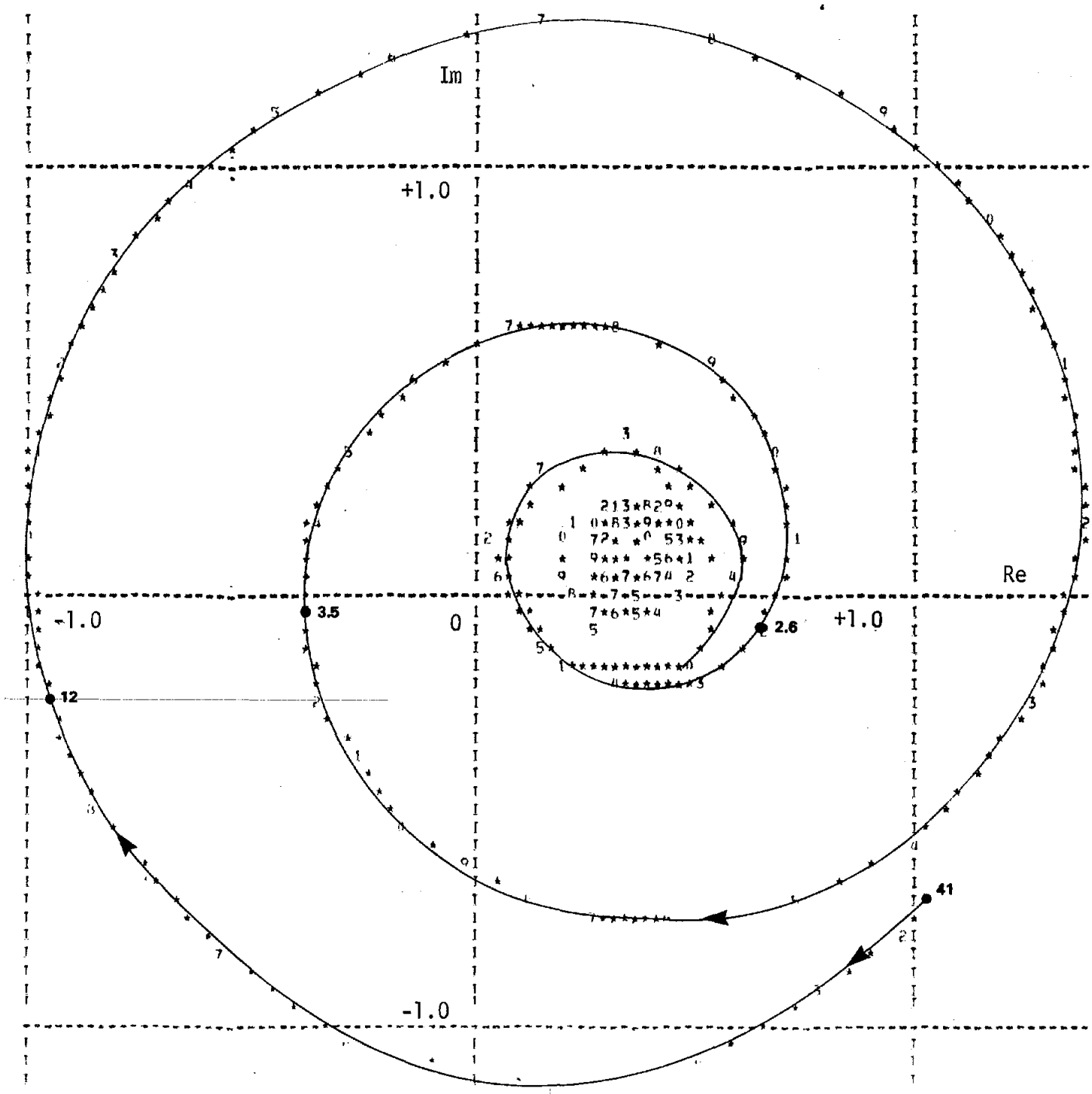

Figure 45. Nyquist Plot for the Pilot Plant Reciever Panel with Maximum Heat Flux and K_{or} = 125. (The oscillation period is marked on the locus in seconds.)

minimum heat flux condition, K_{or} was increased to 1500 and the predicted performance shows the system still unstable, as illustrated with the Nyquist plot in Figure 46. The dynamic stability results with orificing are also summarized in Table 8. The orifice diameter corresponding to K_{or} = 125 and 1500 are estimated as 3.3 mm (0.129 in.) and 2.4 mm (0.093 in.), respectively.

The instability for the minimum heat flux condition was not investigated for K_{or} greater than 1500 because the resulting small orifices are prone to plugging by deposition of scale.

The low mass flux of 32.6 kg/s•m^2 (0.024x10^6 lb/h•ft^2) for the pilot plant receiver tubes with minimum heat flux may contribute to flow regime instabilities. The inlet and exit velocities of 0.043 m/s (0.14 ft/s) and 1.0 m/s (3.3 ft/s) are very low. An estimate of the associated flow regime indicates that the tubes may experience unstable, chugging slug flow.

4.4.2 Commercial Plant

The Nyquist plots for the commercial plant receiver panels with no inlet orificing for maximum and minimum heat flux conditions are presented in Figures 47 and 48. The results show that the system is unstable for both cases. The results are also summarized in Table 8. The ratios of exit to inlet specific volumes are greater than three and the pressure drop ratios, $\Delta P_{\ell,fr}/\Delta P_{tot,fr}$, also summarized in Table 8, are less than 0.33 and, therefore, confirm the instability according to the Griffith criterion.

Inlet orificing was increased, as for the pilot plant, to observe the system approach to stability for the commercial plant cases. The cases become stable with values of K_{or} = 125 for the maximum heat flux condition and K_{or} = 1500 for the minimum heat flux condition. The corresponding Nyquist plots are shown in Figures 49 and 50 and the results are summarized in Table 8.

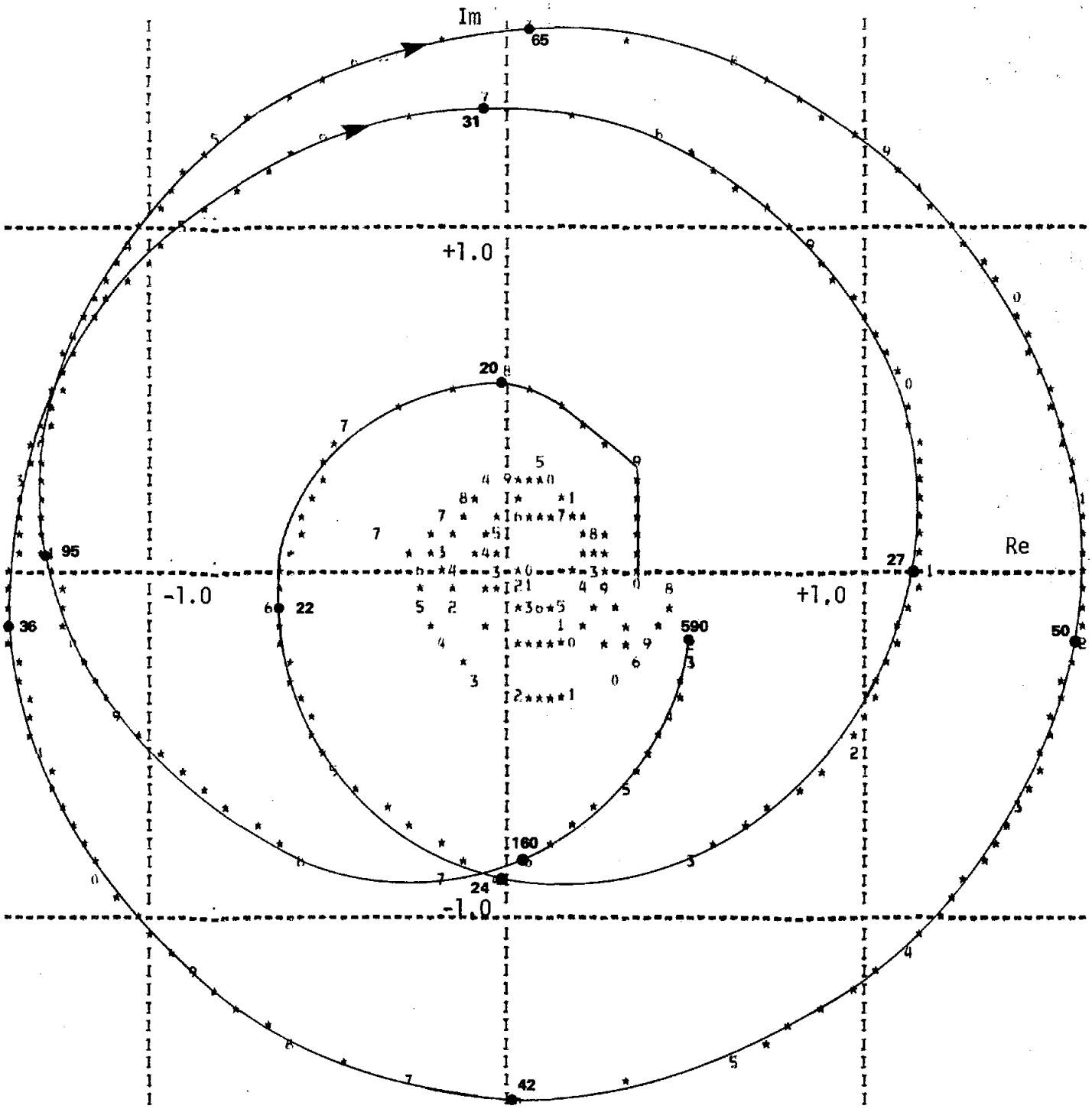

Figure 46. Nyquist Plot for the Pilot Plant Receiver Panel with Minimum Heat Flux and K_{or} = 1500. (The oscillation period is marked on the locus in seconds.)

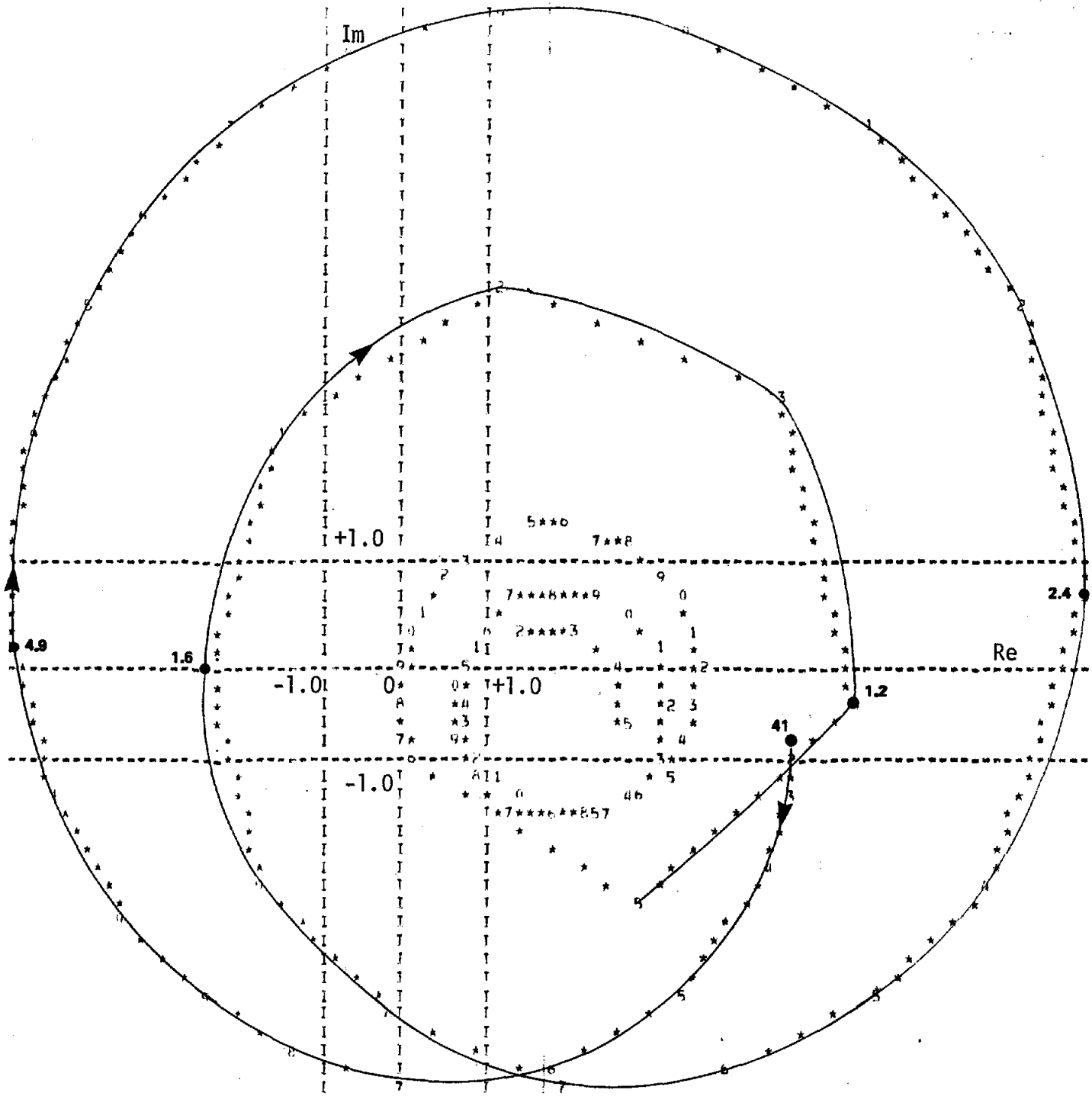

Figure 47. Nyquist Plot for the Commercial Plant Receiver Panel with Maximum Heat Flux and K_{or} = 0. (The oscillation period is marked on the locus in seconds.)

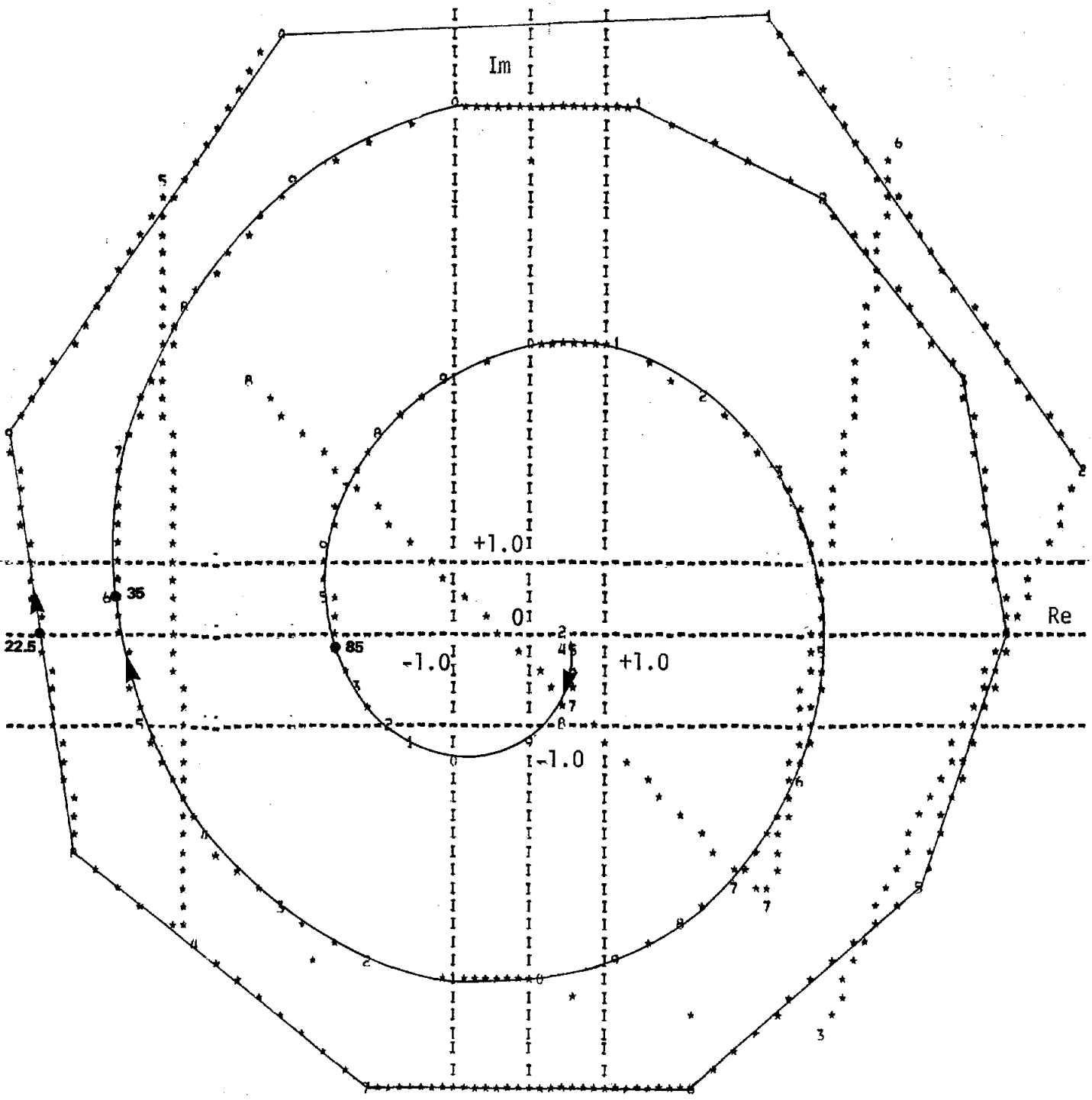

Figure 48. Nyquist Plot for the Commercial Plant Receiver Panel with Minimum Heat Flux and K_{or} = 0. (The oscillation period is marked on the locus in seconds.)

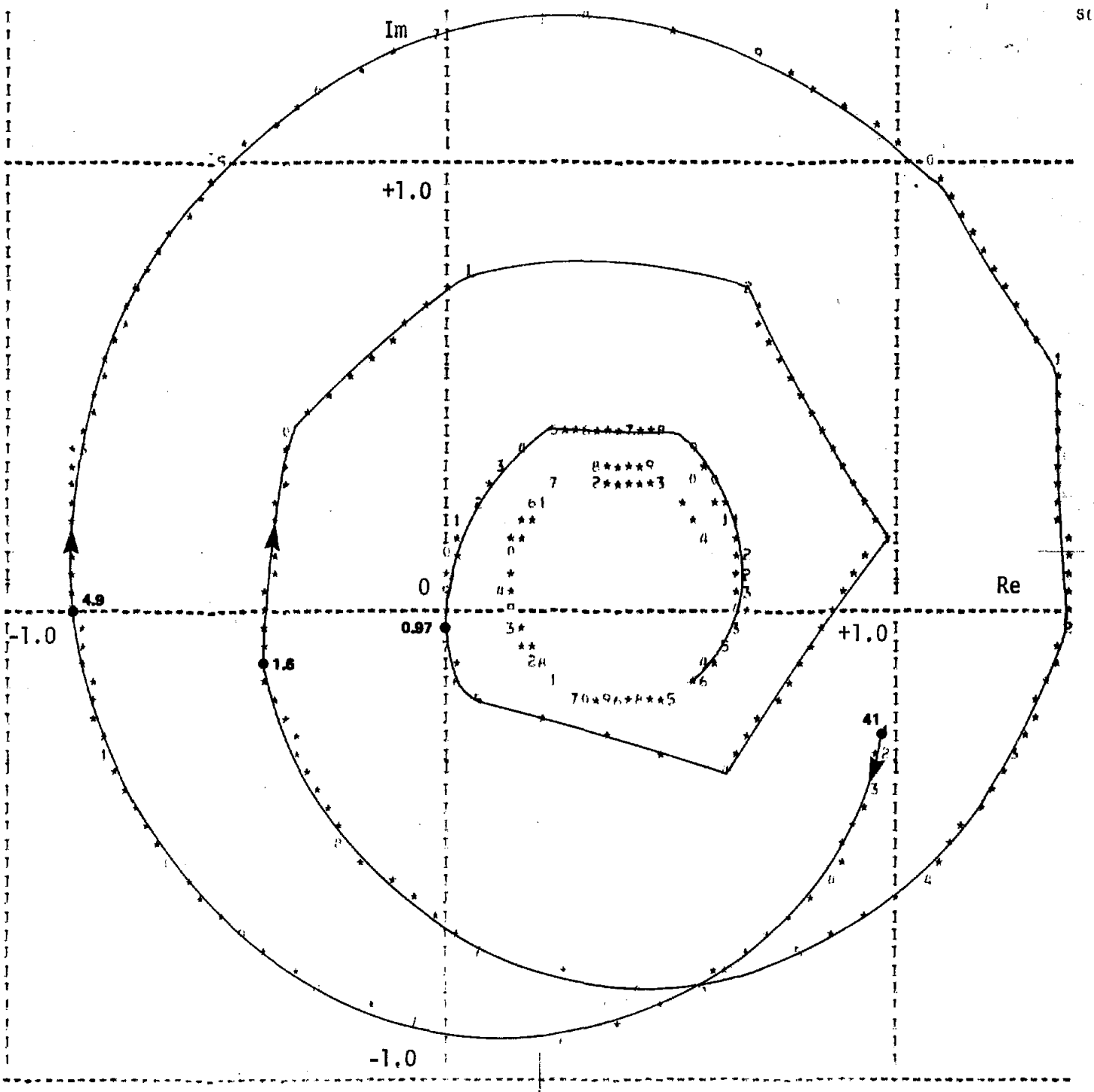

Figure 49. Nyquist Plot for the Commercial Plant Receiver Panel with Maximum Heat Flux with K_{or} = 125. (The oscillation period is marked on the locus in seconds.)

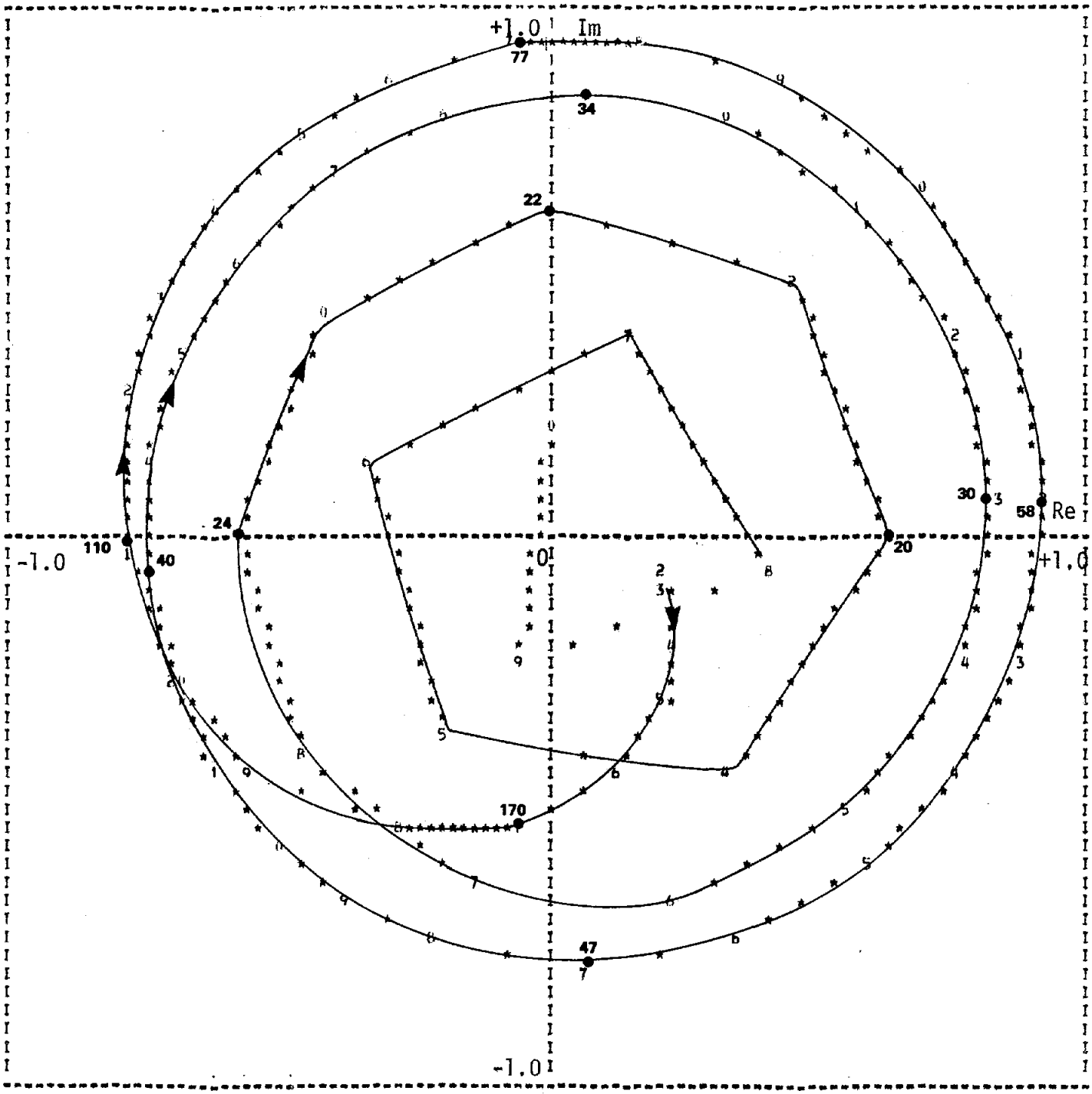

Figure 50. Nyquist Plot for the Commercial Plant Receiver Panel with Minimum Heat Flux with K_{or} = 1500. (The oscillation period is marked on the locus in seconds).

4.4.3 Sensitivity Runs and Code Validations

Conditions for the pilot plant receiver panels for the maximum heat flux condition were varied to assess the sensitivity of the results predicted with NUFREQ2 to some of the model assumptions. A case was run with the tube wall thickness increased to account for the tube-to-tube welds which were neglected in the original model. A comparison of these results with the original model results shows nearly identical instabilities according to the Nyquist plots.

The effect of variation of heat flux around the periphery of the tube was neglected in the original NUFREQ2 model. To check the validity of this model simplification, a case was run with the heated perimeter decreased by two and the heat flux increased by two. A comparison of the new results with the original model results again shows nearly identical instabilities. It is concluded that the circumferential heat flux variation has negligible effect on the stability predictions.

The effect of nonuniform axial heat flux distribution near the exit in the superheat region was neglected in the original NUFREQ2 model by using a uniform heat flux throughout the superheat region. A case was run to check the effect of this simplification in the model. The lower heat flux region near the exit was modeled with an adiabatic riser and the heat flux in the heated two-phase region was increased to obtain the same tube exit conditions. A comparison of the new results with the original model results shows nearly identical instabilities with a slight increase in the oscillation period for onset of instability from 9.4 s for the original case to 12.0 s for the new case.

The NUFREQ2 code was also checked by running a case for conditions corresponding to a 5-tube panel test, conducted by Rocketdyne with electric radiant heat to simulate solar radiation.[1] The test tube material and cross section are identical to the pilot and commercial tubes. However, the test tube is 17 m (56 ft) long compared with 12.5 m (41 ft) for the pilot plant and 25.5 m

(83.7 ft) for the commercial plant. Operating conditions for Test No. 15 are compared with the pilot plant maximum heat flux condition in Table 9. While the conditions are comparable, they are not identical. Since there is a significant difference in subcooling and tube length it is not known, based upon inspection, which system might be more stable.

NUFREQ2 predictions for the 5-tube panel test show that the test panel is unstable with an oscillation period of 14 s for the onset of instability. Reference 1 indicates that no instability was observed for this test. Consequently, there is a discrepancy. It is believed that the assumptions and simplifications in the NUFREQ2 code are such that the predictions are conservative, i.e., the predicted orificing to obtain stability is overpredicted. This conservatism could be removed with an improved state-of-the-art stability code. In particular, the two-phase flow model which is assumed homogeneous in NUFREQ2 could be improved with a separated flow model.

The NUFREQ2 code is a linearized frequency-domain code and, therefore, cannot predict the amplitude of the oscillations at the threshold of instability. If these amplitudes were small it is quite possible that they would not have been observed without ad hoc instrumentation. It is, therefore, possible that a mild inter-tube instability did exist for the test conditions, but it was not observed because of inadequate instrumentation. An inter-tube instability can generally be observed by measuring individual tube flow rates or outlet superheated steam temperatures. Measurements of overall inlet-to-outlet plenum pressure drop or individual plenum pressures may not reveal inter-tube oscillations. In fact, the NUFREQ2 model assumes that the plenum regions are constant pressure points.

TABLE 9 - Comparison of Test Conditions and Pilot Plant Conditions

	Pilot Plant Maximum Heat Flux	5-Tube Panel Test No. 15 (Ref. 1, p. 6-53)
Tube length m	12.5	17
Mass Flux, $kg/s \cdot m^2$ 10^6 $lb/h \cdot ft^2$	405 (0.299)	346 (0.255)
Absorbed power, kW/tube	31.7	33.1
Average absorbed heat flux, MW/m^2	0.20	0.15
Inlet Temperature, °C (°F)	288 (550)	232 (450)
Inlet Pressure MPa psia	10.54 (1528)	10.10* (1465)*

* The pressure is given in Reference 1, p. 6-45, as 400 psig. Following discussions with E. Cull of Sandia, this value was changed to 1465 psia.

5. WATER CHEMISTRY EVALUATION

It is becoming increasingly evident that the chemical ionic content of steam generating water plays a key role in the performance of electric power generating plants. Recent history shows that turbines and steam generators can sustain disabling degrees of damage which require lengthy outages and expensive modification or repairs.

Material selection in power generating plants has become paramount. Copper is a particular metal that has drawn attention. Problems have been experienced with balance of plant performance because of the high copper concentration, and ammonia-copper presents a delicate balance problem in the condenser. It has been postulated that Cu Cl_2 may increase the corrosion rate of Incoloy 800. Also, copper in feedwater transfers with steam and deposits on turbine blades or plates out as metallic copper in the boiler region which presents difficulties during subsequent cleaning operations. Therefore, it is recommended that the 90-10 copper-nickel alloy condenser in the MDAC solar plants be replaced. Titanium is an attractive substitute. Experiences to date have been outstanding. Failure modes for Titanium condenser tubes include mechanical and vibration damage, both of which can be controlled with proper design. Titanium cost is high and its thermal conductivity is low. However, because of its resistance to corrosion, erosion, and impingement attack, thin wall tubes can be utilized making cost and effectiveness comparable to other condenser tubes while negating the problems mentioned above with copper based materials. Another candidate for condenser material is Type 304 stainless steel. It has been used rather extensively for fresh water service. One weakness is the susceptibility to pitting corrosion.

A review was made of modern boiler water practices for the purpose of specifying water purity for the Solar Thermal Power System. In the operation of a once-through system, where entering contaminants either foul boiler tubes or carry over in soluble form into the turbine which has little tolerance for

deposits, marginal feedwater is unacceptable and, since blowdown is not possible in this design, initial high water quality is necessary. Full flow demineralization (condensate polishing) is proposed to protect the boiler and turbine from the effects of such intrusions. The addition of volatile species ammonia and hydrazine was used in the cycle for pH and oxygen control. Condensate polishers afford high flow rates and although their primary function is to remove dissolved species, they also act as mechanical filters for suspended corrosion products (resulting from condenser leakage). Full flow condensate polishing has the following advantages:

1. Protection against condenser leakage.
2. Decreased turbine fouling rate (therefore, increased efficiency).
3. Longer intervals between system cleaning.
4. Decreased system startup time.

Economically, full flow condensate polishers represent a high capital cost investment and further cost in regeneration; however, increased plant availability more than offsets initial capital outlay.

The recommended feedwater specification using state-of-the-art methods are listed below:

Total Solids	50 ppb (maximum)
Dissolved oxygen	7 ppb (maximum)
Silica	20 ppb (maximum)
Iron	10 ppb (maximum)
Copper	2 ppb (maximum)
pH at 25°C	9.3 to 9.6
Hydrazine	5 ppb (maximum)
Conductivity (cation) at 25°C	0.3 micro/mho/cm (maximum)
Sodium	2 ppb (maximum)
Chloride	2 ppb (maximum)

The silica is controlled to avoid harmful deposits on the turbine. The pH range is chosen to protect a carbon steel feedwater train; ammonia is used to adjust the pH. The iron and copper values limit the amount of acceptable corrosion and depositable material from the preboiler system. The conductivity value is to guard against break-through from the demineralization columns of potentially harmful salts from condenser leaks. The hydrazine limit is imposed to avoid overfeeding with consequent release of hydrogen. Also included is a requirement that the sodium concentration be less than 2 ppb in order to limit the amount of potential caustic in the system.

It is recommended that an instrument system to measure ion concentrations in the water be installed. The recent introduction of an ion exchange-chromatographic technique with conductimetric end point detection affords a sensitive technique for both anion and cation measurements. Ion exchange chromatography is now being introduced in U.S. power plants with an objective to adopt it as a continuous on-line analytical method. General Electric has taken steps to actively participate in this introduction and will be in a good position to assess its merits and recommend adoption to the power plant chemistry instrumentation system.

6. TESTING RECOMMENDATIONS

Tests conducted by Rocketdyne[1,21] to support the receiver panel design were reviewed. Tests with a single tube and with a 5-tube panel with 19.8 m (65 ft) length were conducted in the horizontal position[21] and tests with a single tube, 5-tube panel, and a 70-tube panel with 17.1 m (56 ft) length were conducted in the vertical position. In no cases were the operating conditions proposed for the pilot plant or the commercial plant receiver panels for either maximum or minimum heat flux conditions duplicated. Also, the test sections were generally not instrumented in sufficient detail to provide the data needed to validate the performance predictions presented in this report. Consequently, tests to duplicate the proposed operating conditions are recommended. Additional tests at a range of conditions are also recommended to provide a data base for model verification. The models can then be used with confidence to evaluate off-design conditions not tested. Data from the following specific types of tests are needed to validate the analyses in this report and, thereby, support the receiver boiler panel design.

a. Thermal performance - Overall thermal performance for the proposed design conditions should be verified with thermal performance tests. Thermal performance at off-design or part-load conditions not tested can be predicted with thermal performance correlations and an appropriate model. The correlations used in this report are based on uniform circumferential heating. The large nonuniform circumferential heat flux which occurs in the solar-heated receiver panels, could have an effect on the correlations. The largest uncertainty in performance predictions for once-through units generally results from uncertainties in the CHF correlations and the film boiling correlation. Consequently, it is recommended that at least these correlations be verified.

b. Temperature oscillations associated with CHF - The thermal-stress analysis presented in this report is based on a rivulet model originally conceived to simulate the temperature oscillation amplitude and frequency measured during CHF tests conducted at ANL with a sodium-heated steam generator tube. The oscillation amplitude varies with the number of rivulets and the percent wetness. It is not well-known how the amplitude and frequency vary with mass flux and heat flux.

   Consequently, test data for both the pilot and commercial plant tubes for conditions corresponding to the worst temperature oscillations are needed to verify the current model or form the basis for a new model. Test data should include measurement of at least amplitude and frequency of the temperature oscillations. It is recommended that these temperatures be measured with thermocouples embedded in the tube wall similar to the arrangement used in a sodium-heated steam generator tube tested by ANL.[22] The closer the thermocouples are to the inside wall surface the better the measurements are because less high frequency oscillations are damped in the tube wall.

c. Dynamic stability tests - The NUFREQ2 code predicts that inter-tube dynamic instabilities exist for both the pilot and commercial plant for maximum and minimum heat flux conditions without inlet orificing. Multi-tube panel tests are required to validate these predictions, which are believed to be conservative, at the proposed operating conditions. The panels should be instrumented to measure individual tube flow rates or pressure drop from inlet plenum to a point at about the middle of the tubes, and individual tube superheated steam outlet temperatures.

The scope of the testing recommendations portion of this report is limited primarily to giving objectives for the type of testing needed to provide performance validation of the analyses presented in this report and, thereby, support the receiver boiler panel design. Detailed test planning which includes specification of hardware, instrumentation, and test conditions is necessary to achieve the objectives. These aspects are not addressed in this report. It is recommended that personnel who are to be involved in final evaluation of data, also be involved in the detailed test planning or a review and comment phase of such planning to assure test adequacy.

7. SUMMARY AND CONCLUSIONS

Analyses and reviews to evaluate selective features of receiver designs proposed by McDonnell Douglas Astronautics Company for a 10-MWe pilot and 100-MWe commercial solar electric power plant have yielded the following principal results:

a. Thermal performance analysis - Overall thermal performance conditions are predicted for maximum and minimum heat flux conditions for the pilot and commercial plant receiver boiler panels with a steady-state code, including parameters to take into account some two-dimensional effects. Empirical correlations utilized in the code are summarized in Tables 1 and 2. Thermal performance results are in turn summarized in Table 3 and boundary conditions for the subsequent thermal-stress cycling analysis, associated with temperature oscillations in the transition boiling region, are summarized in Table 4.

b. Thermal-stress cycling analysis - A rivulet model initially developed to simulate the measured temperature oscillations in the transition boiling region of a sodium-heated steam generator tube formed the basis for two models for the solar-heated tubes. Model A has two rivulets oscillating on the front side of the tubes, i.e., the side exposed to solar radiation, and Model B has four oscillating rivulets equally spaced all around the periphery of the tube. A general purpose finite element thermal-stress code was used to evaluate temperature and stress oscillation magnitudes for the pilot plant receiver with maximum heat flux and the commercial plant receiver with maximum and 80% of maximum heat flux conditions. The results of the analysis show that the fatigue life for the pilot plant receiver tubes is longer than the required design life of 30 years. However, for the commercial plant tubes with the maximum heat flux condition, the fatigue life is predicted equal to 15 years based on ASME Code

Section III, Subsection NA. An analysis for the commercial plant with a reduced heat flux condition corresponding to 80% of the maximum heat flux condition results in a fatigue life of 51 years.

c. Stability analysis - Results from a frequency-domain model, NUFREQ2, show that inter-tube instabilities exist for the maximum and minimum flow conditions for both the pilot and commercail plant receiver tubes without inlet orificing. When inlet orificing is applied and the orifice coefficient is increased to K_{or} = 125, both cases corresponding to the maximum heat flux condition for the pilot and commercial plants become stable. For the minimum heat flux conditions, orificing must be increased to K_{or} = 1500 before the commercial plant receiver tubes are stable. Even for this large value of K_{or} the minimum heat flux condition for the pilot plant is still unstable. The extremely low velocity conditions specified for minimum heat flux operation are unusual and merit special considerations; chugging instabilities may develop under such conditions.

d. Water chemistry evaluation - A review of water chemistry practices proposed for the solar-heated receivers resulted in several recommendations. It is recommended that the 90-10 copper-nickel alloy condenser be replaced with a substitute unit made from titanium or Type 304 stainless steel. Also, full flow demineralization (condensate polishing) is proposed to protect the boiler and turine from the effects of contaminants. Recommended feedwater specifications are also given.

e. Testing recommendations - Testing recommendations are made to provide data to validate the analyses presented in this report and, thereby, improve the thermal-hydraulic design basis for the solar-heated receivers. Tests should be conducted to include the proposed pilot

and commercial plant receiver conditions corresponding to the maximum and minimum heat flux conditions. Specific tests should be conducted to: (1) determine overall thermal performance and validate selective correlations, which have a substantial impact on the accuracy of performance predictions, in particular the CHF correlation which may be affected by nonuniform circumferential solar heating; (2) determine amplitude and frequency of temperature oscillations in the transition boiling region following CHF; and (3) evaluate inter-tube stability.

ACKNOWLEDGEMENTS

This work was performed under GE-Sandia Contract No. 18-2969 under the direction of E. Cull of Sandia Laboratories.

Dr. G. Yadigaroglu of the University of California, Berkeley, served as a consultant on this work in particular for the dynamic stability analysis, under Consultant Agreement for the Fast Breeder Reactor Department, General Electric Company, P.O. No. 190-K8A14.

J. R. Medley, W. Palmer, and B. R. Bicknell are acknowledged for computer analysis support, and P. J. Ring, for consultation on material properties.

NOMENCLATURE

English Letters

D_i	Inside diameter
D_o	Outside diameter
C_1, C_2, C_3	Parameter defined when introduced
F	Radiation view factor
f	Coefficient of friction
Fr	Froude Number
g_1, g_2, g_3	Functions
G	Mass Flux
h	Heat transfer coefficient
h_f	Film boiling heat transfer coefficient
h_n	Nucleate boiling heat transfer coefficient
H	Enthalpy
k	Tube wall thermal conductivity
k_{or}	Orifice loss coefficient defined as the total pressure loss across the orifice nondimensionalized with the tube inlet dynamic pressure
q	Heat transfer rate
q_c	Convective heat loss
q_e	Emitted radiation heat loss
q_r	Reflected radiation heat loss
q_a''	Absorbed heat flux based on projected outside tube area
q_i''	Incident heat flux based on projected outside tube area
Q	Heat load
P	Pressure
P_r	Thermodynamic reduced pressure
Re	Reynolds Number
S	Slip ratio
S_1, S_2, S_3	Principal stresses defined when introduced
S_{alt}	Alternate stress
S_{eq}	Equivalent alternating stress with zero mean stress
S_m	Mean stress
T	Temperature
$T_{wi,1}$	Inner wall temperature averaged over the fraction C_1 of the circumferential inner area.

$T_{wo,1}$	Outer wall temperature averaged over a fraction C_1 of the circumferential outer area.
$T_{wo,2}$	Outer wall temperature averaged over the top half of the area.
$T_{wo,3}$	Maximum circumferential outer wall temperature
u	Velocity
U	Combined heat transfer coefficient for the tube wall and the inner thermal film
v	Specific volume
W	Mass flow rate
X	Mass quality
Z	Axial location along tube from water inlet at the start of the incident heated region
ΔZ	Length of tube element

Greek Letters

α	Absorptivity
α_v	Void fraction
ΔP	Pressure difference
ΔT_i	Temperature oscillation range on inside wall
ΔT_w	Temperature difference across the tube wall
$\Delta(\Delta T_w)_{max}$	$\Delta T_{w,max} - \Delta T_{w,min}$ at a specified location
ϵ	Emissivity
ϵ_r	Roughness
Θ	Angle measured from the direction normal to the panel face
σ	Stefan-Boltzman constant
σ_{11}	Normal stress component in the plane of the tube cross section and perpendicular to the line of symmetry
σ_{22}	Normal stress component in the plane of the tube cross section and perpendicular to
σ_{33}	Normal stress component in the tube axial direction
σ_{12}	Shear stress
σ_y	Yield stress
τ	Time period
ϕ^2_{fo}	Two-phase frictional multiplier based on pressure gradient for total flow assumed liquid
$\phi^2_{fo,h}$	Value of ϕ^2_{fo} for the homogeneous model

Subscripts

a	Absorbed
ac	Acceleration
amb	Ambient
ave	Average
c	Refers to conditions at the CHF location
f	Liquid
fr	Friction
g	Gas
gr	Gravity
H	Water
i	Inlet
inc	Incident
j	Counter
l	Liquid
L	Loss
max	Maximum
min	Minimum
o	Outlet
tot	Total
wi	Inside of tube wall
wo	Outside of tube wall

REFERENCES

1. "Central Receiver Solar Thermal Power System, Phase 1, CDRL Item 2, Pilot Plant, Preliminary Design Report, Vol. IV, Receiver Subsystem," McDonnell-Douglas, MDC G6776, May 1977.

2. E. M. Sparrow and R. J. Krowech, "Circumferential Variations of Bore Heat Flux and Outside Surface Temperature for a Solar Collector Tube," Trans. ASME, J. Heat Transfer, 99, 360-366, August 1977.

3. N. A. Bailey and J. G. Collier, "The Estimation of Tube Wall Temperatures in the Evaporator Region of Sub-Critical Once-Through Sodium Heated Steam Generators," UK Atomic Energy Authority, AEEW-M 1000, August 1977.

4. S. Wolf and D. H. Holmes, "Critical Heat Flux in a Sodium-Heated Steam Generator Tube," Preprints of AICHE Papers, 17th National Heat Transfer Conference, August 1977, pp. 275-282.

5. J. A. Stevenson and J. C. Grafton, "Radiation Heat Transfer Analysis for Space Vehicles," Space and Information Systems Division, North American Aviation, Inc., SID 61-91, December 1961.

6. M. Abrams, "Convective Heat Loss from the McDonnell-Douglas Receiver," Sandia Laboratories, Memorandum, August 8, 1977.

7. "Forced Convection Heat Transfer to Circular Tubes - Part 1: Correlation for Fully Developed Turbulent Flow - Their Scope and Limitations," Engineering Sciences Data Unit Item 67016, Inst. Mech. Engrs., London 1967.

8. J. R. S. Thom, W. M. Walker, T. A. Fallon and G. F. S. Reising, "Boiling in Subcooled Water During Flow Up Heated Tubes or Annuli," Symposium on Boiling Heat Transfer in Steam Generator Units and Heat Exchangers, Inst. Mech. Engrs., Manchester, 1965.

9. S. Wolf, D. M. France and D. H. Holmes, "Recent Advances in Evaluating Critical Heat Flux Conditions in LMFBR Steam Generators," ASME Paper No. 77-WA/NE-11, 1977.

10. D. M. France, T. Chiang, R. D. Carlson and W. J. Minkowycz, "Measurement and Correlation of Critical Heat Flux in a Sodium Heated Steam Generator Tube," Argonne National Laboratory, ANL-CT-78-15, January 1978.

11. L. Biasi, G. C. Clerici, S. Garribba, R. Sala and A. Tozzi, "Studies on Burnout - Part 3 - A New Correlation for Round Ducts and Uniform Heating and Its Comparison with World Data," Energia Nucleare, 14, 9, 530-536, September 1967.

12. D. C. Groeneveld and G. G. J. Delorme, "Prediction of Thermal Non-Equilibrium in the Post-Dryout Regime," Nuclear Engineering and Design, 36, 17-26, 1976.

13. A. A. Bishop, P. O. Sandberg and L. S. Tong, "Forced Convection Heat Transfer at High Pressure After the Critical Heat Flux," ASME Paper No. 65-HT-31, 1965.

14. J. B. Heineman, "An Experimental Investigation of Heat Transfer to Superheated Steam in Round and Rectangular Channels," Argonne National Laboratory, ANL-6213, 1960.

15. "Incoloy Nickel-Iron-Chromium Alloys," Huntington Alloy Products Division, The International Nickel Company, Huntington, West Virginia, 1973.

16. J. G. Collier, Convective Boiling and Condensation, McGraw-Hill Book Co., 1972.

17. L. F. Moody, "An Approximate Formula for Pipe Friction Factors," Mechanical Engineering, Vol. 69, 1947.

18. E. L. Miropol'skii, M. E. Shitsman, R. I. Shneerova, "Influence of Heat Flux and Velocity on Hydraulic Resistance with Steam-Water Mixture Flowing in Tubes," Teploenergetika, Vol. 12, No. 5, 1965.

19. J. F. Marchaterre and B. M. Hogland, "Correlation for Two-Phase Flow," Nucleonics, 20, 8, 1962.

20. C. L. Chu, "TASA-01 User's Manual," General Electric Co., NEDE-23714, October 1977.

21. R. D. Tobin, "Solar Receiver Heat Flux Capability and Structural Integrity," Rocketdyne, R-9958, May 1976.

22. D. M. France, R. D. Carlson, T. Chiang, and R. Priemer, "CHF-Induced Thermal Oscillations Measured in an LMFBR Steam Generator Tube Wall," Argonne National Laboratory, ANL-CT-78-1, October 1977.

23. C. L. Chu, S. Wolf and A. W. Dalcher, "Oscillatory Dryout Related Thermal Stresses in Clean Steam Generator Tubes," ASME Paper No. 76-JPGC-NE-2, September 1976.

24. C. L. Chu, J. M. Roberts, and A. W. Dalcher, "DNB Oscillatory Temperature and Thermal Stress Responses for Evaporator Tubes Based on Rivulet Model," ASME Paper No. 77-WA/NE-5, 1977.

25. P. M. Magee, D. F. Casey, C. L. Chu, C. L. Dillman, J. M. Roberts and S. Wolf, "An Evaluation of Strain Cycling Effects in the DNB Zone of CRBR Evaporators," General Electric Co., NEDM-14164, December 1976.

26. J. F. Jones, Jr. and D. L. Siebers, "Analysis of the Thermal Fatigue Induced by DNB Oscillations in the MDAC Rocketdyne Pilot and Commercial Plant Solar Receiver Designs," Sandia Laboratories, SAND77-8283, December 1977.

27. "Case 1592, Class 1 Components in Elevated Temperature Service, Appendix T," ASME Boiler and Pressure Vessel Code, 1974 Code Cases, ASME, New York, 1974, pp 385-394.

28. "ASME Boiler and Pressure Vessel Code, Section III - Division I, Rules for Construction of Nuclear Power Plant Components," Subsection NA, General Requirements, ASME, New York, 1974.

29. R. T. Lahey, Jr. and G, Yadigaroglu, "NUFREQ, A Computer Program to Investigate Thermo-Hydrodynamic Stability," General Electric Co., NEDO-13344, July 1973.

30. R. T. Lahey, Jr. and G. Yadigaroglu, "A Lagrangian Analysis of Two-Phase Hydrodynamic and Nuclear-Coupled Density Wave Oscillations," Heat Transfer, Vol. IV, 1974, Proceedings of the 5th International Heat Transfer Conference, September 3-7, 1974, Tokyo, pp 225-229.

31. K. Chen, G. Yadigaroglu and S. Wolf, "Dynamic Stability of the CRBRP Prototype Steam Generator Test Loop and the CRBRP Evaporator Loop Under Low-Power, Low-Flow Rate Natural Circulation Conditions," General Electric Co., NEDM-14157, November 1976.

32. D. J. Rush and D. E. Naaf, "Literature Review and State-of-the-Art Report on Hydraulic Stability," General Electric Co., NEDM-13974, June 1973.

APPENDIX A

ADDITION OF A SUPERHEATER MODEL TO THE STABILITY ANALYSIS OF THE NUFREQ CODE*

A.1 INTRODUCTION

The NUFREQ code computes the pressure drop perturbations in a boiling channel caused by perturbations of the inlet velocity, inlet enthalpy, external heat flux or external pressure drop. From these calculations, the onset of instabilities due to density-wave oscillations can be predicted. The present work extends the calculations of the NUFREQ code to incorporate a superheat region extending beyond the boiling region. At constant pressure, the fluid in the superheat regime is assumed to have a linear specific volume - enthalpy relationship and an analysis similar to that of the boiling regime is presented for the superheat regime.

This Appendix presents only the additional formulation needed to treat the superheat region. The basic approach to the stability analysis can be found in Ref. 1.

---

* Work reported in this section was performed by Mr. K. C. Chan under the direction of Dr. G. Yadigaroglu of the University of California, Berkeley, under Consultant Agreement for the Fast Breeder Reactor Department, General Electric Co., P.O. No. 190-K8A14.

A.2 NOMENCLATURE

English Letters

A	Area, ft^2
D_H	Hydraulic diameter, ft
f	Friction factor
g	Acceleration of gravity, ft/s^2
g_c	Gravitational constant, $lb_m \cdot ft/lb_f \cdot s^2$
G	Mass flux, lb_m/ft^2
h	Enthalpy, Btu/lb_m
j	Velocity, ft/s
k_o	Slope of a specific volume - enthalpy line at constant pressure
K_{EXIT}	Exit loss coefficient
L	Length, ft
P	Pressure, psia
P_H	Heated perimeter, ft
q"	Volumetric heat generation, $Btu/ft^3 s$
s	Laplace transform variable, s^{-1}
t	Time, s
v	Specific volume, ft^3/lb_m
y	Axial location from start of superheat region, ft
z	Axial location from heated inlet, ft

Greek Letters

η	Superheat boundary, ft
λ	Boiling boundary, ft

μ Transit time in boiling region, s

ν Transit time in subcooled region, s

ξ Relative time defined when introduced

Ξ Superheat transfer functions

ρ Density, lb_m/ft^3

ρ_g Density of saturated vapor, lb_m/ft^3

ω Defined when introduced

Ω Defined when introduced

Subscripts

f Liquid

H Heated region

i Inlet

o Steady state

R Riser

s Superheat region

A.3 THEORETICAL ANALYSIS

In the superheat region, the specific volume-enthalpy line of the gas at constant pressure has approximately a linear behavior with a slope k_o, as shown in Figure A.1. Thus, superheated steam at approximately constant pressure can be treated as a perfect gas.

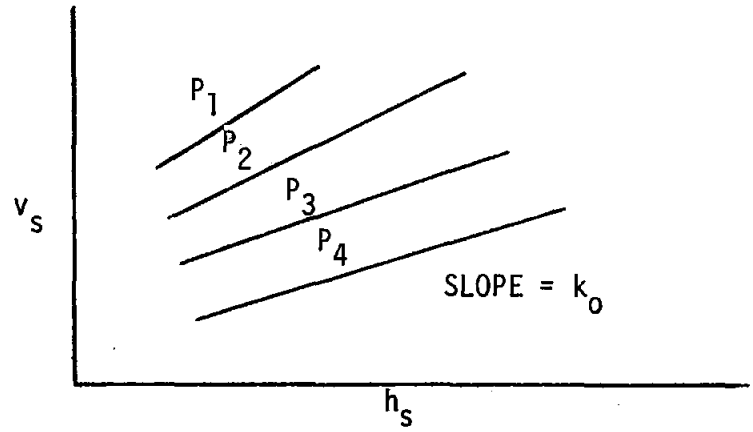

Figure A.1. v_s - h_s Lines for Steam at Constant Pressure

The equation of continuity for the superheat region can be written as:[1]

$$\frac{D\rho_s}{D\xi} + \rho_s \frac{\partial j_s}{\partial z} = 0 \qquad (1)$$

where $\xi = t-t'$, (2)

and t' is the time at which the fluid particle crosses the superheat boundary.

The superheat region energy equation can be written as:

$$\frac{Dh_s}{D\xi} = \frac{q'' P_H}{A\rho_s} \qquad (3)$$

From the relationship illustrated in Figure A.1:

$$\frac{dh_s}{d\rho_s} = \frac{dh_s}{dv_s}\frac{dv_s}{d\rho_s} = -\frac{1}{\rho_s^2 k_o} \qquad (4)$$

Substituting Eq. (4) into (3) and integrating, yields:

$$\rho_s = \rho_g e^{-\omega\xi} \tag{5}$$

where $$\omega = \frac{k_o q'' P_H}{A} \tag{6}$$

The superheat region momentum equation can be written as:

$$-\frac{dp}{dz} = \frac{\rho_s}{g_c}\frac{Dj_s}{Dt} + \frac{f\rho_s j_s^2}{2g_c D_H} + \frac{g}{g_c}\rho_s \tag{7}$$

This equation can be integrated for the heated region and the adiabatic riser. After linearization and Laplace transformation, one obtains:

$$\delta\Delta p_{s,H} = \int_{\eta}^{L_H} \{ \frac{\rho_s}{g_c}\delta(\frac{Dj_s}{Dt}) + \frac{fG_o}{g_c D_H}\delta j_s + [\frac{1}{g_c}(\frac{Dj}{Dt}) + \frac{fj_s^2}{2g_c D_H} + \frac{g}{g_c}]\delta\rho_s \} dz$$

$$- \{ \frac{f\rho_f j_s^2(\eta)}{2g_c D_H} + \frac{g}{g_c}\rho_f \} \delta\eta + K_{EXIT}\{ \frac{G_o}{g_c}\delta j_s + \frac{j_s^2(L_H)}{2g_c} + [\delta\rho(L_H)]\} \tag{8}$$

$$\delta\Delta p_R = \int_{L_H}^{L_R} [\frac{fj_s^2(L_H)}{2g_c D_H} + \frac{g}{g_c}]\delta\rho_R \, dz + \int_{L_H}^{L_R} \{ \frac{\rho_s(L_H)}{g_c}\delta(\frac{Dj_R}{Dt}) + \frac{f j_s(L_H)}{g_c D_{H_R}}\delta j_R \} dz \tag{9}$$

To carry out the integration, one has to find

$$\delta\left(\frac{Dj}{Dt}\right), \quad \delta j_s \quad \text{and} \quad \delta\rho;$$

Eqs. (1) and (5) give:

$$\frac{\partial j_s}{\partial z} = \omega \tag{10}$$

For the constant heat flux, Eq. (5) can be integrated to yield:

$$j_s = \omega(z-\eta) + \Omega(\eta-\lambda) + j_i \tag{11}$$

where $\Omega \equiv \dfrac{q_o'' P_H v_{fg}}{A\, h_{gf}}$

Here, Ω is defined as the characteristic reaction frequency[1] in the two-phase region, η is the location of the superheat boundary, and λ is the location of the boiling boundary. Eq. (11) can be perturbed and Laplace transformed to yield:

$$\delta j_s = -\omega\,\delta\eta + \Omega(\delta\eta-\delta\lambda) + \delta j_i \tag{12}$$

Similarly, for the riser:

$$\delta j_R = \left(\frac{A_H}{A_R}\right)\delta j_s \tag{13}$$

The acceleration term, $\delta\left(\frac{Dj}{Dt}\right)$ is found by taking the material derivative of Eq. (11). After linearization and Laplace transformation, one obtains:

$$\delta\left(\frac{Dj_s}{Dt}\right) = (1-e^{-s\mu_o})\,\Omega[-\Omega\,\delta\lambda + \delta j_i] + s\,\delta j_i + \omega\,\{-\omega\,\delta\eta$$

$$+ e^{-s(\mu_o + v_o)}\delta j_i + \Omega e^{-s(\mu_o + v_o)}[\delta\eta - \delta\lambda]\} \qquad (14)$$

For the riser, one obtains in a similar manner:

$$\delta\left(\frac{Dj_R}{Dt}\right) = \frac{A_H}{A_R}\,\{(\Omega - \omega)(1-e^{-s\mu_o})(-\Omega\delta\lambda + \delta j_i)$$

$$- \omega\,\delta j_i\,(1-e^{-sv_o}) + s\,\delta j_i\} \qquad (15)$$

The density perturbation is obtained by linearizing and laplace-transforming Eq. (5):

$$\delta\rho = -\rho_g \omega e^{-\omega\xi}\,\delta\xi \qquad (16)$$

The differential $\delta\xi$ can be eliminated by perturbing the identity

$$z \equiv y + \eta(t) \qquad (17)$$

For constant z, one obtains from Eq. (17):

$$dz = 0 = \delta y + \delta\eta \qquad (18)$$

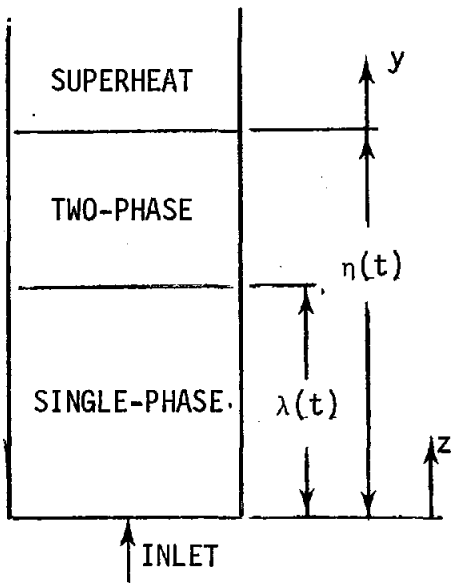

Figure A.2. Flow Regions

Integrating Eq. (11) yields:

$$y(t) = e^{\omega t}\int_{t'}^{t} e^{-\omega t'}\{j_i(t'-\mu-\nu) + \Omega[\eta(t'-\mu-\nu)-\lambda(t'-\mu-\nu)]\}dt' \qquad (19)$$

Eq. (19) can be perturbed by using the following relationship:

$$\delta y = \left(\frac{\partial y}{\partial j_i}\right) \delta j_i + \left(\frac{\partial y}{\partial \xi}\right) \delta \xi$$

Using Eqs. (20) and (18), $\delta\xi$ in Eq. (16) can be eliminated to yield:

$$\delta \rho_s = \frac{\rho_f \omega e^{-2(\omega\xi + \Omega\mu)}}{j_{i_o}} \left\{ \frac{e^{-s(\mu_o + \nu_o)}}{s-\omega} [1-e^{(\omega-s)\xi}] \delta j_i + \delta\eta \right\} \qquad (21)$$

The differential $\delta\eta$ is obtained by using the relationship:

$$\delta\eta = - \left.\frac{\delta \rho_{2\phi}}{\left(\frac{\partial \rho_{2\phi}}{\partial z}\right)_o}\right| \quad \text{at } z = \eta_o \qquad (22)$$

and from Ref. 1, one obtains

$$\delta\eta = \frac{e^{-s\nu_o}}{s-\Omega} [1-e^{(\Omega-s)\mu_o}] \delta j_i \qquad (23)$$

In the adiabatic riser,

$$\delta \rho_R = \delta \rho_s (L_H) \exp\left\{-s \frac{A_H (z-L_H)}{A\ j_s (L_H)}\right\} \qquad (24)$$

Eqs. (8) and (9) can now be integrated to yield:

$$\delta \Delta p_s = \delta \Delta p_{s,H} + \delta \Delta p_R$$

$$= \Xi_1 (s) \delta j_i + \Xi_2 (s) \delta q''' + \Xi_3 (s) \delta h_i \qquad (25)$$

Where the Ξ's are the appropriate superheat-region transfer functions

REFERENCES

1. R. T. Lahey, Jr. and G. Yadigaroglu, "NUFREQ, a Computer Program to Investigate Thermo-Hydraulic Stability," General Electric Co., NEDO-13344, (July 1973).

DISTRIBUTION

Large Power Systems Branch (4)
Division of Central Power Systems
U.S. Department of Energy
Washington, D.C. 20545
Attn: G. W. Braun, Asst. Director
J. Zingeser, Project Officer
J. Weisiger, Program Manager
G. M. Kaplan, Chief

Aerospace Corporation (2)
P.O. Box 92957
Los Angeles, CA 90009
Attn: R. Leatherman
K. Zondervan

Babcock & Wilcox (2)
1562 Beeson
Alliance, OH 44601
Attn: T. B. Brown
M. Wiener

Black & Veatch Consulting Engineers
P.O. Box 8405
Kansas City, MO 64114
Attn: J. E. Harder

Combustion Engineering, Inc. (3)
1000 Prospect Hill Road
Windsore, CT 06095
Attn: C. R. Bozzuto
M. J. Davidson
H. M. Payne

ETEC/STMPO (3)
9550 Flair Park Drive
Suite 210
El Monte, CA 91731
Attn: K. L. Adler
G. C. French
R. W. Wiese

Division of Solar Technology
U.S. Department of Energy
San Francisco Operations Office
1333 Broadway
Oakland, CA 94612
Attn: S. D. Elliott

Foster Wheeler Energy Corp. (2)
110 South Orange Avenue
Livingston, NJ 07039
Attn: S. F. Wu
R. J. Zoschak

Los Angeles Department of Water & Power (2)
P.O. Box 111
Los Angeles, CA 90051
Attn: J. M. Hayashi
C. Singman

Martin Marietta Aerospace (2)
P.O. Box 178
Denver, CO 80201
Attn: D. Gorman
T. R. Tracey

McDonnell Douglas (3)
5301 Bolsa Avenue
Huntington Beach, CA 92647
Attn: I. Catton
G. Coleman
R. Gervais

Rocketdyne Division (3)
Rockwell International Corp.
6633 Canoga Avenue
Canoga Park, CA 91304
Attn: J. M. Friefeld
A. Liebman
D. Vanevenhoven

Riley-Stoker
P.O. Box 547
Worcester, MA 01613
Attn: A. H. Rawdon

Southern California Edison (2)
P.O. Box 800
Rosemead, CA 91770
Attn: L. Rasband
W. H. von KleinSmid

Stearns-Roger (2)
P.O. Box 5888
Denver, CO 80217
Attn: A. W. McKenzie
H. C. Welz

W. B. Jones, 5835
T. B. Cook, Jr., 8000; Attn: W. J. Spencer, 8100
C. H. DeSelm, 8200
B. F. Murphey, 8300
J. F. Jones, 8122
M. Abrams, 8124
L. Gutierrez, 8400; Attn: R. A. Baroody, 8410
J. W. Pearce, 8420
G. W. Anderson, 8440
C. M. Tapp, 8460
C. S. Selvage, 8470
R. C. Wayne, 8450
W. G. Wilson, 8451
A. C. Skinrood, 8452
E. T. Cull, 8452 (20)
L. A. Hiles, 8452
J. W. Liebenberg, 8452
M. B. Loll, 8452
C. W. Moore, 8452
L. N. Tallerico, 8452
Publications & Public Information Division, 8265, for TIC (27)
F. J. Cupps, 8265/Technical Library Processes Division, 3141
Technical Library Processes Division, 3141 (2)
Library & Security Classification Division, 8266-2 (3)